

# Micro-Pattern Gas Detector Studies for the ND280m TPC Detector at the T2K Experiment

Master Thesis by Melody Ravonel  
Under the direction of Prof. Alain Blondel

July 2006 - July 2007



Département de Physique Nucléaire et Corpusculaire  
Université de Genève

### **Abstract**

This thesis reports on a study of MPGD based readout for the TPCs of the near detector of the T2K neutrino oscillation experiment at JPARC in Japan. Although the readout technology was chosen to be Micromegas this study also focuses on the GEM readout. Before mounting on the TPC, the Micromegas module will be mounted on a test bench at CERN for a full characterisation. Designs and electrostatic simulations of the calibration test bench are described for both readout schemes and the first results of the commissioning with the GEM readout are finally presented.

## Acknowledgments

There is a certain number of persons I would like to thank. First of all, Prof. Alain Blondel for giving me the opportunity to work in his group. Besides him, the other members of the group for welcoming me and helping me with their advices.

I would like particularly thanks Nicolas Abgrall, Marie Di Marco and Didier Ferrere, for their investing in the GEM test bench and also Florian Masciocchi and Pierre Bené for their work during the construction of the test bench.

I would like to thanks Thorsten Lux and Federico Sanchez for their help in the measurement, and the result analysis. I would like to thanks Thorsten, Nicolas, Federico and Raphaël for having carefully read my master thesis and for their numerous advices.

Finally, I would like to thanks my parents for their support in my studies.

## Contents

<b>1</b>	<b>Neutrino oscillations</b>	<b>1</b>
1.1	Neutrino oscillation ( $\hbar=c=1$ ) [1, 2]	1
1.1.1	Two flavour oscillations	1
1.1.2	Three-flavour oscillations	3
1.2	Neutrino oscillations in matter [2, 3]	3
1.2.1	Constant density	6
1.2.2	Non-constant density and MSW effect	7
<b>2</b>	<b>The T2K experiment</b>	<b>9</b>
2.1	Kinematics of the neutrino beam from pion decay: the off-axis technique	10
2.2	The neutrino beam line	12
2.2.1	The proton accelerator	13
2.2.2	The target station	13
2.2.3	The decay tunnel	14
2.2.4	The MUon MONitor (MUMON)	15
2.3	The ND280m Detector	15
2.3.1	The ND280	15
2.3.2	The N-GRID	17
2.4	The 2KM complex	18
2.5	The Super-Kamiokande detector	18
<b>3</b>	<b>Gas detectors and TPCs</b>	<b>20</b>
3.1	Physical processes in gaseous detectors	20
3.1.1	Ionization	20
3.1.2	Drift velocity	20
3.1.3	Diffusion	21
3.1.4	Gas Amplification	22
3.2	Principle of a Time Projection Chamber (TPC)	22
3.3	Multi-Wire Proportional Chamber	23
3.4	Micro-Pattern Gas Detectors (MPGDs)	24
3.4.1	The Gas Electron Multipliers (GEMs)	24
3.4.2	The MICRO-Mesh Gaseous Structure (MICROMEGAS)	25
3.4.3	Differences between the various readout schemes	26
3.5	The ND280 TPC resolution	27
<b>4</b>	<b>The test bench</b>	<b>28</b>
4.1	Test bench description	28
4.1.1	Module and calibration box for the GEM test bench	29
4.1.2	Module and calibration box for the Micromegas test bench	30
4.1.3	Data Acquisition (DAQ)	32
4.1.4	The iron source	33
4.1.5	X-rays attenuation	34
4.1.6	Effective coverage	38



<b>5</b>	<b>Electrostatic simulations for the test bench</b>	<b>39</b>
5.1	Maxwell/GARFIELD Implementation . . . . .	39
5.2	Distortion quantification . . . . .	39
5.2.1	Collection coefficient . . . . .	40
5.2.2	Mean shift of an electron . . . . .	41
5.3	Electrostatic simulations for the Micromegas test bench . . . . .	42
5.3.1	Influence of the external setup . . . . .	42
5.3.2	Border frame mesh (BFM) potential and pillars influence . . . . .	44
5.3.3	Determination of the nominal setting . . . . .	45
5.3.4	Alignment precision . . . . .	47
5.4	Electrostatic simulations for the GEM test bench . . . . .	48
5.4.1	Guard ring influence . . . . .	49
<b>6</b>	<b>GEM measurement results</b>	<b>54</b>
6.1	Scope . . . . .	54
6.2	Spectrum Reconstruction . . . . .	54
6.2.1	Spectrum Reconstruction algorithm . . . . .	54
6.2.2	Spectrum fit . . . . .	55
6.3	Stability . . . . .	56
6.3.1	Time Stability . . . . .	56
6.3.2	Pad plane uniformity . . . . .	57
6.4	Difference between the sectors . . . . .	59
6.4.1	Variation of the GEM potential . . . . .	60
6.4.2	Transfer and induction field variation . . . . .	62
6.4.3	Drift field variation . . . . .	63
6.5	Modification of the guard ring potential . . . . .	64
6.6	Pad response function: source displacement over three pads . . . . .	66
<b>7</b>	<b>Conclusion</b>	<b>69</b>
	<b>References</b>	<b>70</b>

## List of Figures

1	Feynman diagrams contributing to the potential which influences the neutrino propagation of neutrinos. For the neutral current, the same Feynman diagrams are also possible replacing $e^-$ by $n$ or $p$ ( $n \equiv$ neutron, and $p \equiv$ proton), and replacing $\nu_e$ by $\nu_\mu$ or $\nu_\tau$ as well as $\bar{\nu}_e$ by $\bar{\nu}_\mu$ or $\bar{\nu}_\tau$ . . . . .	4
2	View of the long baseline experiment [4] . . . . .	10
3	Pion decay (laboratory frame) . . . . .	10
4	Left: $E_{\nu_\mu}$ versus $p_\pi$ . Right: on-axis and off-axis energy spectrum [1]. . . . .	11
5	Probability to observe $\nu_\mu \rightarrow \nu_x$ : $P( \nu_\mu\rangle \rightarrow  \nu_x\rangle; L) = \sin^2(2\theta_{23}) \sin^2(1.27\Delta m_{23}^2 L/E)$ as a function of the distance $L$ in [m]. The parameters are set as: $E = 30 \text{ MeV}/\theta$ , with $\theta = 3^\circ, 2.5^\circ, 2^\circ$ , $\Delta m_{23}^2 = 2.4 \cdot 10^{-3} \text{ eV}^2$ and $\sin^2 \theta_{23} = 0.44$ . . . . .	12
6	The neutrino beam line . . . . .	12
7	Overview of the different stages of the proton acceleration in the JPARC complex [5]. . . . .	13
8	Overview of the different stations in JPARC (top) [5]. Target station (down) [5]. . . . .	14
9	Decay Tunnel [5]. . . . .	15

10	The ND280 off-axis detector overview [5](left).The ND280 tracking section design [4](right)	16
11	Feynman diagrams for neutral and charged current . . . . .	16
12	The N-GRID detectors setup at the near detector hall [5]. . . . .	18
13	Super-Kamiokande detector [1]. . . . .	19
14	GARFIELD simulation of the drift velocity (left), diffusion coefficients (middle) and transverse diffusion distribution of an electron in a uniform electric field of 200 V/cm, for a drift distance of 4 cm in Ar : CF <sub>4</sub> : iC <sub>4</sub> H <sub>10</sub> (93 : 3 : 2), at $B = 0$ T. . . . .	21
15	TPC scheme for a colliding experiment (left).PEP4/9-TPC energy-deposit measurement in multi-hadron events. The muons and pions are separated at low momentum [6] (right). . . . .	22
16	Mechanism of the gating grid in order to suppress the ion back flow [7] (left). Principle of a multi-wire proportional chamber and charge smearing over the readout pads [8, 9] (right). . . . .	24
17	Microscopic photo of the foil (up-left). Detail of electric field lines (solid) and equipotentials (dashed) in the region of GEM holes. Most of the positive ions produced in the hole drift back to the top side of the GEMs [8](up-right). 3-GEM principle (down left) [10]. Transverse diffusion is suppressed in high magnetic field, therefore the charge is collected by very small number of pad [9](down right) . . . . .	25
18	Micro-mesh (up left). GARFIELD simulation of the electron (solid) and positive ion (dashed) drift lines in a Micromegas avalanche region (up right) [6]. Micromegas principle (down left).Transverse diffusion is suppressed in high magnetic field (down right)	26
19	GEM test bench (left). MICROMEGAS test bench (middle). . . . .	28
20	Gas system as it will be implemented at the CERN room. . . . .	29
21	GEM tower mounted on the pad plane inside the Plexiglas box (left), top view of the module with guard ring and shield surrounding the active area (right). . . . .	29
22	Calibration box, with its GEM setup . . . . .	30
23	Micromegas module (left). Micromegas field cage (right) . . . . .	30
24	Schematic view of the beginning of the Micromegas module . . . . .	31
25	Schematic view of the bottom of the gas box with the additional strip (left). Real view of the box with its potential setting (right). . . . .	31
26	On the left side the protection and converter cards linked to the ALTRO card (left). USB to FEC (U2F) interface card (right). . . . .	32
27	Collimator and grid setup for the GEM test bench and for the Micromegas test bench.	33
28	Top view of the strong source Micromegas collimator (left). Weak source support (right)	34
29	Attenuation length in air (left) and in Argon (right) as a function of the photon energy ?? . . . . .	34
30	Schematic view of the collimator and the spot on the micro mesh (or 3 <sup>rd</sup> GEM). $\theta(0)$ denotes the maximum angle of a punctual source placed at $y = 0$ . . . . .	36
31	Spot radius distribution depending on the collimator. . . . .	37
32	Example of mesh computation in the z-x plane at the level of the guard ring long side (left) short side (right); the mesh is refined where boundaries are more complex [11]. .	39
33	Transverse and longitudinal diffusion coefficients as a function of the drift field for ArCO <sub>2</sub> (90:10) (left) and for ArCF <sub>4</sub> iC <sub>4</sub> H <sub>10</sub> (93:3:2) (right). . . . .	40
34	Schematic view of an electron illumination. The collection coefficient is defined as the ratio between the blue electrons reaching the pad and the orange electrons. . . . .	41

35	Mean shift value for 1000 electrons sent above the middle of each pad for different design: Micromegas test bench design (left), version with a grounded shield base in aluminum (middle). Histogram of the mean shift of an electron drifting along perfectly straight field lines (right). . . . .	42
36	Electric field distortions without strip over the walls: equipotentials (left), mean shift value along the pad plane (right) . . . . .	42
37	Equipotentials (left) and mean shift values along the pad plane (right) with a strip over the walls. . . . .	43
38	Shift of an electron with a strip (left) and without strip (right) near the aluminum base.	43
39	Histogram of 5000 electrons sent above the edge (left) and the middle (middle) of the 1 <sup>st</sup> pad with a BFM potential set at -460 V. Histogram of the edge of the first pad for a BFM potential set at 0 V (right). . . . .	44
40	Equipotential for the G10 design: BFM at -460 V (left) and 0 V (right). . . . .	44
41	Mean shift value as a function of the shield potential for $V_{strip} = -765$ V (left), as a function of the strip potential for $V_{strip} = -361$ (middle) and as a function of the shield potential for $V_{strip} = -771$ (right) for the first and last pad. The mean shift values are obtained with a statistic of 1000 electrons sent above the middle of each pad. . . . .	45
42	Mean shift (top left) and sigma value of the gaussian electron shift distribution (top right) and collection coefficient (bottom left) as a function of the pad position. Potential configuration of the field cage (bottom right). The mean shift and sigma are obtained with a statistic of 1000 electrons, while the collection coefficient values are determined from 10 illuminations of 100 electrons sent uniformly above the pad. . . . .	46
43	Different simulated G10 design showing various possible misalignment. . . . .	47
44	Collection coefficient for the first pad (left) and mean shift value of an electron sent above the middle of the first pad as a function of the $dy$ parameter. . . . .	48
45	Equipotentials of the GEM box for the nominal setting. . . . .	49
46	Drift lines near the guard ring short side( left) and long side ( right) for a guard ring potential, $V_{NS} = -3557$ V - $DV=0$ V -(top) and $V_{GR} = -3677$ V - $DV=120$ V -(bottom). . . . .	50
47	Collection coefficient as a function of the pad position for $DV=-60$ V (top left), $DV=0$ V (top right), $DV=60$ V (bottom left) and $DV=120$ V (bottom right). . . . .	51
48	Mean shift value as a function of the pad position for $DV=-60$ V (top left), $DV=0$ V (top right), $DV=60$ V (bottom left) and $DV=120$ V (bottom right). . . . .	52
49	RMS of the electron shift distribution as a function of the pad position for $DV=-60$ V (top left), $DV=0$ V (top right), $DV=60$ V (bottom left) and $DV=120$ V (bottom right).	53
50	Spectrum of the iron source with a gaussian fit for the peak at 5.9 keV. The escape peak is also visible. The mean value of the gaussian fit is $1322 \pm 2$ and the sigma $217 \pm 2$ for a $\chi^2/ndf$ of 985.5/227. . . . .	55
51	Distribution of the mean value over one day (left). Mean value of the iron source peak as a function of time (1 bin = 16 min). . . . .	56
52	Distribution of the resolution over one day (left). Resolution of the iron source peak as a function of time (1 bin = 16 min). . . . .	57
53	Mean value per pad for 10 successive rows (left). The pads without value in the center are faulty pads. Mean distribution for the good pads (right). . . . .	58
54	Resolution value per pad for 10 rows (left). The pads without value in the center are faulty pads. Resolution distribution for the good pads (right). . . . .	58

55	Charge distribution per column normalized with the total charge collected over 10 rows (bottom right).	59
56	Spectrum obtained for a pad in the center of the first sector (left) and second sector(right).	60
57	Spectrum obtained over the pad (12,17) for $V_q= 310$ V (left), 315 V (middle) and 320 V (right).	61
58	Mean value (left) and resolution (right) as a function of $V_q$ .	61
59	Reconstructed spectrum for the first setting ( $dV=-800$ V). The mean value is $1330 \pm 13$ and the sigma $229 \pm 15$ for a $\chi^2/ndf = 29.49/14$ .	62
60	Mean and sigma value of the iron source peak (left) and resolution as a function of $dV$ (right).	63
61	Mean value of the iron source peak (left) and ratio value as a function of the drift field $DF$ (right). The resolution uncertainties are dominated by the sigma uncertainties.	64
62	Charge map for three GR voltage settings. The cluster of charges situated on the left side are due to the weak source.	65
63	Charge collected of the main hit pads normalized with the total charge inside the cluster (e.g $ROW > 10$ ), for a constant number of trigger (left) as a function of $DV$ , the potential difference to the nominal setting which is described in Table 10 ( $DV = V_{NS} - V_i$ , with i the setting number). Total normalized charge collected on the main hit pads (right) as a function of $DV$ .	65
64	Schematic position of the collimator without grid (left), with the grid at the edge of the spot (middle), inside the spot (right).	66
65	Arrival electron distribution without grid (top-left), with the grid at the edge of the spot (top-right), inside the spot (bottom). The top distribution are fitted with the same function which is used to determine the response function. For both grid distributions, the grid thickness of 6 mm was not taken into account and only the grid width was considered. In consequence the effect of the grid might be even more larger in the reality.	67
66	Schematic principle of the charge response function of a pad as a function of the collimator position (left). Collected charge as a function of the collimator position (right).	68

## 1 Neutrino oscillations

The observation of the electronic neutrino disappearance propagating from the sun and the  $\nu_\mu$  disappearance in atmospheric neutrinos prove that neutrino have mass and therefore the conventional description of the Standard Model is not complete. If neutrinos have a mass, then oscillations are possible between the different flavors.

### 1.1 Neutrino oscillation ( $\hbar=c=1$ ) [1, 2]

If neutrinos have non-zero masses, their flavor eigenstates do not necessarily coincide with their mass eigenstates. The flavor eigenstates  $|\nu_f\rangle$  ( $f = e, \mu, \tau$ ) are then described by a linear superposition of the mass eigenstates:

$$|\nu_f\rangle = \sum_j V_{fj} |\nu_j\rangle \quad , \quad \text{with } j = 1, 2, 3.$$

Assuming now that the state  $|\nu_f\rangle$  is a plane wave solution of the Schrödinger equation:

$$i \frac{d}{dt} |\nu_f(t)\rangle = \hat{H}^f |\nu_f(t)\rangle \quad \Rightarrow \quad |\nu_f(t)\rangle = e^{-i\hat{H}^f t} |\nu_f(0)\rangle$$

The amplitude of probability that a state  $|\nu_\alpha\rangle$  ( $f = \alpha$ ) at  $t = 0$  goes into the state  $|\nu_\beta\rangle$  ( $f = \beta$ ) at time  $t$  is given by:

$$\begin{aligned} A_{\alpha\beta} &= \langle \nu_\beta(t) | \nu_\alpha(0) \rangle \\ &= \langle \nu_\beta(0) | e^{-i\hat{H}^f t} | \nu_\alpha(0) \rangle \end{aligned}$$

Using that the Hamiltonian operator  $\hat{H}_{free}^n \equiv V^{-1} \hat{H}^f V$  is diagonal for the mass eigenstates and that the eigenstates are orthogonal:

$$\begin{aligned} A_{\alpha\beta} &= \langle \nu_\beta(0) | \sum_\gamma (V e^{-\hat{H}_{free}^n t} V^{-1})_{\alpha\gamma} | \nu_\gamma(0) \rangle \\ &= \langle \nu_\beta(0) | \sum_{j,\gamma} V_{\alpha j} V_{j\gamma}^{-1} e^{-iE_j t} | \nu_\gamma(0) \rangle \\ &= \sum_j V_{\alpha j} V_{j\beta}^{-1} e^{-iE_j t} \end{aligned} \tag{1}$$

#### 1.1.1 Two flavour oscillations

In the two flavour case, the transformation matrix,  $V$ , is a simple rotation:

$$V(\theta_0) = \begin{pmatrix} \cos \theta_0 & \sin \theta_0 \\ -\sin \theta_0 & \cos \theta_0 \end{pmatrix}$$

where  $\theta_0$  is called the mixing angle.

The probability for a neutrino emitted in a state  $|\nu_\alpha\rangle$  at  $t=0$  to be observed in a state  $|\nu_\beta\rangle$  at time  $t$  is then:

$$\begin{aligned}
 P(|\nu_\alpha\rangle \rightarrow |\nu_\beta\rangle; t) &= |A_{\alpha\beta}|^2 \\
 &= |\cos\theta_0 \sin\theta_0 (-e^{-iE_1t} + e^{-iE_2t})|^2 \\
 &= 4\cos^2\theta_0 \sin^2\theta_0 \sin^2\left(\frac{(E_2 - E_1)t}{2}\right) \\
 &= \sin^2(2\theta_0) \sin^2\left(\frac{(E_2 - E_1)t}{2}\right)
 \end{aligned} \tag{2}$$

For relativistic neutrinos with momentum  $p$ :

$$\begin{aligned}
 E_j &= \sqrt{p^2 + m_j^2} = p \sqrt{1 + \left(\frac{m_j}{p}\right)^2} \\
 &\approx p \left(1 + \frac{m_j^2}{2p^2}\right) = p + \frac{m_j^2}{2p} \approx p + \frac{m_j^2}{2E}
 \end{aligned} \tag{3}$$

Using 3 in 2:

$$P(|\nu_\alpha\rangle \rightarrow |\nu_\beta\rangle; t) = \sin^2(2\theta_0) \sin^2\left(\frac{\Delta m_{21}t}{4E}\right) \tag{4}$$

where  $\Delta m_{21} = m_2^2 - m_1^2$ .

Defining the Hamiltonian as  $\hat{H}_{free}^n = \frac{1}{2E} \begin{pmatrix} 0 & 0 \\ 0 & \Delta m_{21} \end{pmatrix}$  we obtain directly the same approximate result.

The probability can be written in terms of the distance,  $L$ , travelled by the neutrinos (in the units  $\hbar = c = 1$ , we have for relativistic neutrinos  $L = t$ ) and  $L_{osc} = \frac{4\pi E}{\Delta m_{21}}$ , equation 4 can be written as:

$$P(|\nu_\alpha\rangle \rightarrow |\nu_\beta\rangle; L) = \sin^2(2\theta_0) \sin^2\left(\frac{\pi L}{L_{osc}}\right)$$

For  $L$  given in [m] or [km],  $E$  in [MeV] or [GeV] and  $\Delta m$  in [eV<sup>2</sup>]:

$$P(|\nu_\alpha\rangle \rightarrow |\nu_\beta\rangle; L) = \sin^2(2\theta_0) \sin^2\left(1.27 \frac{\Delta m_{21} L}{E}\right).$$

In term of  $\hbar c$ , we have:

$$P(|\nu_\alpha\rangle \rightarrow |\nu_\beta\rangle; L) = \sin^2(2\theta_0) \sin^2\left(\frac{\Delta m_{21} L}{4E\hbar c}\right).$$

Oscillations are cancelled for  $\theta_0 = 0$ , or when the neutrinos have the same masses. The mechanism described in this section is called *vacuum oscillation*.

### 1.1.2 Three-flavour oscillations

For the tree flavour oscillations, the flavours eigenstates are obtained through the mixing matrix  $V$  which can be factorized as:

$$V = UA,$$

with

$$A = \begin{pmatrix} e^{i\alpha} & 0 & 0 \\ 0 & e^{i\beta} & 0 \\ 0 & 0 & 1 \end{pmatrix},$$

the Majorana phase matrix which does not enter into oscillation phenomena<sup>1</sup>, and the neutrino mixing matrix<sup>2</sup> given by the Particle Data Group (PDG, [6]):

$$U = \begin{pmatrix} U_{e1} & U_{e2} & U_{e3} \\ U_{\mu1} & U_{\mu2} & U_{\mu3} \\ U_{\tau1} & U_{\tau2} & U_{\tau3} \end{pmatrix} = \begin{pmatrix} c_{12}c_{13} & s_{12}c_{13} & c_{13}e^{i\delta} \\ -s_{12}c_{23} - c_{12}s_{13}s_{23}e^{i\delta} & c_{12}c_{23} - s_{12}s_{13}s_{23}e^{i\delta} & c_{13}s_{23} \\ s_{12}s_{23} - c_{12}s_{13}c_{23}e^{i\delta} & c_{12}s_{23} - s_{12}s_{13}c_{23}e^{i\delta} & c_{13}c_{23} \end{pmatrix}, \quad (5)$$

where  $s_{ij} = \sin \theta_{ij}$  and  $c_{ij} = \cos \theta_{ij}$ . A  $3 \times 3$  unitary matrix such as the mixing matrix,  $U$ , can be parametrized with 3 angles and one complex phase  $\delta$  [1] and can be then understood for leptons as the analog of the CKM matrix used in the quark sector.

If the phase is non-zero, then it causes the breaking of the CP symmetry, whereas  $\theta_{13} = 0$ , the phase has no effect.

By now the the best limit for  $\theta_{13}$  is provided from the nuclear reactor experiment, Chooz:

$$\sin^2 2\theta_{13} < 0.1,$$

which value is in agreement with the good result obtained by using two flavours oscillation approximation in solar and atmospheric experiment.

A more precise measurement of this angle is one of the main purpose of the T2K experiment.

## 1.2 Neutrino oscillations in matter [2, 3]

The flavour conversion in an inhomogeneous matter potential occurring by an adiabatic transition is called MSW (Mikheyev-Smirnow-Wolfenstein) effect. The possible interactions of the neutrinos with matter are described in figure 1.

The effective low-energy Hamiltonian describing the relevant neutrino interactions is given by:

$$H_{int} = \frac{G_F}{\sqrt{2}} \left( J^{+,\mu}(x) J_{\mu}^{-}(x) + \frac{1}{4} J^{N,\mu}(x) J_{\mu}^N(x) \right) \quad (6)$$

where  $J_{\mu}^{+/-}$  and  $J_{\mu}^N$  are respectively the standard fermionic charged currents and the neutral current. Neutral and charged currents can be expressed with the lepton spinor,  $l(x)$ , and the corresponding neutrino  $\nu_l(x)$ :

<sup>1</sup>The phase factors  $\alpha$  and  $\beta$  are non-zero only if neutrinos are Majorana particles (whether or not they are is unknown)

<sup>2</sup>also called Pontecorvo-Maki-Nakagawa-Sakata (PMNS or MNS) matrix

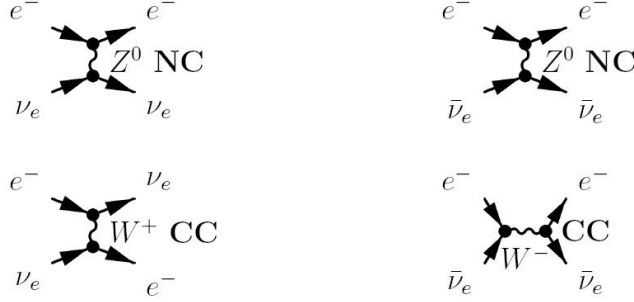


Figure 1: Feynman diagrams contributing to the potential which influences the neutrino propagation of neutrinos. For the neutral current, the same Feynman diagrams are also possible replacing  $e^-$  by  $n$  or  $p$  ( $n \equiv$ neutron, and  $p \equiv$ proton), and replacing  $\nu_e$  by  $\nu_\mu$  or  $\nu_\tau$  as well as  $\bar{\nu}_e$  by  $\bar{\nu}_\mu$  or  $\bar{\nu}_\tau$ .

$$\begin{aligned}
J_\mu^+(x) &= \bar{\nu}_e(x) \gamma_\mu (1 - \gamma_5) e(x) \\
J_\mu^-(x) &= \bar{e}(x) \gamma_\mu (1 - \gamma_5) \nu_e(x) \\
J_\mu^N(x) &= \sum_{l=e, \mu, \tau} \bar{\nu}_l(x) \gamma_\mu (1 - \gamma_5) \nu_l(x) - \bar{l}(x) (\gamma_\mu (1 - \gamma_5) - 4 \sin^2 \theta_W \gamma_\mu) l(x) \\
&\quad + \bar{p}(x) (\gamma_\mu (1 - g_A^{(p)} \gamma_5) - 4 \sin^2 \theta_W \gamma_\mu) p(x) - \bar{n}(x) (\gamma_\mu (1 - g_A^{(n)} \gamma_5)) n(x)
\end{aligned}$$

where  $g_A^{(n,p)}$  are the axial couplings for neutrons and protons, and  $\theta_W$ , the Weinberg angle, whose experimental value is  $\sin^2 \theta_W = 0.23120(15)$  [3].

Since the part of the Hamiltonian concerning the neutral current is identical for all flavours, we can simplify by studying only the charged current part. Writing  $s$  and  $p_e$  as the spin and the momentum of the electron, we have:

$$\begin{aligned}
\langle e(s, p_e) | H_{CC} | e(s, p_e) \rangle &= \frac{G_F}{\sqrt{2}} \langle e(s, p_e) | \bar{e}(x) \gamma_\mu (1 - \gamma_5) \nu_e(x) \bar{\nu}_e(x) \gamma^\mu (1 - \gamma_5) e(x) | e(s, p_e) \rangle \\
&= \frac{G_F}{\sqrt{2}} \bar{\nu}_e(x) \gamma_\mu (1 - \gamma_5) \nu_e(x) \langle e(s, p_e) | \bar{e}(x) \gamma^\mu (1 - \gamma_5) e(x) | e(s, p_e) \rangle
\end{aligned}$$

where the Fierz identity has been used to separate the neutrino's and electron's spinor. Expanding the electron fields  $e(x)$  in plane waves we find:

$$\begin{aligned}
&\langle e(s, p_e) | \bar{e}(x) \gamma^\mu (1 - \gamma_5) e(x) | e(s, p_e) \rangle \\
&= \frac{1}{V} \langle e(s, p_e) | \bar{u}_s(p_e) a_s^\dagger(p_e) \gamma^\mu (1 - \gamma_5) a_s(p_e) u_s(p_e) | e(s, p_e) \rangle
\end{aligned}$$

where  $a_s^\dagger$  and  $a_s$  are the creation and destruction operator for the electron,  $u_s(p_e)$  and  $\bar{u}_s(p_e)$  their wave function, and finally  $V$  a normalisation factor. The trajectory of the neutrino is determined by the electrons present in the matter. To obtain the effective Hamiltonian due to the electrons in the medium,  $H_{CC}^{(e)}$ , we have to average over all the momentum and spin of the electrons, and sum



over each electron in the medium. We assume the energy distribution of the electrons in the matter,  $f_e(E_e)$ , homogeneous and normalized to 1 ( $\int d^3p_e f(E_e) = 1$ ). We obtain:

$$H_{CC}^{(e)} = \frac{G_F}{\sqrt{2}} \bar{\nu}_e(x) \gamma_\mu (1 - \gamma_5) \nu_e(x) \times \int d^3p_e f(E_e) \frac{1}{2} \sum_s \sum_{j=1}^{n_e} \left[ \frac{1}{V} \langle e(s, p_e) | \bar{u}_s(p_e) a_s^\dagger(p_e) \gamma^\mu (1 - \gamma_5) a_s(p_e) u_s(p_e) | e(s, p_e) \rangle \right]$$

where we assume that the medium has a same number of electrons with spin 1/2 and -1/2. In addition we have:

$$\frac{1}{V} \sum_{j=1}^{n_e} \langle e(s, p_e) | a_s^\dagger(p_e) a_s(p_e) | e(s, p_e) \rangle = n_e(p_e)$$

We have also:

$$\frac{1}{2} \sum_s \langle e(s, p_e) | \bar{u}_s(p_e) \gamma^\mu (1 - \gamma_5) u_s(p_e) | e(s, p_e) \rangle = \frac{1}{2} \text{Tr} \left[ \frac{m_e + \not{p}_e}{2E_e} \gamma^\mu (1 - \gamma_5) \right] = \frac{p_e^\mu}{E_e}$$

Thus:

$$H_{CC}^{(e)} = \frac{G_F}{\sqrt{2}} \bar{\nu}_e(x) \gamma_\mu (1 - \gamma_5) \nu_e(x) \int d^3p_e f(E_e) n_e(p_e) \frac{p_e^\mu}{E_e}$$

We assume also that the distribution of energy in the medium is isotropic. That implies:

$$\int d^3p_e f(E_e) p_e^j = 0 \quad \text{with } j = 1, 2, 3.$$

In consequence, the only term contributing after the integration over  $d^3p_e$  is  $p_e^0 \equiv E_e$ . The integration gives then:

$$H_{CC}^{(e)} = \frac{G_F n_e}{\sqrt{2}} \bar{\nu}_e(x) \gamma_0 (1 - \gamma_5) \nu_e(x)$$

where  $\int d^3p_e f(E_e) n_e(p_e) = n_e$ . The effective potential for  $\nu_e$  induced by its charged current interactions with the electron present in the matter is then given by:

$$V_{CC} = \langle \nu_e | \int d^3x H_{CC}^{(e)} | \nu_e \rangle = \frac{G_F n_e}{\sqrt{2}} \langle \nu_e | \int d^3x \bar{\nu}_e(x) \gamma_0 (1 - \gamma_5) \nu_e(x) | \nu_e \rangle$$

Neglecting the neutrino masses, we have  $(1 - \gamma_5) \nu_e(x) = 2\nu_e(x)$ , and since  $\langle \nu_e | a^\dagger u^\dagger(x) C u(x) | \nu_e \rangle = u^\dagger(x) u(x)$  when expanding the neutrino field as a plane-wave, we obtain:

$$V_{CC} = G_F n_e \frac{\sqrt{2}}{V} \int d^3x u^\dagger(x) u(x) = G_F n_e \sqrt{2}$$

In the case of the anti-neutrino, by taking the normal ordering which allows the anti-commutation between  $b$  and  $b^\dagger$  (i.e  $bb^\dagger = -b^\dagger b$ ), we find:

$$\langle \bar{\nu}_e | b v^\dagger(x) b^\dagger v(x) | \bar{\nu}_e \rangle = -v^\dagger(x) v(x)$$

where  $b$  and  $b^\dagger$  are the destruction and creation operator of an antiparticle which is here the anti-neutrino.

$$\begin{aligned} V_{CC} &= \frac{G_F n_e}{\sqrt{2}} \langle \bar{\nu}_e | \int d^3x \bar{\nu}_e(x) \gamma_0 (1 - \gamma_5) \nu_e(x) | \bar{\nu}_e \rangle = \frac{G_F n_e \sqrt{2}}{V} \langle \bar{\nu}_e | \int d^3x b v^\dagger(x) b^\dagger v(x) | \bar{\nu}_e \rangle \\ &= -G_F n_e \sqrt{2} \end{aligned}$$

The explicit development is made in [2]

### 1.2.1 Constant density

If  $n_n$  and  $n_e$  are the neutron and electron densities in the matter crossed by the neutrino, we find that the Hamiltonian density for the neutral current is proportional to  $V_{NC} = -\frac{\sqrt{2}}{2} G_F n_n$  for each flavour. For the electronic neutrino, as we saw in the previous section, there is an additional term that accounts for the CC interaction. The Hamiltonian, in the flavour basis, has then the following form:

$$\hat{H}_{int}^f = \begin{pmatrix} V_{CC} + V_{NC} & 0 & 0 \\ 0 & V_{NC} & 0 \\ 0 & 0 & V_{NC} \end{pmatrix}$$

The effect of the addition of  $V_{NC}$  is only to change an unmeasurable phase to all neutrino states. We assume then that the Hamiltonian can be written as:

$$\hat{H}_{int}^f = \begin{pmatrix} V_{CC} & 0 & 0 \\ 0 & 0 & 0 \\ 0 & 0 & 0 \end{pmatrix}$$

The total Hamiltonian is thus the sum between the Hamiltonian for a free particle and the Hamiltonian for a particle interacting with matter. Both are defined in different basis, but using the PMNS matrix (see (5)), we have:

$$\hat{H}_{tot}^f = V \hat{H}_{free}^n V^\dagger + \hat{H}_{int}^f$$

$\hat{H}_{tot}^f$  can be diagonalized in a new basis  $|\nu_i^m\rangle$ . The diagonal form of the Hamiltonian is then defined as:

$$\hat{H}_{tot}^m = \begin{pmatrix} \epsilon_1 & 0 & 0 \\ 0 & \epsilon_2 & 0 \\ 0 & 0 & \epsilon_3 \end{pmatrix}$$

where  $\epsilon_i$  ( $i = 1, 2, 3$ ) are the eigen values of the Hamiltonian.

For two flavours, the matrix transformation from the mass eigenstates into the flavours eigenstates can be written as a function of a new mixing angle, usually referred to, as the matter mixing angle  $\theta_m$ , i.e  $V(\theta_m) = \begin{pmatrix} \cos \theta_m & \sin \theta_m \\ -\sin \theta_m & \cos \theta_m \end{pmatrix}$ .

$$\begin{aligned} \hat{H}_{tot}^f &= V(\theta_m) \hat{H}_{tot}^m V^\dagger(\theta_m) = V(\theta_0) \hat{H}_{free}^n V^\dagger(\theta_0) + \hat{H}_{int}^f \\ &= \frac{1}{2E} V(\theta_0) \begin{pmatrix} 0 & 0 \\ 0 & \Delta m_{21} \end{pmatrix} V^\dagger(\theta_0) + \begin{pmatrix} V_{CC} & 0 \\ 0 & 0 \end{pmatrix} \\ &= \frac{1}{4E} \begin{pmatrix} -\Delta m_{21} \cos 2\theta_0 + 4EV_{CC} & \Delta m_{21} \sin 2\theta_0 \\ \Delta m_{21} \sin 2\theta_0 & \Delta m_{21} \cos 2\theta_0 \end{pmatrix} \end{aligned} \quad ^3$$

We find that:

$$\begin{aligned}\epsilon_1 &= \frac{1}{4E}(\Delta m_{21} + 2EV_{CC} - \Delta M_{21}) & \epsilon_2 &= \frac{1}{4E}(\Delta m_{21} + 2EV_{CC} + \Delta M_{21}) \\ \sin 2\theta_m &= \frac{\Delta m_{21} \sin 2\theta_0}{\Delta M_{21}} & \tan 2\theta_m &= \frac{\Delta m_{21} \sin 2\theta_0}{\Delta m_{21} \cos 2\theta_0 - 2EV_{CC}},\end{aligned}\quad (7)$$

where  $\Delta M_{21}$  is defined as the difference of the eigen values in analogy with the vacuum case:

$$\begin{aligned}\frac{\Delta M_{21}}{2E} &\equiv \epsilon_2 - \epsilon_1 \\ &= \sqrt{\Delta m_{21}^2 + 4EV_{CC}(EV_{CC} - \Delta m_{21}^2 \cos 2\theta_0)}\end{aligned}$$

One notes that the mixing angle and mass difference depend on the density of the medium. The value  $2EV_{CC} = \Delta m_{21} \cos 2\theta_0$  is called the MSW resonance. We choose  $\cos 2\theta_0 > 0$  so that  $\cos^2 \theta_0 > \sin^2 \theta_0$  (i.e  $\theta_0 < \pi/4$ ). With this choice,  $|\nu_1\rangle$  is defined as the neutrino mass eigenstate with the highest electronic content; so that  $m_2^2 > m_1^2$  and we have  $\Delta m_{21} > 0$ .

In the case of neutrinos interacting with matter, the resonant condition is:

$$2\sqrt{2}EG_F n_e = \Delta m_{21} \cos 2\theta_0$$

which is possible if  $\Delta m_{21} > 0$  (i.e  $m_2^2 > m_1^2$ ). On the contrary for the anti-neutrino:

$$-2\sqrt{2}EG_F n_e = \Delta m_{21} \cos 2\theta_0$$

which is only allowed if  $\Delta m_{21} \cos 2\theta_0 < 0$ .

### 1.2.2 Non-constant density and MSW effect

We suppose now that the density is not constant, the evolution of the flavour eigenstates of a neutrino is then given by :

$$i \frac{d}{dt} \nu_f = \hat{H}_{tot}^f \nu_f.$$

where  $\nu_f = \begin{pmatrix} |\nu_e\rangle \\ |\nu_\mu\rangle \\ |\nu_\tau\rangle \end{pmatrix}.$

Defining  $V(\theta_m(t)) \equiv V_t$ , the flavour eigenstates can be expressed in terms of the mass eigenstates as:

$$\nu_f = V_t \nu_m$$

Thus:

$$\begin{aligned}i \frac{d}{dt} (V_t \nu_m) &= \hat{H}_{tot}^f V_t \nu_m \\ i \left( \frac{d}{dt} V_t \nu_m + V_t \frac{d}{dt} \nu_m \right) &= \hat{H}_{tot}^f V_t \nu_m \\ i V_t \frac{d}{dt} \nu_m &= \left( \hat{H}_{tot}^f V_t - i \frac{d}{dt} V_t \right) \nu_m \\ i \frac{d}{dt} \nu_m &= \left( V_t^\dagger \hat{H}_{tot}^f V_t - i V_t^\dagger \frac{d}{dt} V_t \right) \nu_m \\ i \frac{d}{dt} \nu_m &= \left( \hat{H}_{tot}^m - i V_t^\dagger \frac{d}{dt} V_t \right) \nu_m\end{aligned}\quad (8)$$

---

<sup>3</sup>Normally an additional term should be included in the diagonal. However, as it is the same value for each element of the diagonal, this term doesn't have any effect on the oscillation.

For two flavours, equation (8) becomes:

$$\begin{aligned} i \frac{d}{dt} \nu_m &= \begin{pmatrix} 0 & -i \frac{d\theta_m}{dt} \\ i \frac{d\theta_m}{dt} & \frac{\Delta M_{21}^2}{2E} \end{pmatrix} \nu_m \\ &= \begin{pmatrix} 0 & -i \frac{E \Delta m_{21} \sin 2\theta_0}{\Delta^2 M_{21}^2} \frac{dV_{CC}}{dt} \\ i \frac{E \Delta m_{21} \sin 2\theta_0}{\Delta^2 M_{21}^2} \frac{dV_{CC}}{dt} & \frac{\Delta M_{21}^2}{2E} \end{pmatrix} \nu_m, \end{aligned}$$

where equation (7) has been used to calculate the derivative.

We see here that when the density variation is very slow (adiabatic case -  $\frac{dV}{dt} \ll 1$ ), a neutrino eigenstate of  $\hat{H}_{tot}^m$  at time  $t$  remains an eigenstate over time. When  $n_e = 0$  (e.g.  $V_{CC} = 0$ ), as in vacuum, the propagation eigenstate is always  $|\nu_2\rangle$  in our convention and there is no oscillation. This situation can be applied to the case of a  $\nu_e$  production in the sun. At the beginning,  $|\nu_e\rangle$  is close to be an eigenstate of propagation and remains in this state, if we consider that the density of the sun varies slowly, as in the adiabatic approximation. When the neutrino reaches the vacuum where  $n_e = 0$ , its eigenstate becomes  $|\nu_2\rangle$  and stays as such until the detector. The probability to observe an electronic neutrino from the sun on earth is then  $|\langle \nu_e | \nu_2 \rangle|^2 = \sin^2 \theta_0$  which is about  $\sin^2 \theta_0 \approx 1/3$  which is effectively equal to the fraction of  $\nu_e$ 's observed on earth with respect to the prediction of the solar model.

## 2 The T2K experiment

The T2K experiment is a long baseline neutrino oscillation experiment. It is designed to complete the knowledge of the MNSP matrix by measuring with a good precision  $\theta_{13}$ , the sign of  $\Delta m_{23}$  and the value of the CP-violating phase  $\delta$ .

By now, the experiments SNO, KamLAND, Super-Kamiokande, K2K and MINOS have provided indeed the others MNSP parameters:

- **SNO and KamLAND:** Both experiments have measured the parameters of solar oscillations:  $\theta_{12}$ ,  $\Delta m_{21}$ . Whereas SNO observed directly the solar neutrinos through both neutral and charged current interactions, KamLAND observed anti-neutrino interactions produced by nuclear reactors in Japan at a distance  $L/E$  of the same order of magnitude as the oscillation frequency of solar neutrinos.

The best fit gives [12]:

$$\begin{aligned}\sin^2 \theta_{12} &= 0.30_{-0.03}^{0.02} \\ \Delta m_{21} &= (7.9 \pm 0.3) \cdot 10^{-5} \text{ eV}^2.\end{aligned}$$

- **SK, K2K and MINOS:** The Super-Kamiokande (SK) experiment consists of the observation of atmospheric neutrinos resulting from hadronic decay in the upper atmosphere. Depending on the zenith angle, SK observes a  $\nu_\mu$  disappearance while the  $\nu_e$  measurement completely fits the data.

The K2K (KEK to Kamiokande) experiment uses a  $\nu_\mu$  beam produced in an accelerator at KEK through:  $\pi \rightarrow \nu_\mu \mu^+$  and the Super-Kamiokande detector, placed 250 km away from the accelerator, to observe a  $\nu_\mu$  disappearance. The experiment setup is defined so that:

$$P(|\nu_e\rangle \rightarrow |\nu_e\rangle) \cong 1.$$

The MINOS (Main Injector Neutrino Oscillation Search) experiment consists of a neutrino beam produced at FERMILAB (Fermi National Laboratory) and two detectors located 1 km and 375 km away from the target. From the comparison of the reconstructed neutrino energy spectrum at the near and far locations the oscillation parameters  $|\Delta m_{23}|$  and  $\sin^2(2\theta_{23})$  are extracted.

The oscillation observed by all these experiments is then:

$$\nu_\mu \rightarrow \nu_\tau$$

The common results are [12, 1]:

$$\begin{aligned}\sin^2 \theta_{23} &= 0.50_{-0.07}^{0.08} \\ \Delta m &= 2.4_{-0.6}^{0.5} \cdot 10^{-3} \text{ eV}^2.\end{aligned}$$

where  $\Delta m = |m_3^2 - \frac{m_1^2 + m_2^2}{2}|$ .

The physical goals of the T2K experiment are then as follow:

- A measurement of  $\sin^2 2\theta_{23}$  and  $\Delta m_{23}$  to improve the accuracy by observing  $\nu_\mu \rightarrow \nu_\mu$  disappearance
- A first measurement of  $\sin^2 2\theta_{13}$  by observing  $\nu_\mu \rightarrow \nu_e$  at the atmospheric wavelength.

- Have a confirmation of  $\nu_\mu \rightarrow \nu_\tau$  via the observation of neutral current events.

The  $\nu_\mu$  beam will be produced in Tokai through pion decay after a proton collision with a graphite target. Since T2K is a  $\nu_e$  appearance experiment, a detector which can extremely well separate  $\nu_e$  from  $\nu_\mu$  signals is mandatory. The detector is Super-Kamiokande (SK) located about 1000 m water equivalent underground in the Kamioka mine (Gifu) and 295 km away from the  $\nu_\mu$  production site.

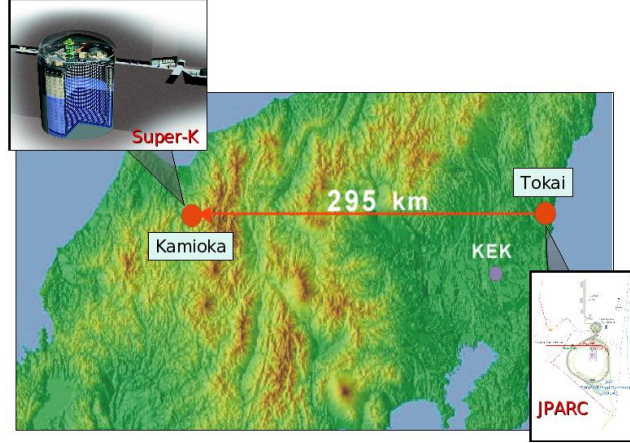


Figure 2: View of the long baseline experiment [4]

## 2.1 Kinematics of the neutrino beam from pion decay: the off-axis technique

The off-axis technique is used to select the energy of the T2K neutrino beam. It comes from the kinematic of the 2-body decay of charged pions,  $\pi^+ \rightarrow \mu^+ \nu_\mu$ . Figure 3 shows the kinematic of the pion decay.

The neutrino energy is then given by:

$$(P_\pi - P_{\nu_\mu})^2 = P_\mu^2 \quad \Rightarrow \quad E_{\nu_\mu} = \frac{m_\pi^2 - m_\mu^2}{2(E_\pi - p_\pi \cos \theta)}$$

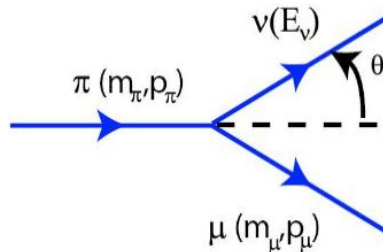


Figure 3: Pion decay (laboratory frame)

In the pion center of mass system (labelled by a star), the neutrino energy is given:

$$E_{\nu_\mu}^* = \frac{m_\pi^2 - m_\mu^2}{2m_\pi} \approx 30 \text{ MeV}$$

Applying the Lorentz boost,  $\Lambda(\beta)$ , to the 4-vector impulsion:

$$\Rightarrow E_{\nu_\mu} = \gamma E_{\nu_\mu}^* (1 + \beta \cos \theta^*) \quad (9)$$

$$P_{\nu_\mu}^* = \Lambda(\beta) P_{\nu_\mu} \quad \Rightarrow E_{\nu_\mu} \cos \theta = \gamma E_{\nu_\mu}^* (\beta + \cos \theta^*) \quad (10)$$

$$\Rightarrow E_{\nu_\mu} \sin \theta = E_{\nu_\mu}^* \sin \theta^*$$

$$\Rightarrow \cos \theta^* = \frac{\cos \theta - \beta}{1 - \beta \cos \theta} \approx \frac{1 - \theta^2 \gamma^2}{1 + \theta^2 \gamma^2}$$

where the approximations :  $\cos \theta \simeq 1 - \frac{\theta^2}{2}$  and  $\beta \simeq 1 - \frac{1}{2\gamma^2}$  are used since small angles are considered ( $\theta \ll 1$ ) and the pions are relativistic.

Considering now the equation (9) at first order so that  $\beta \simeq 1$ . We have then:

$$E_{\nu_\mu} \simeq \gamma E_{\nu_\mu}^* \left( 1 + \frac{1 - \theta^2 \gamma^2}{1 + \theta^2 \gamma^2} \right) = E_{\nu_\mu}^* \frac{2\gamma}{1 + \theta^2 \gamma^2} \equiv E_{\nu_\mu}(\theta)$$

It follows, for  $\theta = 0$ , that  $E_{\nu_\mu}(0) = 2\gamma E_{\nu_\mu}^*$ .

If  $\theta \neq 0$ :

$$\frac{\partial}{\partial \gamma} \left( \frac{2\gamma}{1 + \theta^2 \gamma^2} \right) = \frac{1 - \theta^2 \gamma^2}{(1 + \theta^2 \gamma^2)^2} = 0 \Leftrightarrow \gamma = \frac{1}{\theta}$$

The maximum energy is then found when  $\gamma = 1/\theta$  which implies an upper kinematic limit for the neutrino energy equal to  $E_{\nu_\mu}^*/\theta$ , while the neutrino energy for an on-axis beam is determined by that of the parent pions (see figure 4).

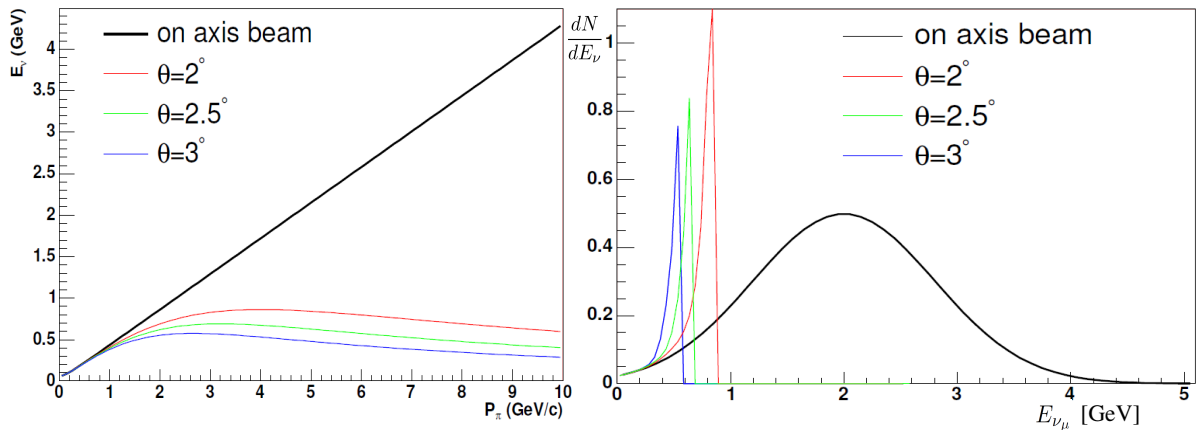


Figure 4: Left:  $E_{\nu_\mu}$  versus  $p_\pi$ . Right: on-axis and off-axis energy spectrum [1].

In order to maximize the oscillation effect,  $\theta$  is chosen so that the peak of the neutrino energy spectrum corresponds to the energy needed to be at the first maximum of the oscillation in Super-Kamiokande. In this case, one can see that the neutrino flux is considerably enhanced near the end-point, thus increasing the useful statistics and reducing the flux of the high energy neutrinos which only produce backgrounds.

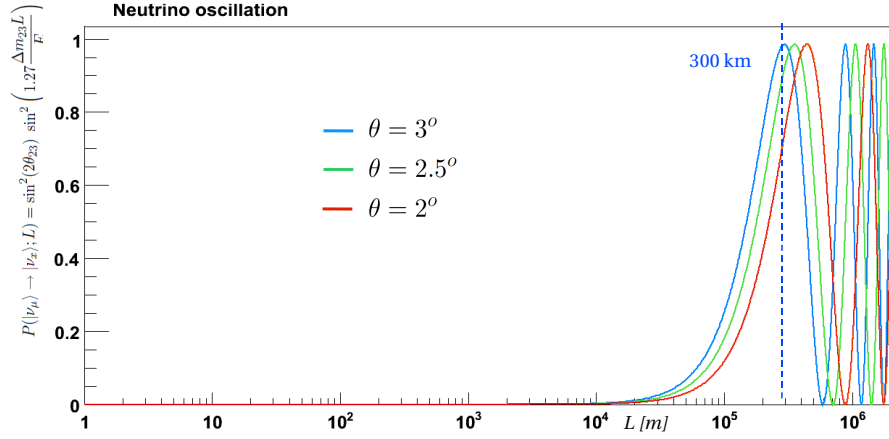


Figure 5: Probability to observe  $\nu_\mu \rightarrow \nu_x$ :  $P(|\nu_\mu\rangle \rightarrow |\nu_x\rangle; L) = \sin^2(2\theta_{23}) \sin^2(1.27\Delta m_{23}L/E)$  as a function of the distance  $L$  in [m]. The parameters are set as:  $E = 30 \text{ MeV}/\theta$ , with  $\theta = 3^\circ, 2.5^\circ, 2^\circ$ ,  $\Delta m_{23} = 2.4 \cdot 10^{-3} \text{ eV}^2$  and  $\sin^2 \theta_{23} = 0.44$ .

The maximum of oscillation, corresponding to the distance between Tokay and Kamiokande, is then found for  $\theta \approx 3$  (see figure 5).

## 2.2 The neutrino beam line

Figure 6 gives a schematic view of the different stages of production and detection of the neutrino beam. The 2KM detector is indicated only as information in the figure 6, since it will not be present in the first phase of the measurement.

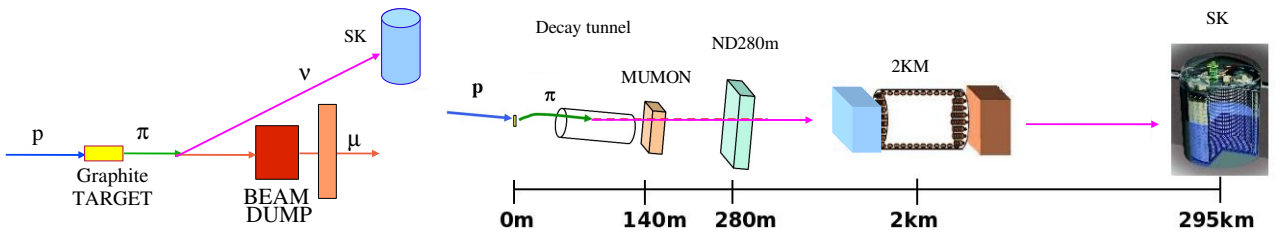


Figure 6: The neutrino beam line



### 2.2.1 The proton accelerator

Before the collision with the graphite target, the protons reach an energy of 30-50 GeV (30 GeV in the first phase of the experiment) by passing through different accelerators:

1. The 400 MeV LINear ACcelerator (LINAC)
2. The 3 GeV Rapid Cycling Synchrotron (RCS)
3. The 50 GeV Proton Synchrotron (PS)

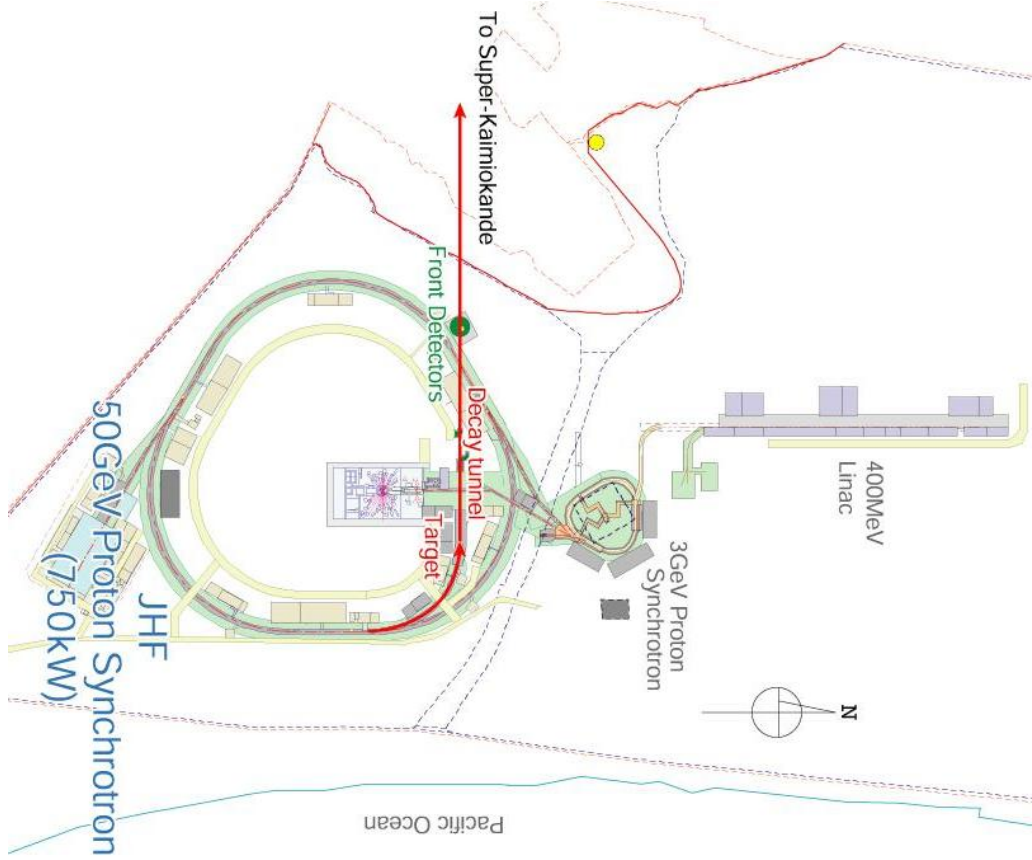


Figure 7: Overview of the different stages of the proton acceleration in the JPARC complex [5].

### 2.2.2 The target station

This station includes the graphite target, which is placed 12 m underground, and three magnetic horns which focus the pions produced in the proton interactions toward the decay tunnel. The dumping of protons onto the graphite target mainly produces pions and kaons. By changing the polarity of the magnetic field,  $\pi^+$  or  $\pi^-$  are selected and focused toward the decay tunnel as well as  $K^+$  and  $K^-$  which can produce electronic neutrinos by its 3-body decay ( $K^+ \rightarrow \pi^0 e^+ \nu_e$  or its charge conjugate mode respectively with 5% of probability). This kaon decay in electronic neutrino will give the main irreducible background at SK.

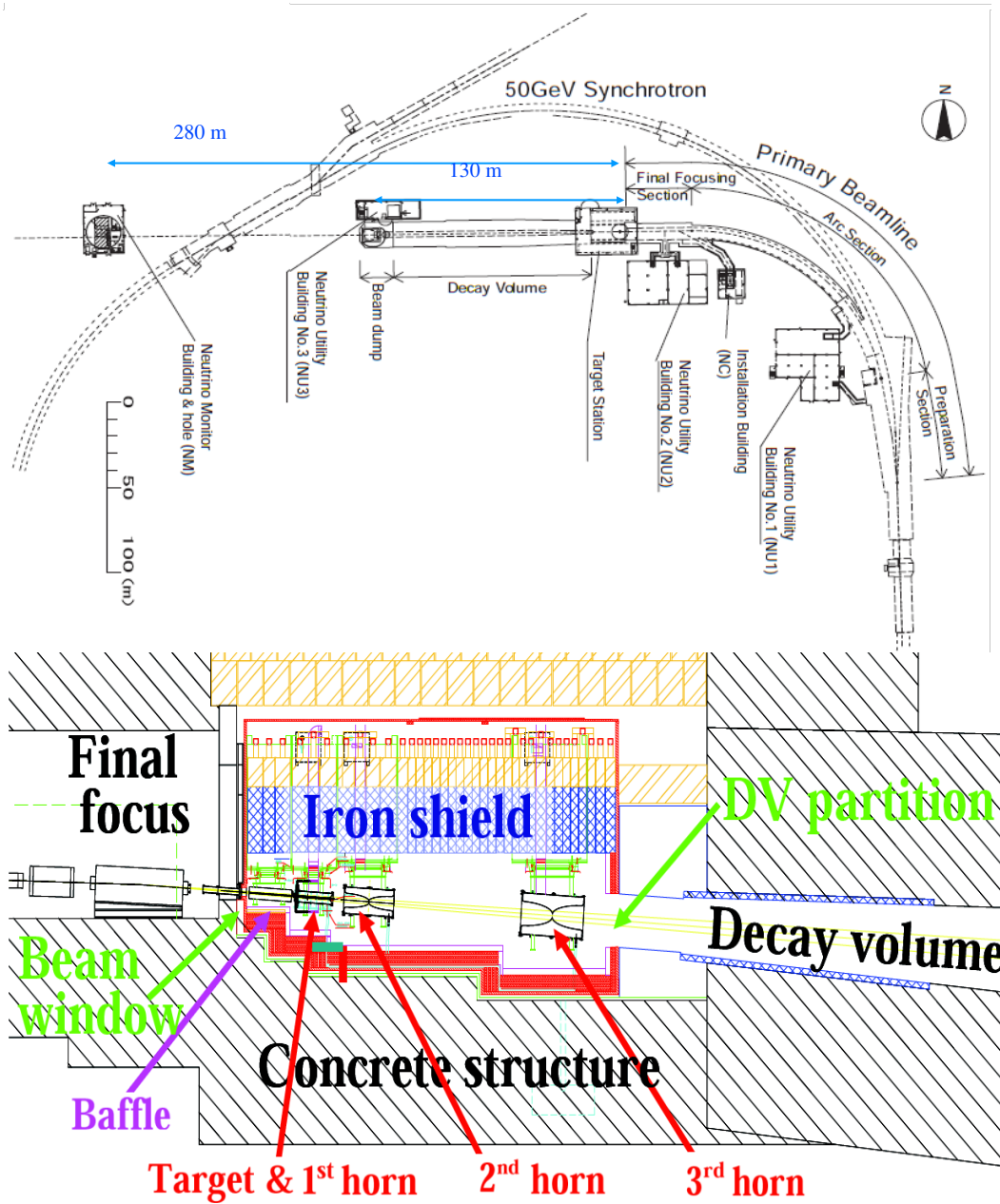


Figure 8: Overview of the different stations in JPARC (top) [5]. Target station (down) [5].

### 2.2.3 The decay tunnel

The decay tunnel is filled with Helium in which the secondary hadrons, mainly pions, decay. At the end of the tunnel is placed a beam dump, in graphite, which will stop the remaining hadrons. Its vertical dimension is made so that the neutrino beam direction can be off-axis by an angle between  $2^\circ$  and  $3^\circ$ . The result of the MINOS experiment should provide informations for the optimal off-axis angle (see figure 9).

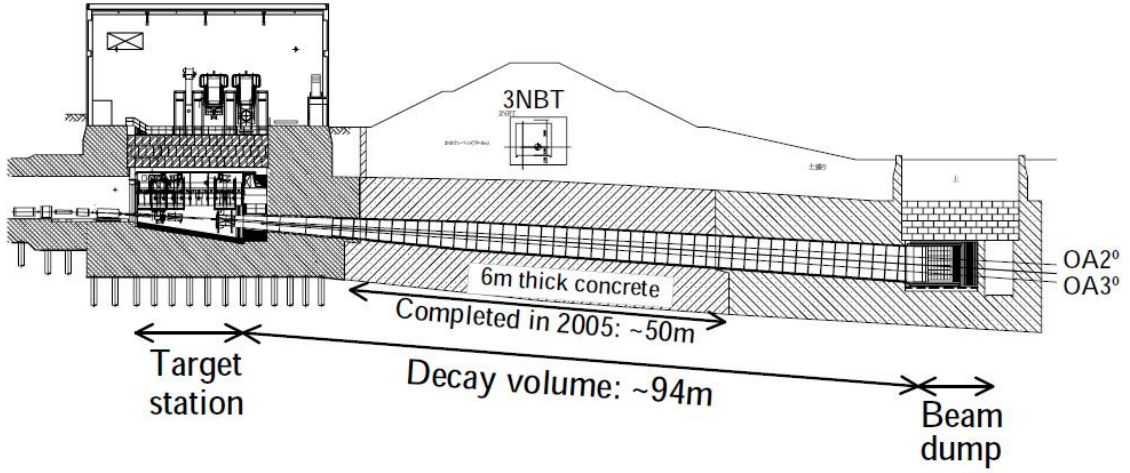


Figure 9: Decay Tunnel [5].

#### 2.2.4 The MUon MONitor (MUMON)

The direction of the secondary pion beam is monitored by the muon monitor measuring high energy muons escaping the beam dump. Since the muons are produced from the same parent particles as the neutrinos, the measurement of their properties also provides information about the neutrino beam. To reduce systematic uncertainties and assure the measurement at Super-Kamiokande, it is necessary to control the beam direction. Actually, in order to have  $\delta(\Delta m) \equiv 10^{-4} \text{ eV}^2$  [5], the precision on the neutrino beam direction has to be much better than  $1 \text{ mrad}$ . The muon detector will consist in ionisation chambers and diamond/silicium detectors. The MUMON sensitivity is limited to high energy muons (above  $5 \text{ GeV}/c$ ).

### 2.3 The ND280m Detector

The near detector complex, 280 m away from the hadron production target, contains, off-axis, a fine-resolution magnetized detector (ND280) and, on-axis, a neutrino monitor (N-GRID).

#### 2.3.1 The ND280

The ND280 is designed :

- to measure the flux, the spectrum and the interaction cross sections of  $\nu_\mu$ .
- to measure the flux and spectrum of  $\nu_e$  as well as the cross section of interactions that the far detector might misinterpret as coming from  $\nu_e$ .

It follows that a fine-grained detector is required.

The reconstruction of the neutrino energy at the near detector is based on Charged-Current Quasi-Elastic (CCQE) reaction ( $\nu_l + n \rightarrow l + p$ ), in which the neutrino energy,  $E_\nu$ , is reconstructed by

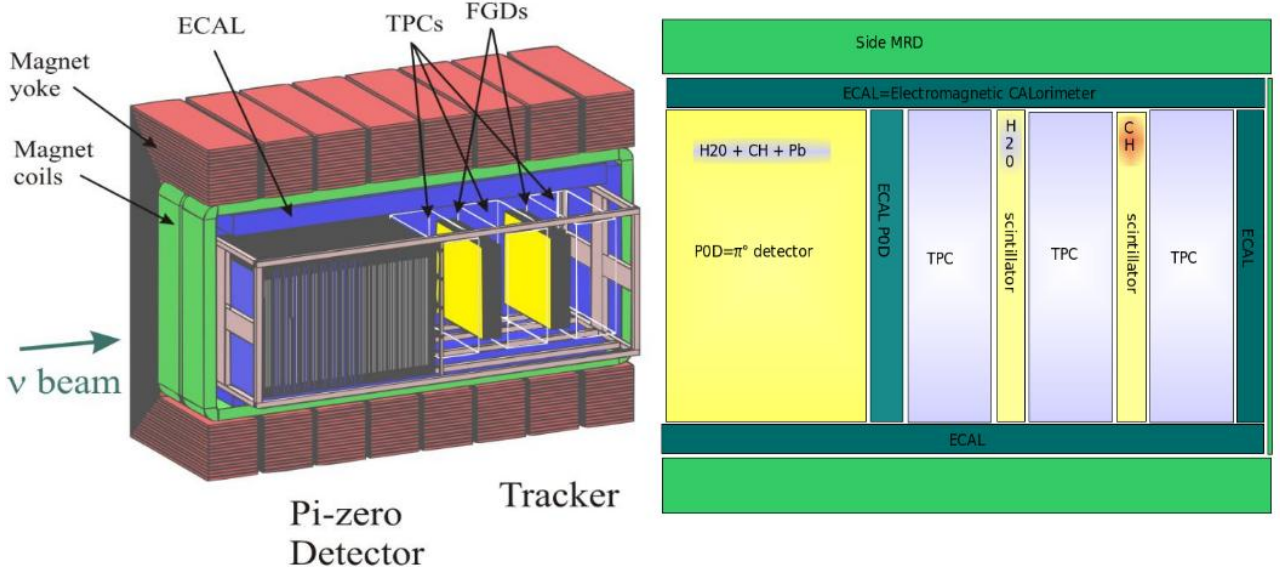


Figure 10: The ND280 off-axis detector overview [5](left). The ND280 tracking section design [4](right)

measuring the charged lepton energy,  $E_l$ , and angle  $\theta_l$  relative to the neutrino beam direction as shown by the following formula:

$$(P_n + P_\nu - P_l)^2 = P_p^2 \quad \Rightarrow \quad E_\nu = \frac{m_n E_l + m_p^2/2 - m_n^2/2 - m_l^2/2}{m_n - E_l + p_l \cos \theta_l}^4$$

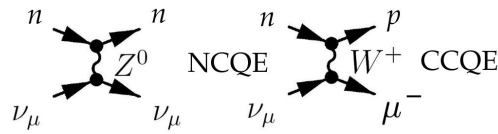


Figure 11: Feynman diagrams for neutral and charged current

The off-axis near detector consists of the following elements:

- Magnet: It comes from the UA1 experiment and will be operated with a magnetic field of 0.2 T to measure the momentum of charged particles produced by neutrino interactions in the near detector.
- Pi-Zero Detector (P0D): Located at the upstream end of the ND280, the P0D is optimized to measure the rate of the in-elastic neutral current  $\pi^0$  production, which represents the most important background for  $\nu_e$  appearance search.

<sup>4</sup>where  $P_n$ ,  $P_p$ ,  $P_l$ ,  $P_\nu$  are the 4-vector energy-impulsion of the neutron, proton, lepton and neutrino respectively.

The P0D consists of tracking planes composed of scintillating bars interleaved between lead foils. Inactive layers of passive water are also implemented in some sections of the P0D to measure oxygen nucleus interactions.

- The tracking detector: Downstream of the P0D is a tracker optimized to study neutrino interactions that will produce charged particles, such as muons, electrons, protons and pions:
  - $\nu_\mu$  charged current quasi-elastic interactions (CCQE) to measure the  $\nu_\mu$  flux and spectrum before the oscillation.
  - $\nu_\mu$  charged current in-elastic interactions (CC non-QE) that can be misinterpreted by SK as being CCQE interactions, and thus assigning an incorrect  $\nu_\mu$  energy.
  - $\nu_\mu$  neutral current inelastic interactions (NC non-QE) producing  $\pi^\pm$  that can be misinterpreted by SK as being CCQE interaction.
  - $\nu_e$  CCQE interactions to determine the  $\nu_e$  flux and spectrum which is an important background to  $\nu_e$  appearance at SK.

The tracking detector consists of two fine-grained detectors (FGDs) interleaved between three time projection chambers (TPCs).

\* *The two Fine Grained Detectors (FGDs):* the FGD modules, consist of layers of finely segmented scintillating tracker bars providing the target mass for neutrino interactions that will be measured by the TPCs. The CC interactions in the FGDs provide the measurement of the directions and ranges of recoil protons giving clean identification of CCQE and CC non-QE interactions which is impossible at SK since the proton velocity is usually below the Cherenkov threshold of 1050 GeV/c in water.

One FGD module will consist entirely of plastic scintillator, while the second will consist of plastic scintillator and water to determine the neutrino cross-sections on carbon and on water.

\* *The three Time Projection Chambers (TPCs):* the TPCs will measure the 3-dimensional momentum of the charged particles produced by CC interactions in the detector and provide the most accurate measurement of the neutrino energy spectrum. The 3D tracking and dE/dx measurement in the TPC will also give a clear identification of the particles.

- Electromagnetic CALorimeter (ECAL): The ECAL is a segmented Pb-scintillator detector surrounding the P0D and the tracker. Its main purpose is to measure those  $\gamma$  produced in ND280 that do not convert in the inner detectors and is critical for the reconstruction of  $\pi^0$  decays and for the  $e/\mu$  identification.
- Side Muon Range Detector (SMRD): It consists of plastic scintillators located in the side of the UA1 magnet. The SMRD goals are to measure the ranges of muons that exit the sides of the ND280, to provide a veto for events entering the detector from the outside and to provide a useful cosmic trigger for the calibration.

### 2.3.2 The N-GRID

The on-axis neutrino monitor (N-GRID) will be set to directly measure the direction of the neutrino beam in order to complete the observation of the muon monitor which observes only the small fraction of muons which have an energy greater than 5 GeV (see section 2.2.4). It consists of 7 + 7 identical units, arranged to form a grid which samples the beam on a  $8 \times 8 m^2$  area.

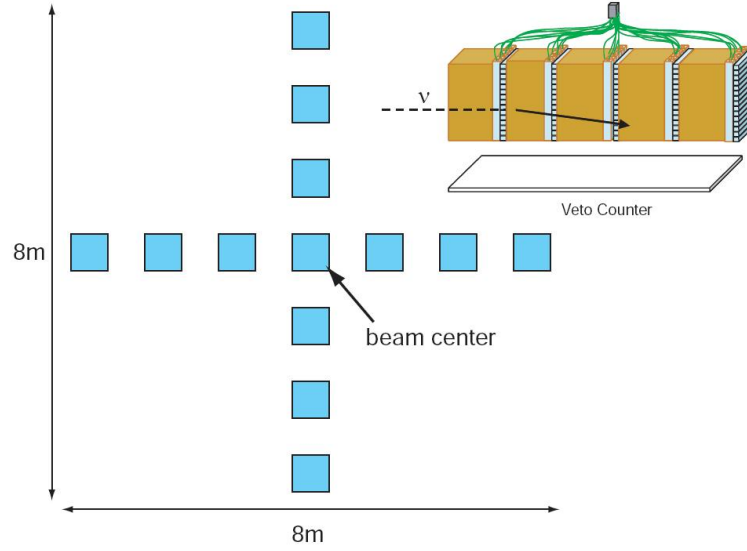


Figure 12: The N-GRID detectors setup at the near detector hall [5].

Iron is chosen as the target for the neutrino interactions, whereas the scintillators are used to detect the muons from the interactions.

## 2.4 The 2KM complex

The near detectors at 280 m are very different compared to Super-Kamiokande because of the different properties of the neutrino beam at the respective distances from the target. Two kilometers away from the target, the beam has mostly the same characteristics than at Super-Kamiokande with an event rate low enough to place a water Cherenkov device. Such detector set at the same off-axis angle, would reduce the systematic errors in the predictions by using the same algorithm and techniques as used in Super-Kamiokande to measure neutrino interactions on water.

With the 2KM complex, the expected systematic errors are predicted to be well below the required 10%.

Despite of the 2KM advantages, it will not be build for the first phase of the experiment. However, systematic errors have to be reduced and the NA61 experiment at CERN should be able to provide part of the information needed, namely a measurement of the properties of primary hadrons produced in the target.

## 2.5 The Super-Kamiokande detector

The Super-Kamiokande detector is a 50 kton tank of water situated approximately 1 km underground. The water in the tank acts as both the target for neutrinos, and the detecting medium for the by-products of neutrino interactions. The inside surface of the tank is lined with 11146 photomultiplier tubes (PMTs). In addition to the inner detector, which is used for physics studies, an additional layer of water called the outer detector is also instrumented with light sensors to detect any charged particles entering the central volume, and to shield it by absorbing neutrons produced in the nearby rock. To detect the high-energy particles which result from neutrino interactions, Super-Kamiokande



exploits the Cherenkov radiation emitted by the charged particles travelling with a velocity greater than the speed of light in the water.

Each PMT measures the total amount of light reaching it, as well as the time of arrival. These measurements are used to reconstruct energy and starting position, respectively, of any particles passing through the water. The array of over 11000 PMTs samples the projection of the distinctive ring pattern, which can be used to determine the direction of a particle. Finally, the details of the ring pattern - most notably whether it has the sharp edges characteristic of a muon, or the fuzzy, blurred edges characteristic of an electron, can be used to reliably distinguish muon-neutrino and electron-neutrino interactions.

The good spatial reconstruction capability of SK enables a good differentiation between the neutrinos coming from the sun or from the T2K neutrino beam.

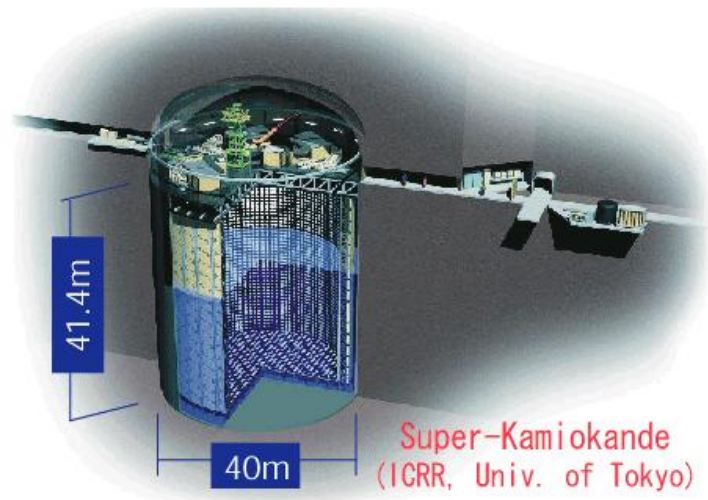


Figure 13: Super-Kamiokande detector [1].

### 3 Gas detectors and TPCs

#### 3.1 Physical processes in gaseous detectors

##### 3.1.1 Ionization

As heavy charged particles are passing through matter, they interact via electromagnetic interactions, primarily by ionisation. Doing so, they loose energy. This loss per unit length is described by the Bethe-Bloch formula, which can be divided into three physical regimes:  $1/\beta^2$ , relativistic rise and saturation.

Assuming that the shell electrons are free and initially at rest and that the charged particle mass is larger than the electron mass, we have [6]:

$$-\frac{dE}{dx} = Kz^2 \frac{Z}{A} \frac{1}{\beta^2} \left( \frac{1}{2} \ln \frac{2m_e c^2 (\beta\gamma)^2 T_{max}}{I^2} - \beta^2 - \frac{\delta}{2} \right) \quad K \equiv 4\pi N_A r_e^2 m_e c^2$$

where  $T_{max}$  denotes the maximum kinetic energy which can be transmitted to a free electron in a single collision,  $z$  the charge of the incoming particle in units of  $e$ ,  $\beta = \frac{p}{Mc}$ ,  $Z$  and  $A$  the atomic number and mass of the absorber,  $I$  the mean excitation energy,  $r_e$  the classical electron radius and  $\delta$  the density effect correction to the ionization energy loss.

The relation between the average energy required for the production of an electron-ion pair and the total number of electrons released per unit length  $n_t$  is given by:

$$n_t = \frac{dE}{dx} \frac{1}{W}.$$

$W$  has to be larger than the ionisation potential, since part of the deposited energy disappears through excitation energy and kinetic energy.

##### 3.1.2 Drift velocity

When a gas is ionised by a traversing charged particle, the electrons and ions recombine immediately unless an electric field is applied. In this latter case, the electrons drift to the anode and the ions to the cathode under the influence of the electric field and also of the magnetic field as described by the Langevin equation:

$$m \frac{d\vec{v}}{dt} = e(\vec{E} + \vec{v} \times \vec{B}) - K\vec{v},$$

where  $m$  denotes the charged particle mass,  $e$  the electric charge and  $K$  a viscosity coefficient. The  $-K\vec{v}$  term is caused by the scattering of the charged particles on the gas molecules with an average time between two collisions of  $\tau \equiv \frac{m}{K}$ .

The solution of this equation for  $t \ll \tau$  is:

$$\vec{v} = \frac{\mu |\vec{E}|}{1 + \omega^2 \tau^2} (\hat{E} + \omega \tau (\hat{E} \times \hat{B}) + \omega^2 \tau^2 (\hat{E} \cdot \hat{B}) \hat{B}),$$

where  $\hat{E}$  and  $\hat{B}$  are unit vectors,  $\mu = \frac{e\tau}{m}$  is the mobility in the gas and  $\omega = \frac{e|\vec{B}|}{mc}$  is the cyclotron frequency.



### 3.1.3 Diffusion

A charged particle diffuses isotropically away from its creation point because of its thermal energy. The transverse and longitudinal diffusion after a time,  $t$ , can be described by gaussian distributions:

$$T(x) = \frac{1}{\sigma_x \sqrt{2\pi}} \exp\left(\frac{-x^2}{2\sigma_x^2}\right) \quad \text{with } \sigma_x = D_t \sqrt{v_D t} = D_t \sqrt{z}$$

$$L(z) = \frac{1}{\sigma_l \sqrt{2\pi}} \exp\left(\frac{-z^2}{2\sigma_z^2}\right) \quad \text{with } \sigma_l = D_l \sqrt{z}$$

where the creation point is initialized to  $(x = 0, z = 0)$ ,  $D_t$  and  $D_l$  are respectively the transverse and longitudinal diffusion coefficient, and  $z$  the drift distance. The relation with the Einstein diffusion coefficient  $\tilde{D}$ <sup>5</sup> is:

$$\tilde{D} = \frac{D^2 v_D}{2}$$

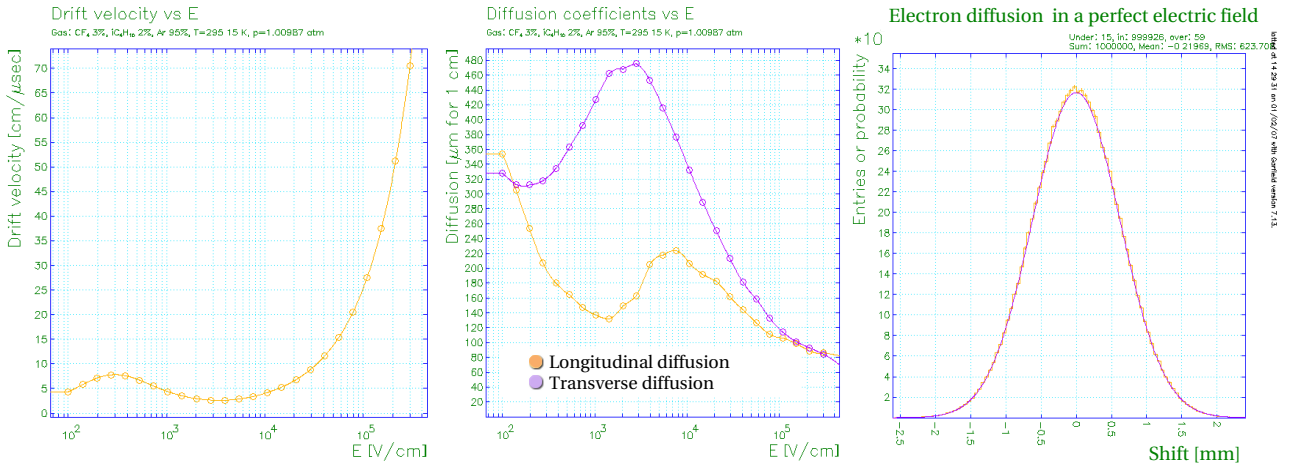


Figure 14: GARFIELD simulation of the drift velocity (left), diffusion coefficients (middle) and transverse diffusion distribution of an electron in a uniform electric field of 200 V/cm, for a drift distance of 4 cm in Ar : CF<sub>4</sub> : iC<sub>4</sub>H<sub>10</sub> (93 : 3 : 2), at  $B = 0$  T.

Assuming that free charges are conserved so that there is no recombination<sup>6</sup>, the diffusion coefficient,  $D$ , depends on the temperature,  $T$ , pressure,  $p$ , of the chosen gas mixture and on the mass of the charged particle,  $m$ :

$$D = \frac{2}{3\sqrt{\pi} p \sigma_{tot}} \sqrt{\frac{(KT)^3}{m}}$$

<sup>5</sup>where the Einstein relation is given by:  $\sigma = \sqrt{2\tilde{D}t}$

<sup>6</sup>This assumption is not always true in presence of O<sub>2</sub> since O<sub>2</sub> has a high attachment coefficient [13]

where  $\sigma_{tot}$  depends also on the gas and the type of the charged particle.

In a magnetic field, the longitudinal diffusion coefficient is unchanged, while the transverse diffusion coefficient is highly suppressed as described by the following formula:

$$D_t(B) = \frac{D_t(0)}{1 + \omega^2 \tau^2} \qquad D_l(B) = D_l(0)$$

### 3.1.4 Gas Amplification

Primary electrons accelerated by a drift field of 10 kV/cm gain sufficient energy between two inelastic collision to ionize the gas. The electrons released in the ionization can continue the avalanche process as long as the field strength is high enough.

The probability of an electron to ionize a gas mixture, in a given electric field, per unit length, is called the Townsend coefficient  $\alpha$ <sup>7</sup>.

The gain  $G$  of the amplification is then obtained by:

$$G = \frac{N(r)}{N_{r_0}} = \exp \left( \int_{r_0}^r \alpha(r) dr \right)$$

where  $r_0$  denotes the starting point of the avalanche and  $r$  the end point,  $N(r_0)$  the number of primary electrons and  $N(r)$  the number of electrons at the point  $r$ .

## 3.2 Principle of a Time Projection Chamber (TPC)

A TPC usually consists of a cylindrical drift volume with a central cathode and an anode at the two ends. In the case of a colliding experiment, the TPC contains an inner radius in which the beam pipe and inner detectors are placed.

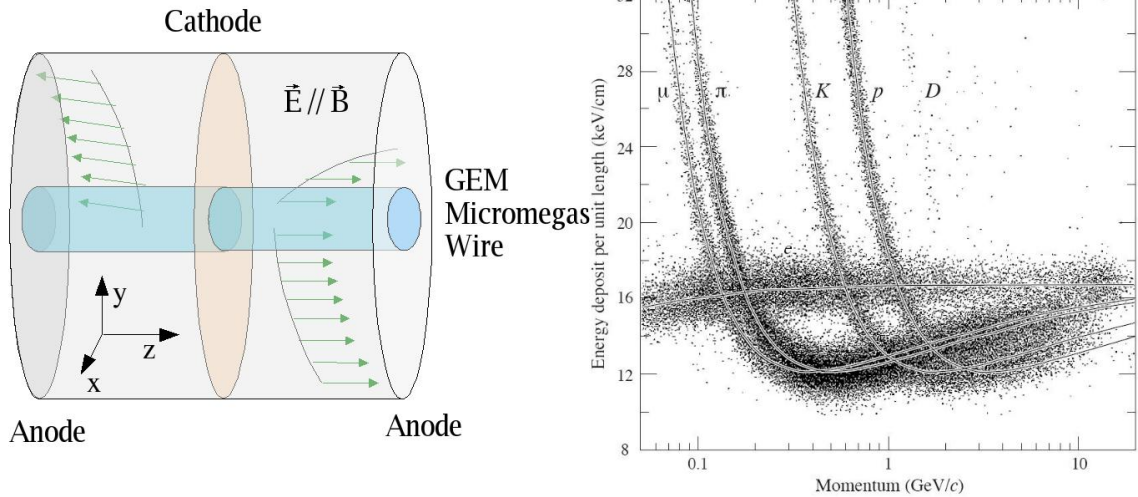


Figure 15: TPC scheme for a colliding experiment (left). PEP4/9-TPC energy-deposit measurement in multi-hadron events. The muons and pions are separated at low momentum [6] (right).

<sup>7</sup>Actually, the Townsend coefficient is directly related to the mean path of an electron,  $\lambda$ , by:  $\alpha = 1/\lambda$

The anodes are at ground, while the cathode is at a potential of about 10 kV. The walls of the volume are the field cage, which ensures a very homogeneous electrical field between the electrodes. The magnetic field is parallel to the electric field to suppress transverse diffusion. Without the magnetic field this diffusion would dominate, degrading the track and momentum reconstruction.

The electrons are released after the ionization of the sensitive gas volume and drift along the electric field to the anodes, while the ions drift toward the cathode.

An amplification device is placed in front of the anodes and creates an electron avalanche. The signal amplification can be done by multi-wire proportional plane, a Gas Electron Multiplier (GEM) or a MICRO-Mesh Gaseous Structure (MICROMEGAS).

The TPC provides:

- \* **3 dimensional track reconstruction**, by getting the  $xy$  information from the anode segmented in pads and the  $z$  coordinate delivered by the drift time. To obtain the  $z$  coordinate from the drift time, the drift field has to be very homogeneous. Because this coordinate is obtained via the drift velocity of the electron, it should have a moderate dependence on the drift field for a given gas mixture<sup>8</sup>.
- \* **The total momentum of a charged particle**, by measuring the radius,  $\rho$ , of the electron trajectory to get the transverse momentum<sup>9</sup>, and adding this information to the knowledge of the trajectory in the  $z$  plane.
- \* **The particle identification**: As the gain increase exponentially with the voltage between the anode and the amplification device, the amplified signal is proportional to the deposited energy. In consequence, the energy loss can be extracted by measuring the charge deposited on the readout pads. The energy loss combined with the measurement of momentum in the magnetic field provides then the particle identification.

The gas mixture should be chosen to minimize the capture of electrons by the molecules of electronegative impurities.

Due to the long drift distance ( $\sim 1\text{-}2$  m), and the fact that ions are heavier and much slower than electrons, ions can accumulate in the chamber. This effect can lead to electric field distortions and should therefore be avoided. To decrease this effect, the structure of the readout chambers is generally designed to avoid ions from escaping into the gas volume. A gas with a large drift velocity is also chosen in experiments with large interaction rate.

### 3.3 Multi-Wire Proportional Chamber

It consists of three layers of wires. The layer close to the anode plane is composed of amplification and field wires with positive and negative potential respectively.

The primary electrons from the drift volume follow the field lines towards the wires, where the field strength is high enough to start the gas amplification. This amplification process takes place in about 1 ns, then all electrons are collected onto the wires, while the positive ions start to drift towards the cathode.

The main component of the signal is due to the remaining ions. Since the ion drift is very slow compared to electrons, the signal is quite long. The signal can be read out at the wires, but the

<sup>8</sup>In particular, the relation of the  $z$  coordinate and the drift time is given by:  $z = v_{drift} \cdot (t_z - t_0)$ , where  $t_z$  is the time when the signal arrives at the anode and  $t_0$  is the starting time known from the outer scintillators or from a bunch crossing in the case of a colliding experiment [14]

<sup>9</sup>The transverse momentum is easily obtained from the following formula:  $p_t[GeV] \approx 0.3 \cdot B[T] \cdot \rho[m]$  [14]

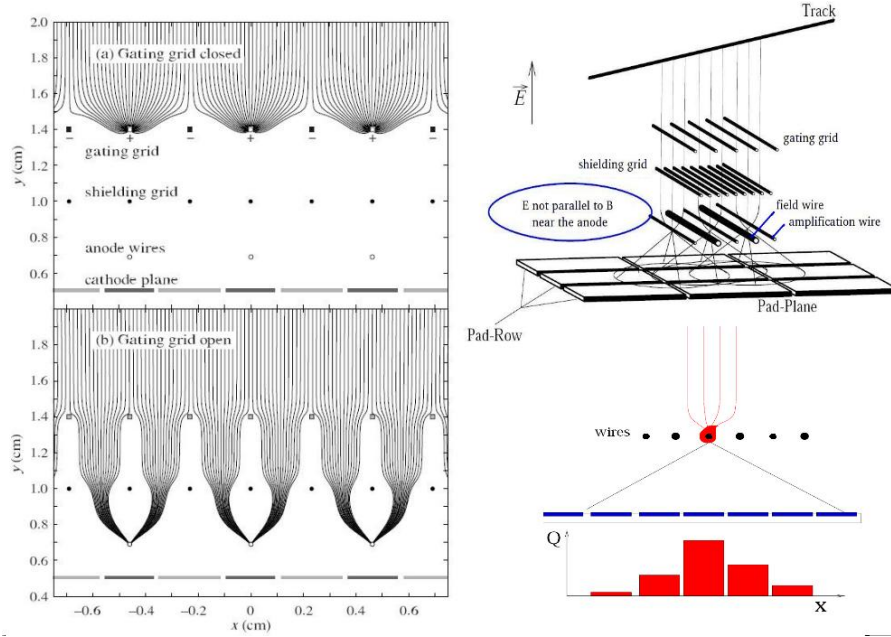


Figure 16: Mechanism of the gating grid in order to suppress the ion back flow [7] (left). Principle of a multi-wire proportional chamber and charge smearing over the readout pads [8, 9] (right).

achieved resolution can be improved, when the signal induced on the anode plane is also used. This signal is spread over several pads and allows a good coordinate reconstruction.

The role of the field wires, which have a larger diameter than the amplification wires to ensure that no gas amplification occurs close to them, is to stabilise the electric field. The second wire plane is the shielding grid, which terminates the drift volume. The gating grid, next to the drift volume, has the task to prevent the ions, that are also created in the gas amplification process, from drifting back to the sensitive volume.

When the gate is opened, the applied potential is equivalent to the field potential, while if the difference of potential between two neighbouring wires is  $\cong \pm 80$  V, the gate is closed and no electrons nor ions can pass through. With the help of external detectors, events are analyzed. Depending on which type of desired event, the voltage is applied to the gating grid to close or open the gate.

### 3.4 Micro-Pattern Gas Detectors (MPGDs)

Micro-pattern gas detectors are replacing conventional wire chambers in many applications. In these devices electron gas amplification is obtained in very high fields generated by modest voltages (300-400 V) across  $50 - 100 \mu\text{m}$  structures suitable for large-area applications. Typically gains of  $10^3 - 10^4$  are achieved with many gases under standard conditions. Gas Electron Multipliers and MICRO-Mesh Gaseous structure are two example of MPGDs.

#### 3.4.1 The Gas Electron Multipliers (GEMs)

GEMs consist of a thin Kapton foil coated on both sides with copper and pierced with a high density of holes which diameter is about  $70 \mu\text{m}$  at a  $140 \mu\text{m}$  pitch. The Kapton thickness is, in general,

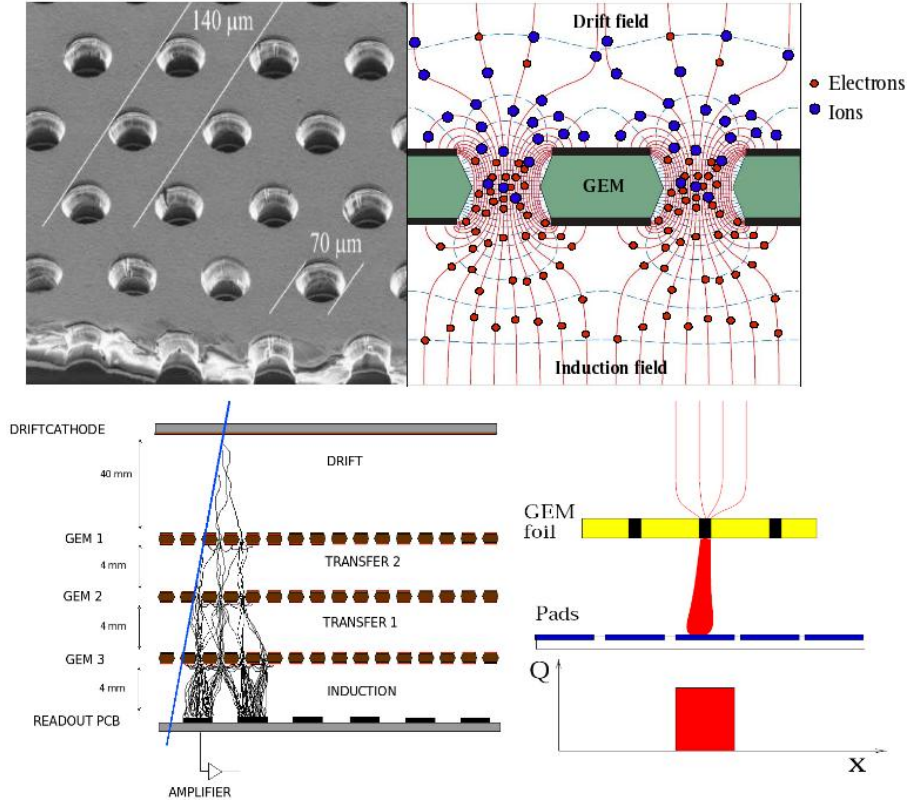


Figure 17: Microscopic photo of the foil (up-left). Detail of electric field lines (solid) and equipotentials (dashed) in the region of GEM holes. Most of the positive ions produced in the hole drift back to the top side of the GEMs [8](up-right). 3-GEM principle (down left) [10]. Transverse diffusion is suppressed in high magnetic field, therefore the charge is collected by very small number of pad [9](down right)

around 50  $\mu\text{m}$ , while that of the copper layer is around 5  $\mu\text{m}$ . A potential difference is maintained between the opposite sides of the copper sheet, so that electron avalanches occur in the holes.

Figure 17 shows that part of the field lines ends at the lower side of the GEM, so that only a fraction of the electrons are read out at the anode. This effect implies the introduction of the effective gain which denotes the ratio between the electrons measured at the anode and the primary ones.

A standard GEM chamber consists of a conversion gap, one or several transfer gaps, an induction gap and finally a readout structure (see figure 17). However, a chamber with one GEM foils is more difficult to run stably and therefore two or three GEM foils are generally stacked at a lower voltage.

### 3.4.2 The MICRO-Mesh Gaseous Structure (MICROMEAS)

A Micromegas detector is a parallel plate avalanche gas chamber with a single amplification stage. It consists of a conversion gap and a narrow amplification region, which is located between a cathode mesh and the anode readout structure underneath. The width of the conversion gap is dependent on the gas choice. In the case of the ND280 TPC it is 128  $\mu\text{m}$  thick for operation with a gas mixture of Ar:CF<sub>4</sub>:iC<sub>4</sub>H<sub>16</sub> (95:3:2).



The cathode mesh is made of a thin metallic micro-mesh ( $5\ \mu\text{m}$  width) with a hole-pitch smaller than  $50\ \mu\text{m}$ . The anode readout structure is a simple Printed Circuit Board (PCB) with either a strip or a pad structure. A segmentation into pads has been chosen for the T2K experiment. The micro-mesh-anode distance is kept constant by small insulating pillars with a pitch of  $0.8\ \text{mm}$  (ND280) in order to obtain a uniform electric field in the amplification gap.

The high voltage, applied on the drift electrode and the wire mesh, forms the electric field. The electrons released in the drift volume, by an ionizing particle, follow the electric field lines towards the micro-mesh and are multiplied in the high field region of the amplification gap.

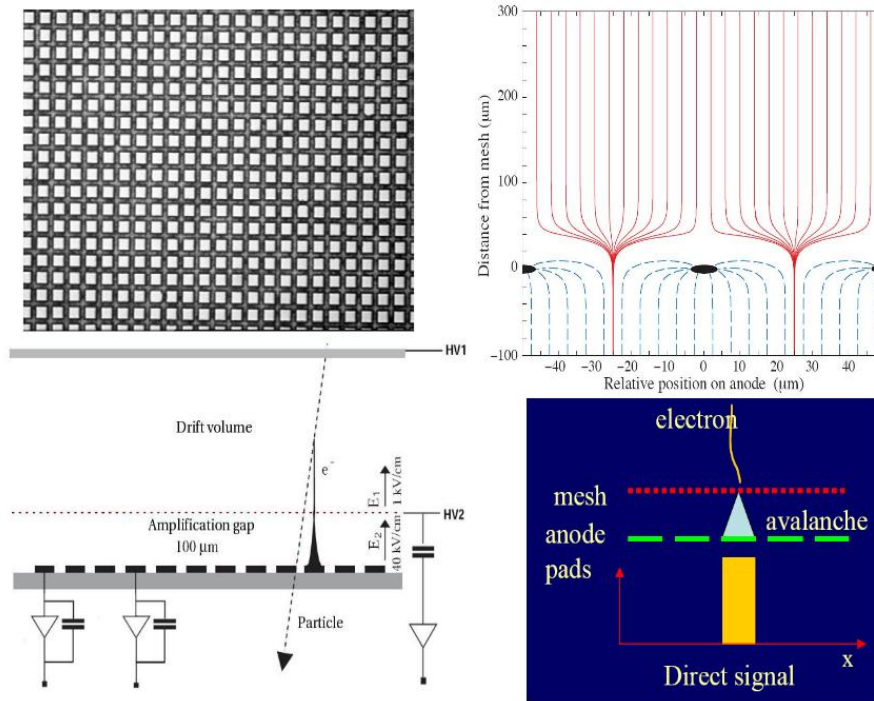


Figure 18: Micro-mesh (up left). GARFIELD simulation of the electron (solid) and positive ion (dashed) drift lines in a Micromegas avalanche region (up right) [6]. Micromegas principle (down left). Transverse diffusion is suppressed in high magnetic field (down right)

Due to the electric field configuration, the ions are collected rapidly on the micro-mesh, since the conversion gap is very small. The ions drifting in this region induce a short signal on the readout and are collected indeed in a  $200\ \text{ns}$  period.

The field configuration in the amplification gap of the detector exploits the saturating characteristics of the Townsend coefficient. The gain shows a maximum as a function of the gap for a given voltage applied. In standard operation conditions, this optimal gap is a few tens of microns. This makes the gain independent of the gap at first order, and can lead to a good potential for  $dE/dx$  resolution [8].

### 3.4.3 Differences between the various readout schemes

Micro-pattern devices for TPC provide :

- **Higher rate capability:** The MWPC voltage drops at  $< 10^4 \text{ kHz/mm}^2$ , while MPGDs provide a rate capability over  $10^5 \text{ Hz/mm}^2$  (single GEM  $> 10^3 \text{ Hz/mm}^2$ , multi-GEM  $> 10^5 \text{ Hz/mm}^2$ ).
- **Intrinsic ion feedback suppression:** for typical drift fields of 100-300 V/cm and amplification fields of 40-70 kV/cm, most of the field lines originating at the anode end at the micro-mesh or at the GEM foil. As the diffusion is negligible for ions, the ions produced on these field lines do not go back to the drift volume and most of them will be neutralised on the mesh or GEM foil.
- **A direct electron signal**, which gives a better time resolution. However, since transverse diffusion is suppressed in high magnetic field, most of the charges are collected on one or two pads only. This degrades the spatial resolution in the xy plane (see figure 15) compared to the case of wires for which the induced cathode signal determined by the geometry provides accurate centroid determination with wide pads and then a good measure of track position.
- **Much smaller  $\vec{E} \times \vec{B}$  effects** than wires chamber for which the spacing of the wires is about a few mm. Since the electric field is radial near the wires, generating a spread of the electron cluster of more than 100 microns due to  $\vec{E} \times \vec{B}$  effects. This effect limits the MWPC resolution. It is reduced for MPGD because of their small amplification structures.
- **A simple design easy to build and eliminate the need of wire tension.**
- **A larger gain**, by multistage structure of the GEM.
- **An electron amplification independent of the gap, at first order, for Micromegas**, because of the Townsend coefficient saturation leading to a good dE/dx resolution.

In addition, Micromegas can be usable with a gas mixture containing  $CF_4$  as a quencher (avoid permanent discharges at low gain).  $CF_4$  responds much less to the neutron backgrounds than isobutane, methane, and other hydrocarbons. Such gas cannot be used in structures where fields of the order of a few kV/cm exist over a mm as in a wire readout.

### 3.5 The ND280 TPC resolution

The resolution of the TPC is limited by the diffusion of the drifting electrons. An upper bound on the diffusion is calculated using the standard Gluckstern parameterization, assuming a large number of measurements along the length of the track [5]:

$$D < \frac{\sigma_{pt}}{p_t} \sqrt{\frac{n_T L}{720}} (L[m]^2) \frac{0.3B[T]}{p_t[GeV/c]} \frac{1}{\sqrt{L_{drift}}} = 260 \frac{\mu m}{\sqrt{cm}}$$

where the diffusion component of the momentum resolution ( $\sigma_{pt}/p_t$ ) is required to be less than 5% at  $p_t = 1 \text{ GeV/c}$ ,  $n_T = 90$  ionization electrons per cm of gas (mainly argon) for a track measured over  $L = 60 \text{ cm}$  and for a drift distance of  $L_{drift} = 125 \text{ cm}$ .

## 4 The test bench

### 4.1 Test bench description

The test bench consists on a drift chamber with a Micromegas or a GEM module implemented on one side and a cathode on the other side. The chamber is held vertically and mounted on a support structure in front of x-y stages. The x-y stages are used to move a strong  $^{55}\text{Fe}$  source behind the cathode over each pad during the calibration. Two other weak sources of iron are fixed behind the cathode for a stability control in time.



Figure 19: GEM test bench (left). MICROMEAS test bench (middle).

There is a 10 mbars overpressure inside the box which is regulated through a bubbler filled with mineral oil. Pressure regulators, flow meters, bubblers and manometers are installed as described in figure 20. In figure 20, a red dashed frame indicates the part of the gas system used for the preliminary measurement at the University of Geneva. The complete gas system will be implemented at CERN to allow a higher calibration rate during the production.

The bubblers  $B2$  and  $B4$  are the bubblers regulating the overpressure, while  $B1$  and  $B3$  are the security bubblers which limit the pressure greater than 15 mbars.

In order to maximize the gain, the calibration box is filled with  $\text{ArCF}_4\text{iC}_4\text{H}_{10}$  (93:3:2), for the Micromegas test bench, while it is filled with  $\text{ArCO}_2$  (90:10) for the GEM test bench. According to the attenuation length in Argon for 6 keV photon, the drift distance is set at 40 mm which is the optimal length in order to cover the area of a single readout pad.



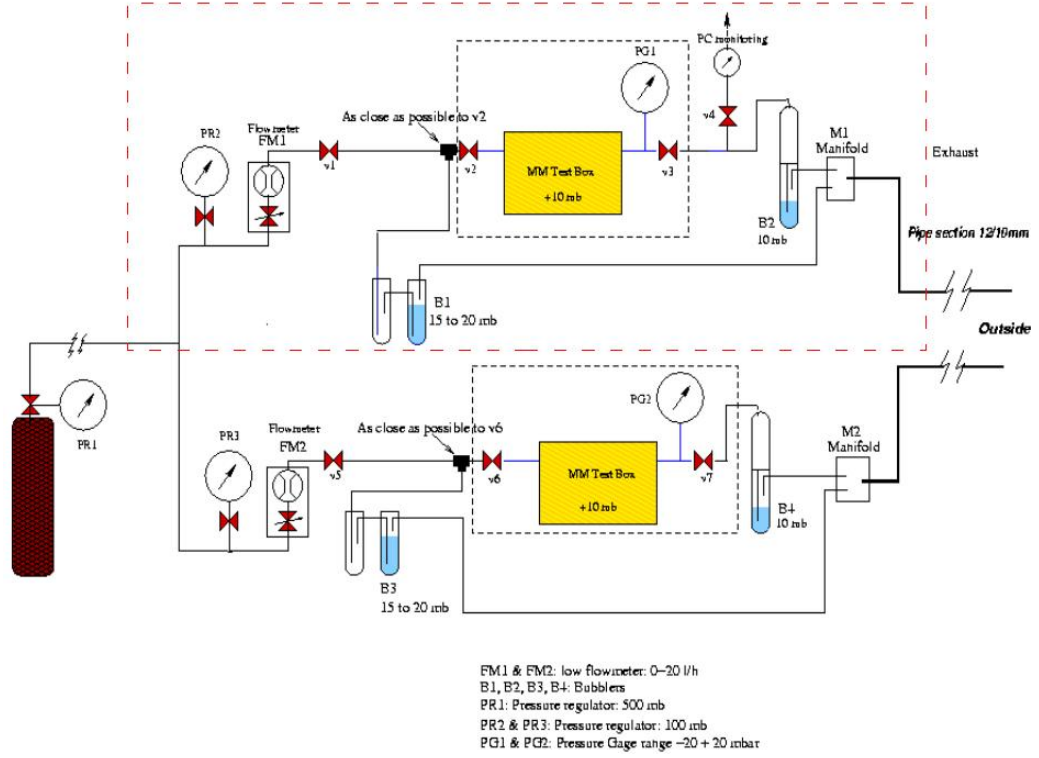


Figure 20: Gas system as it will be implemented at the CERN room.

#### 4.1.1 Module and calibration box for the GEM test bench

The GEM module (see figure 21) consists of two adjacent towers fixed on the same pad plane in order to double the size of the active area.

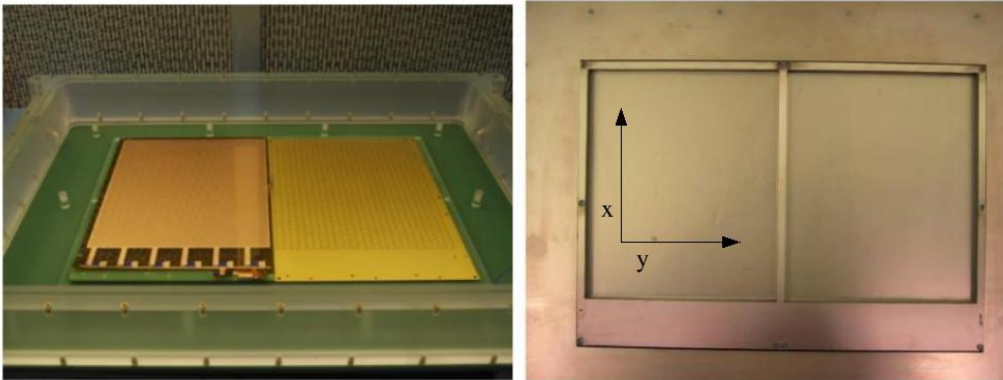


Figure 21: GEM tower mounted on the pad plane inside the Plexiglas box (left), top view of the module with guard ring and shield surrounding the active area (right).

The pad plane is divided in two sectors each with 720 staggered pads of dimensions  $8.3 \times 8 \text{ mm}^2$ . A tower is a stacking of three GEM foils retrieved from the LHCb experiment that are glued on 4 mm

thick FR4 frames. The total active area obtained with this configuration is  $240 \times 400 \text{ mm}^2$  and the dead zone between the two sectors is minimized to 8 mm wide.

A large copper coated FR4 frame (guard ring) is placed above the towers. The 11 mm thick frame surrounds the active area and allows the fixation of the GEMs onto the pad plane. The guard ring width is 8 mm except on one side where it is 50 mm wide.

At the level of the third GEM, 2 mm away from the border of the module, a large copper coated PCB (shield) surrounds the module in order to get a well defined potential at the level of the active area (see figure 21).

The calibration chamber has not been designed as a field cage so that there are no strips on the walls. This implies that external pieces in aluminum may have an influence on the electrostatics.

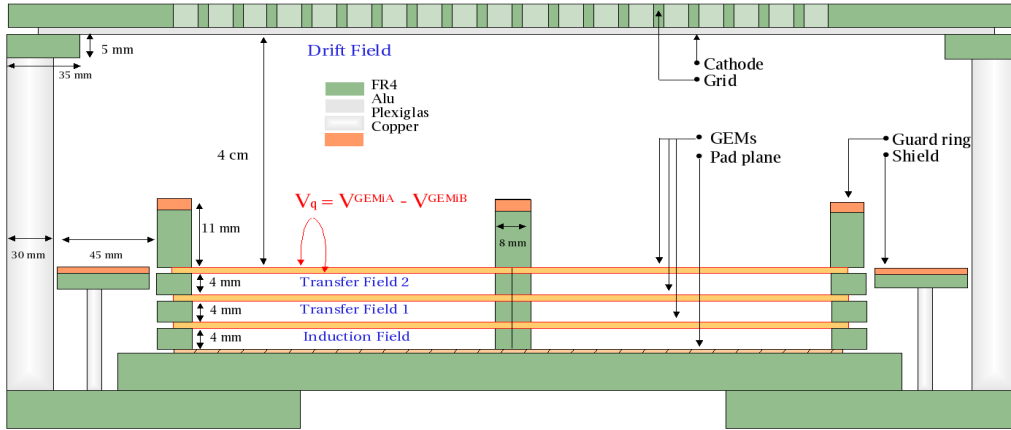


Figure 22: Calibration box, with its GEM setup

A G10 frame closes the box and supports the cathode which is a large aluminum coated mylar foil. A grid in G10, 5 mm thick, is fixed to this frame to secure the system and avoid any bending of the cathode.

#### 4.1.2 Module and calibration box for the Micromegas test bench

The Micromegas module constructed at CERN is built using a particular technique suited for compact and robust low mass detectors.

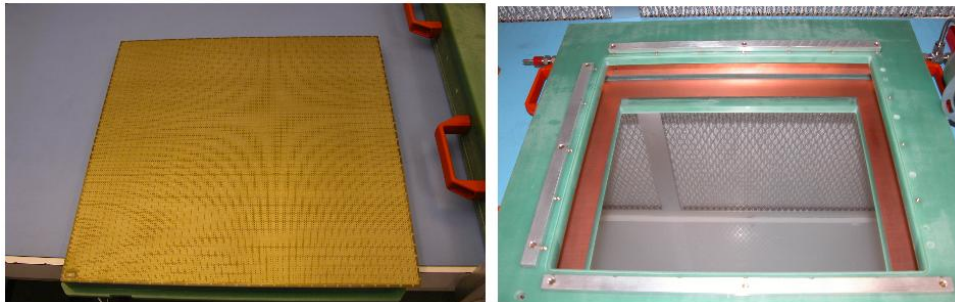
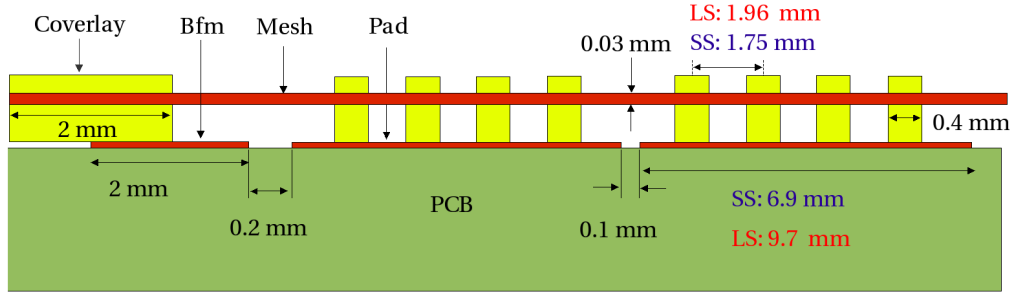


Figure 23: Micromegas module (left). Micromegas field cage (right)

The pad plane is made of  $36 \times 48 = 1728$  pads with dimensions of  $6.9 \times 9.7 \text{ mm}^2$ . On each pad, 12 pillars are supporting the mesh, which is 0.03 mm wide and placed 0.128 mm above the pad plane.



Warning: There are 3 pillars for the long size (LS) the corresponding sizes are written in pink

Figure 24: Schematic view of the beginning of the Micromegas module

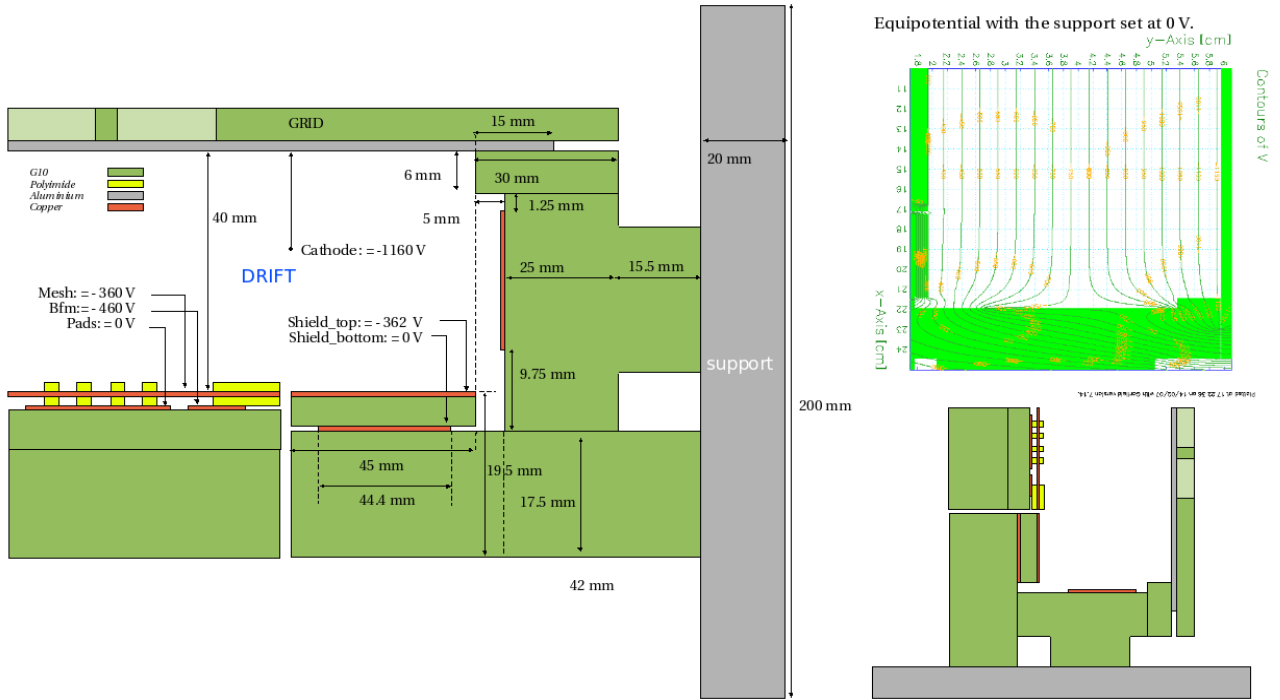


Figure 25: Schematic view of the bottom of the gas box with the additional strip (left). Real view of the box with its potential setting (right).

The calibration box design depends on different mechanical and electrostatic parameters. It must

be gas tight and easy to use since 72 Micromegas modules have to be calibrated. From the electrostatic point of view, uniform field lines above the pad plane is required to guarantee a good calibration. This last constraint implies accurate dimensions and adequate choice of the materials.

A shield surrounding the Micromegas active area is then necessary to get uniform field lines. This shield is made of a single G10 frame which is copper coated on both sides.

The top copper layer is set at the same potential than the mesh, while the bottom layer is grounded.

Besides, a strip is implemented over the walls of the box to suppress field distortions due to the aluminum support.

The cathode is an aluminum coated mylar foil fixed over a frame in G10 and protected by a grid as in the case of the GEM test bench.

#### 4.1.3 Data Acquisition (DAQ)

The final T2K DAQ is still being designed, therefore the DAQ used for the measurements done at CERN in 2006 has been recycled for the test bench. Each GEM or Micromegas module is read out by 6 sets of protection, inverter and ALTRO cards, the last containing 8 ALTRO chips developed for the ALICE TPC. The  $6 \times 128$  channels are linked by a bus PCB and read out by a USB to FEC interface card. For the Micromegas test bench, the ALTRO cards will be used until the T2K electronics will be available.

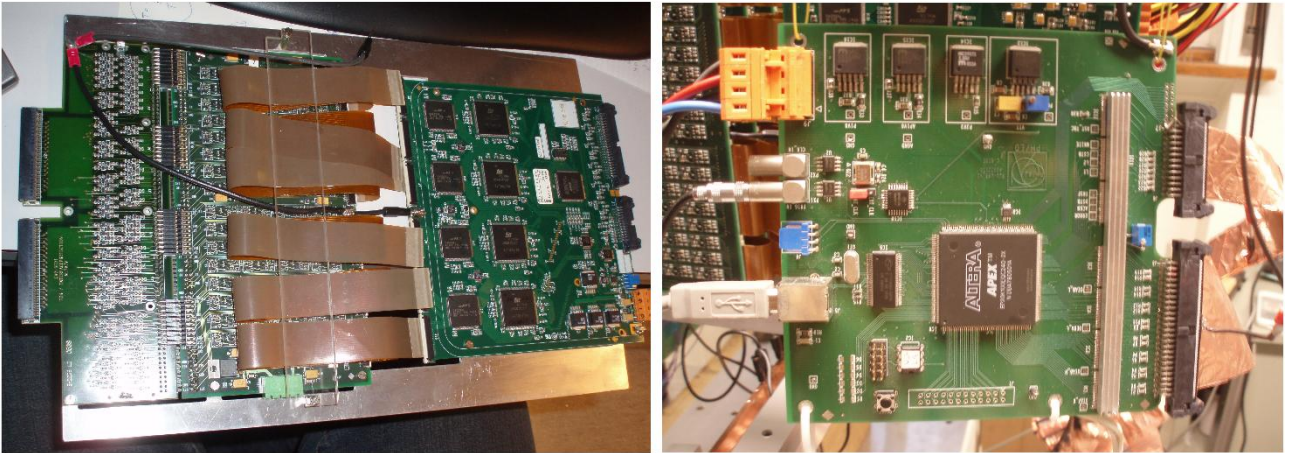


Figure 26: On the left side the protection and converter cards linked to the ALTRO card (left). USB to FEC (U2F) interface card (right).

In gaseous detectors the dead time is the time needed for the system recovery between two successive acquisition cycles. During this time the detector is not able to count or, in some cases, is not even sensitive to another event (spark chamber) and finally in other cases, the detector is sensitive but not able to give out information. The live time is then the difference between the total running time and dead time.

Many factors contribute to the total dead time:

- \* The intrinsic dead time of the detector.

- \* The analog front end electronics, for example the shaping time of the amplifier (in particular for the GEM and Micromegas readouts).

In the case of the GEM measurement, the time window was  $9 \cdot 10^{-5}$  s, and the acquisition rate was around 1.3 Hz, so that the DAQ live time had the nominal value  $\mathcal{L} = 0.012$  %. At the end of the measurement the acquisition rate has been improved and can reach now 7 Hz for both amplifier device.

#### 4.1.4 The iron source

The  $^{55}\text{Fe}$  decays into  $^{55}\text{Mn}$  by electron capture. Besides the neutrino emission, photons of 5.9 keV are emitted with a probability of 24.4 % and others with an energy of 6.49 keV (probability of 2.86 %). Hence,  $^{55}\text{Fe}$  source emits X rays with a probability of 27.3 %. Two peaks might be observable after the spectrum reconstruction: the 5.9 keV peak as a result of the photoelectric effect with the electrons of the K-shell and a peak at lower energy coming from the atom desexitation (when an electron of the L-shell transits to the K-shell). The activity of the source should be sufficient large to allow a reasonable time measurement and small pile up. As for the radio protection, the 6 keV X-rays emitted by the source are not considered dangerous, as they affect only the dead layer of the skin. Hence a very thin layer of material, even air, stops the core of the radiation.

The strong source activity, has a nominal value of 185 MBq, while the weak sources have a nominal activity of 37 MBq. The calibration need a strong source because of the dead time induced by the DAQ.

The GEM collimator tube prototype has a radius of 2.5 mm and is 6 cm long.

For a better pad-per-pad characterization the Micromegas collimator tube provides three different positions for the strong source:

$$L_{coll} = 8 \text{ cm}, 1.5 \text{ cm}, 0.5 \text{ cm}$$

The tube has a hole with a radius  $r_s = 2.5$  mm. For a better collimation, the exit hole is slightly closed with aluminum so that the hole at the end of the tube has a radius  $r_t = 1.1$  mm.

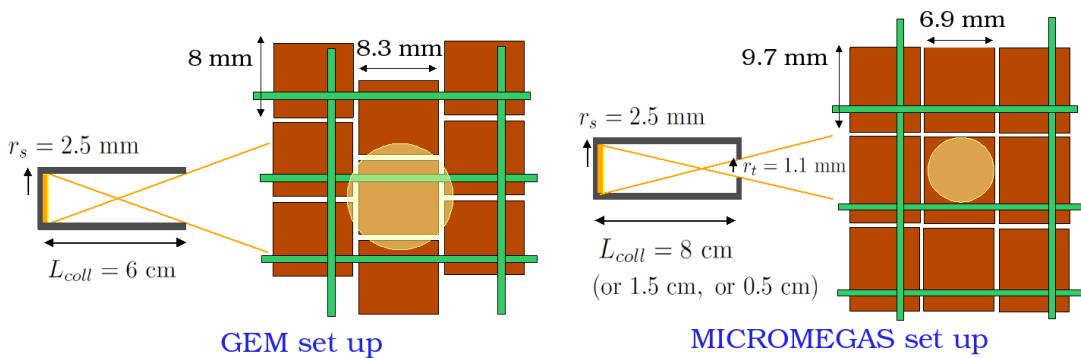


Figure 27: Collimator and grid setup for the GEM test bench and for the Micromegas test bench.

The reference weak sources are implemented with a lower collimation so that a few pads are fully illuminated but on a well-defined area. The rate should be high enough to allow a gain monitoring during the measurement.



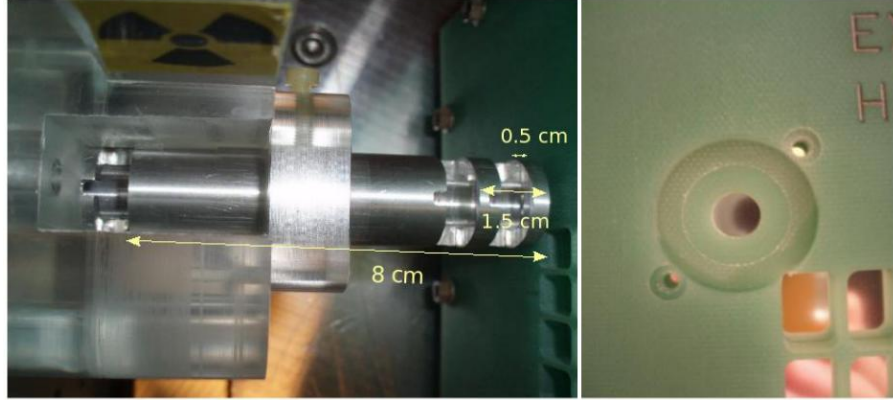


Figure 28: Top view of the strong source Micromegas collimator (left). Weak source support (right)

#### 4.1.5 X-rays attenuation

The radiation of the source is attenuated, first in the thin layer of Beryllium over the iron source, and then in the external medium (air), during the passage through the cathode (Mylar + Aluminum) and finally in the gas.

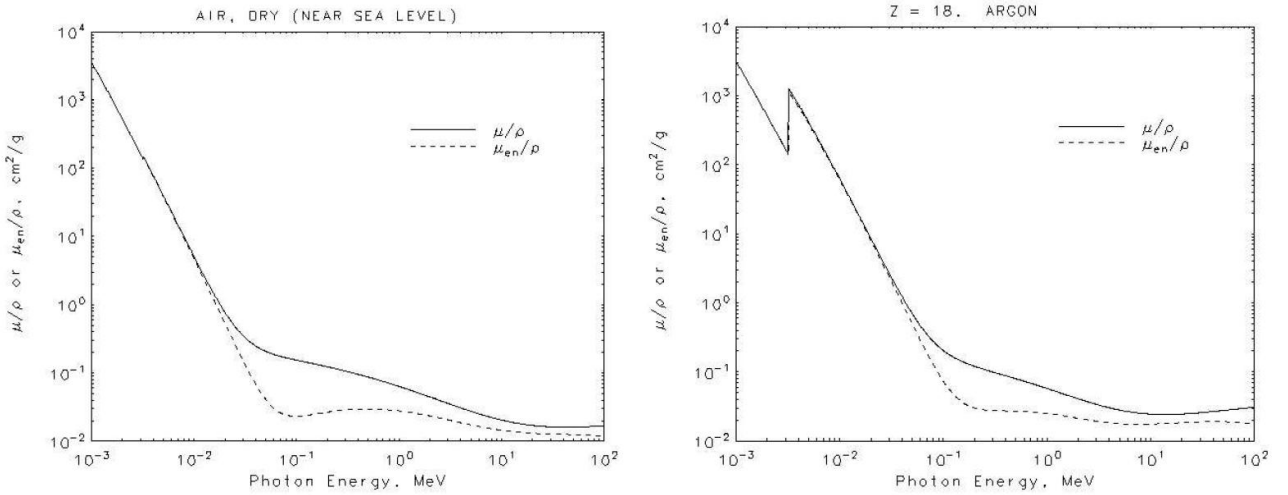


Figure 29: Attenuation length in air (left) and in Argon (right) as a function of the photon energy ??.

Figure 29 shows the attenuation length in air and Argon as a function of the emitted photon energy.

For 6 keV photons, the attenuation lengths and densities, for the different mediums used during the calibration, are given in Table 1:

Medium	$\rho$ [g/cm <sup>3</sup> ]	$\lambda$ [g/cm <sup>2</sup> ]
Air	0.0427	$1.205 \cdot 10^{-3}$
Ar	0.0039	$1.667 \cdot 10^{-3}$
Al	0.0864	2.7
Mylar	0.0591	1.39

Table 1: Attenuation length coefficient and densities

The survival factor,  $\mathcal{S}$  is then defined as:

$$\mathcal{S} = \frac{I}{I_0} = e^{-\mu x} = e^{-x\rho/\lambda}$$

The survival factor through the Beryllium window is then  $\mathcal{S}_{Be} = 0.88$ .

For 23  $\mu\text{m}$  of mylar, and 0.25  $\mu\text{m}$  of aluminum the respective survival intensity are  $\mathcal{S}_{my} = 94.7\%$  and  $\mathcal{S}_{Al} = 99.992\%$ .

The remaining intensity, before the X-rays reaches the internal box, is:

$$\mathcal{S}_{ext} = \mathcal{S}_{air} \cdot \mathcal{S}_{my} \cdot \mathcal{S}_{Al}$$

the values of the survival factor is given in Table 2 for different position of the strong source.

For Argon, the attenuation is very high, and, therefore after a drift distance of  $D = 4$  cm, the survival intensity is very low:

$$\mathcal{S}_{ar}(D) = e^{-\mu_{ar}D} = 0.18$$

The remaining intensity at the pad plane is given in Table 2.

Device	$L_{coll} + W$ [mm]	$\mathcal{S}_{air}$	$\mathcal{S}_{ext}$	$\mathcal{S}_{tot}$
MM	88	0.79	0.74	11.6 %
	23	0.95	0.89	13.9 %
	13	0.97	0.91	14.3 %
GEM	68	0.83	0.78	12.3 %

Table 2: Survival intensity after the passage through the collimator, the grid and the cathode ( $\mathcal{S}_{ext}$ ), and through the Beryllium window and Argon ( $\mathcal{S}_{tot} = \mathcal{S}_{ext} \cdot \mathcal{S}_{Ar}(D)$ ), where  $W$  is the addition of the grid thickness (6 mm) and the space between the grid and the collimator (2 mm).

For a nominal activity  $A_{nom}$  with a probability of photon emission,  $P_e = 27.3\%$ , the effective activity  $A_{eff}$  is then given by the following formula:

$$A_{eff} = A_{nom} \times P_e \times \mathcal{S}_{Be} = 44 \text{ MBq}$$

The area illuminated over the pad plane depends on the collimation tube and the source position. Figure 30 describes the different dimensions used.

The number of converted photons detected in the box per time unit is:

$$N_\gamma = \mathcal{S}_{ext} \cdot A_{eff} \cdot \mathcal{L} \cdot \int \int \mathcal{S}_{Ar}(y, z) \cdot \mathcal{I}(y) dy dz$$

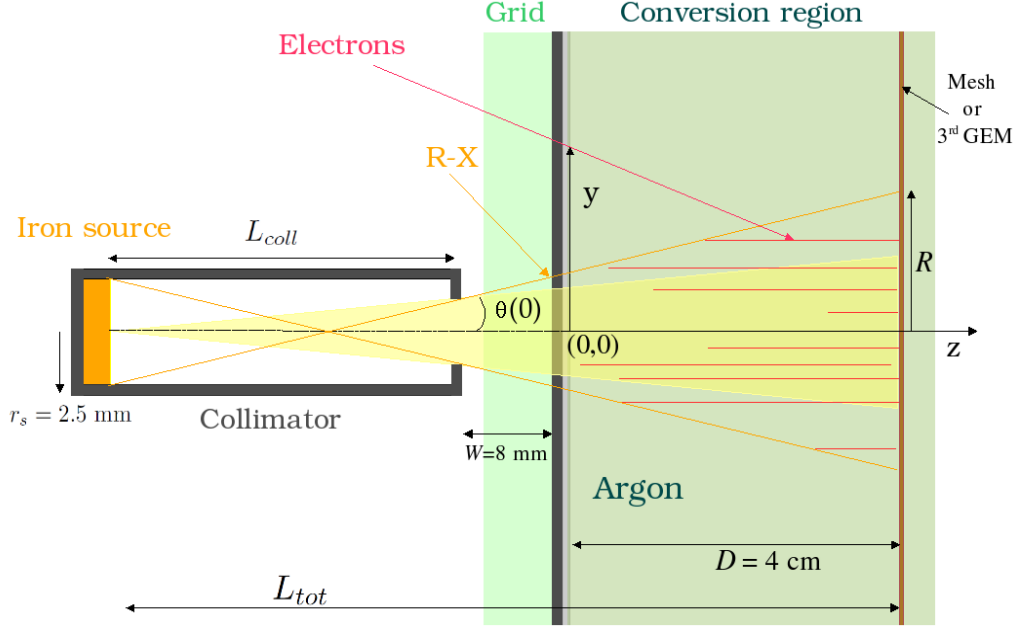


Figure 30: Schematic view of the collimator and the spot on the micro mesh (or 3<sup>rd</sup> GEM).  $\theta(0)$  denotes the maximum angle of a punctual source placed at  $y = 0$ .

where  $\mathcal{L}$  is the DAQ live time and  $\mathcal{I}$  the respective fraction of solid angle:

$$\mathcal{I}(y) = \frac{I(y)}{I_{tot}} = \frac{\int_0^{2\pi} \int_{-\theta(y)}^{\theta(y)} \sin(\theta) d\theta d\phi}{4\pi}.$$

Considering a punctual source placed at  $y = 0$ , so that:

$$\theta_0 \equiv \theta(0) = \text{atan}\left(\frac{r_t}{L_{coll}}\right) \text{ and } r_0 = L_{tot} \cdot \tan \theta_0,$$

where  $r_0$  is the corresponding spot radius and  $L_{tot} = L_{coll} + W + D = 108$  mm. Then:

$$N_\gamma = \mathcal{S}_{ext} \cdot A_{eff} \cdot \mathcal{L} \cdot \mathcal{I}(0) \int_0^D e^{-\mu_{ar} \cdot z} \cdot \mu_{ar} dz = \mathcal{S}_{ext} \cdot A_{eff} \cdot \mathcal{L} \cdot \mathcal{I}(0) \cdot (1 - \mathcal{S}_{ar}(D))$$

Assume now that the source is not punctual, the survival factor  $\mathcal{S}_{Ar}$  depends on the photo-emission point,  $(z - W - L_{coll}, y)$ . In a perfect uniform electric field with negligible transverse diffusion, the  $y$ -location of the electron conversion corresponds to its arrival position. The distribution of the arrival position is shown in figure 31 for a strong source centered at  $y = 0$ .

Since there is no smaller hole at the end of the GEM collimator to have a better collimation, the spot radius is bigger and the distribution of the electrons different compared to the one obtained with the Micromegas collimator. In all cases, the arrival electron distribution is bigger at the center than at the edges.



Device	$L_{coll}$ [mm]	$\theta(r_s)$	$R$ [mm]	$\theta_0$	$\mathcal{L}$	$N_\gamma$
MM	80	2.6 °	3.44	0.8 °	0.063 %	0.80
	15	13.5 °	13.6	4.2 °	0.063 %	27.35
	5	35.75 °	38.5	12.4 °	0.063 %	245.31
GEM	60	4.8 °	6.8	2.4 °	0.012 %	1.45

Table 3: Maximal extension of the spot,  $R$ , and number of photons detected in electrons per second,  $N_\gamma$  depending on the source position in the Micromegas or GEM collimator.

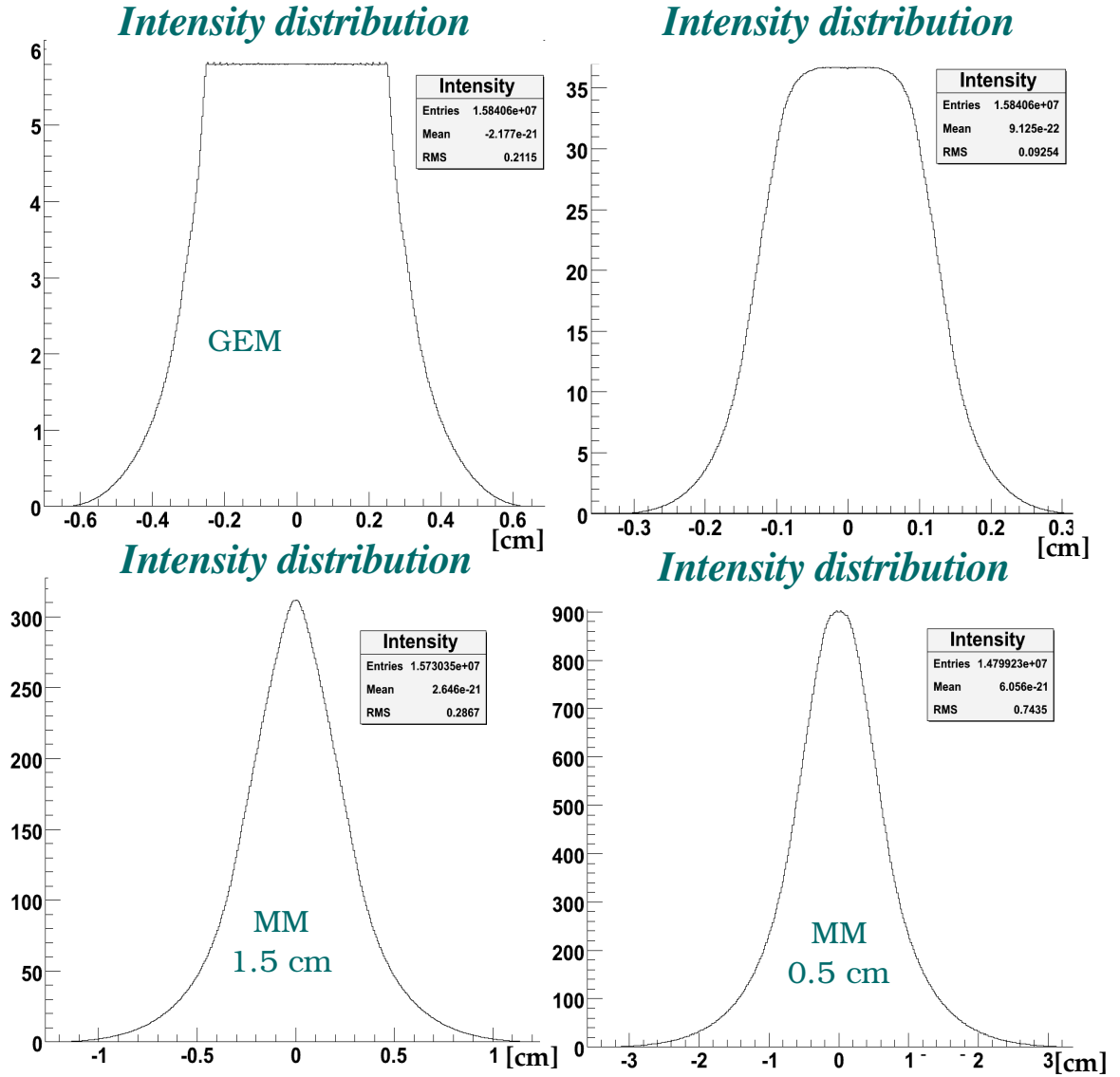


Figure 31: Spot radius distribution depending on the collimator.

#### 4.1.6 Effective coverage

The effective coverage of the source at the level of the first GEMs (or micro mesh) and at the pad plane, is found taking into account the transverse diffusion coefficient in the respective gas. Let's  $D_d$  be the transverse coefficient in the drift region, and  $D_t$  the transverse coefficient in the transfer and induction regions. For released electrons at the level of the cathode, the transverse diffusion implies a maximal shift of 0.9 mm for  $\text{ArCO}_2$  and 1.2 mm for  $\text{ArCF}_4\text{iC}_4\text{H}_{10}$  for 4 cm drift <sup>10</sup>. Hence, the transverse diffusion is too small to influence the spot radius determined then mostly by the collimator geometry.

For a transfer field of 2000 V/cm the transverse diffusion is, in the case of the GEMs,  $384 \mu\text{m}/\sqrt{\text{cm}}$ . For the Micromegas, we have in the induction gap, a field of  $\frac{360 \text{ V}}{0.0128 \text{ cm}} = 28125 \text{ V/cm}$  which corresponds to a transverse diffusion coefficient of  $216 \mu\text{m}/\sqrt{\text{cm}}$ .

For the GEMs, since there are three layer separated with a distance,  $d = 4 \text{ mm}$ , the transverse diffusion over the pad plane increases the spot radius:

$$r_{spot} = R + 3\sqrt{d}D_t = 6.96 \text{ mm},$$

while for the Micromegas the spot radius does practically not change due to its very small induction gap.

---

<sup>10</sup>For a drift field of 200 V/cm,  $D_d = 310 \mu\text{m}/\sqrt{\text{cm}}$  for  $\text{ArCF}_4\text{iC}_4\text{H}_{10}$  and  $D_d = 220 \mu\text{m}/\sqrt{\text{cm}}$  for  $\text{ArCO}_2$

## 5 Electrostatic simulations for the test bench

### 5.1 Maxwell/GARFIELD Implementation

The overall geometry and boundary conditions are implemented using the Maxwell 2D program. Different geometries are used since only a two dimensional model is considered.

- The view in the z-y plane over one sector (long side of the GEMs see figure 21) and over the pad plane (long side Micromegas, see figure 32)
- View in the z-x plane the short side of the GEMs or Micromegas (see figures 21 and 24).

Maxwell is used to generate the field and potential maps. These maps are computed using a mesh method that can be refined to get higher computation precision. The solutions are given as an input

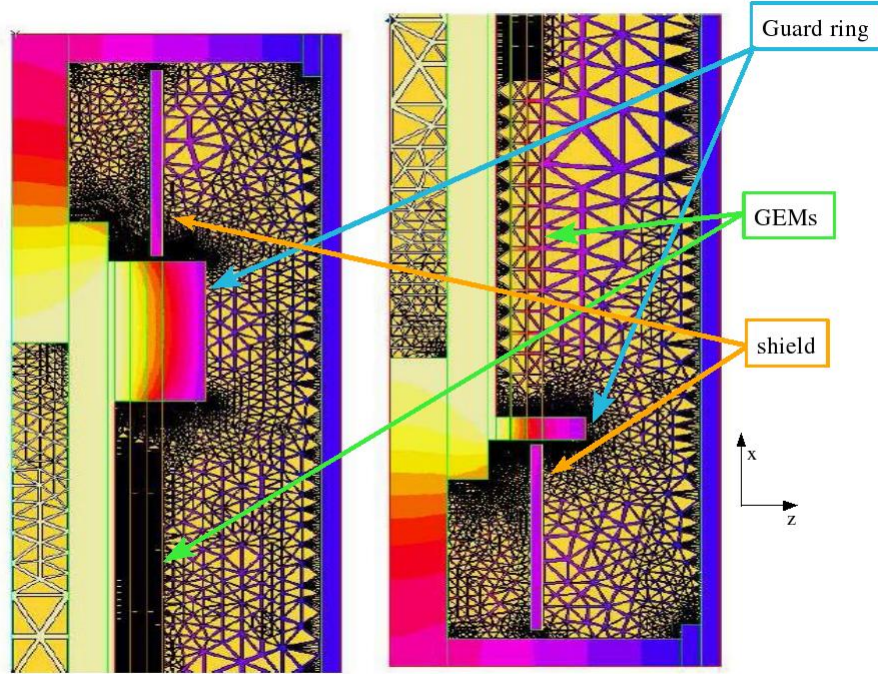


Figure 32: Example of mesh computation in the z-x plane at the level of the guard ring long side (left) short side (right); the mesh is refined where boundaries are more complex [11].

to the GARFIELD program which is used to compute different simulations related to the drift of the electrons in the gas. The gas map is computed via the interfaces of GARFIELD with the Magboltz and Heed programs.

### 5.2 Distortion quantification

To quantify the electric field distortions due to the field cage design, different simulations are performed. Interactions between electrons and the atoms of the gas are also taken into account and simulated by the GARFIELD program using a Monte Carlo drift method. In the following simulations, the average distance between two collisions,  $l$ , is the parameter used to tune the method.

The calibration of the method is made using a perfect box with ideal field lines. The sigma,  $\sigma_x$ , of the gaussian distribution of the difference between the initial and final position of a drifting electron has to be equal to  $D_t\sqrt{L}$ , where  $D_t$  is the transverse diffusion coefficient and  $L$  the drift distance.

Depending on the gas in use, the transverse diffusion is different: for ArCO<sub>2</sub> (90:10),  $D_t = 220 \mu\text{m}/\sqrt{\text{cm}}$ , while for ArCF<sub>4</sub>iC<sub>4</sub>H<sub>10</sub> (93:3:2),  $D_t = 310 \mu\text{m}/\sqrt{\text{cm}}$  for a drift field of 200 V/cm. The

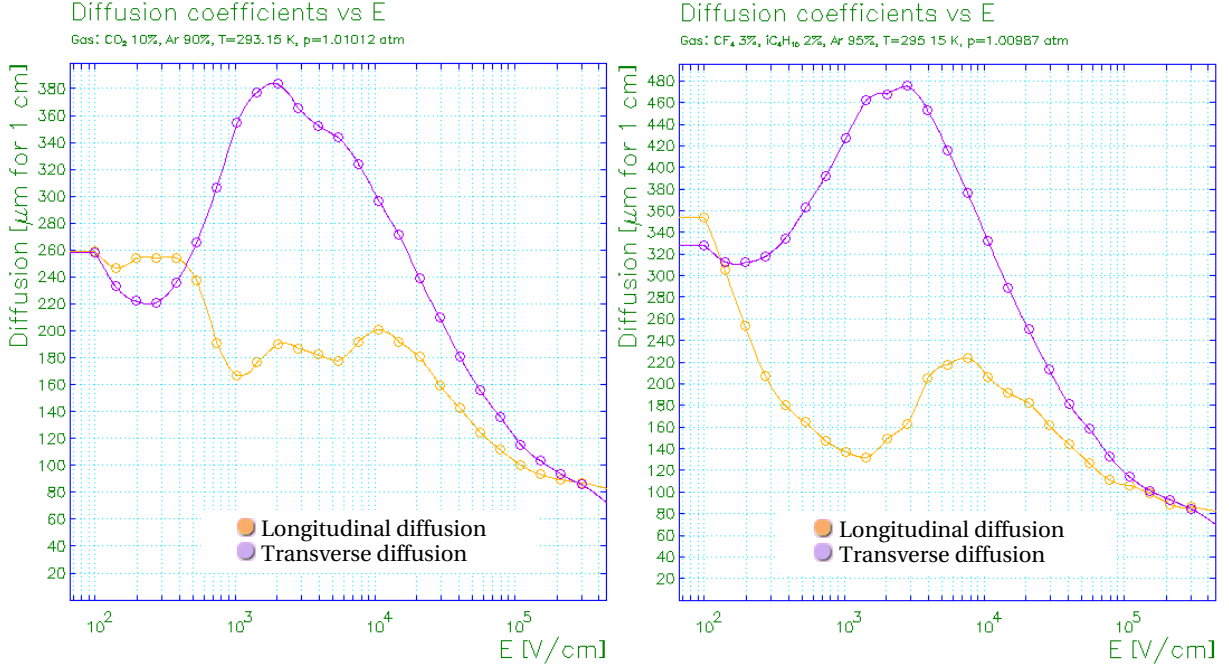


Figure 33: Transverse and longitudinal diffusion coefficients as a function of the drift field for ArCO<sub>2</sub> (90:10) (left) and for ArCF<sub>4</sub>iC<sub>4</sub>H<sub>10</sub> (93:3:2) (right).

GARFIELD average distance parameter,  $l$ , is then chosen so that  $\sigma_x = D_t\sqrt{L}$ .

From these simulations two quantities are constructed: the collection coefficient and the mean shift of an electron track, which reflect not only the electric field distortions but also the transverse diffusion of the electron in the gas.

### 5.2.1 Collection coefficient

The collection coefficient is computed as the ratio between the number of electron reaching the pad with the number of electrons uniformly generated 4 cm above the pad. In the reality, the electrons do not actually follow such uniform distribution at the level of the cathode as seen in the previous section. However, the information of this collection coefficient can be useful to quantify the electric field distortions. An electron illumination means that 100 electrons are sent uniformly along the pad per interval of  $\frac{\text{padwidth}}{100}$ . For each pad, 10 electron illuminations are performed in order to have a precision about 1 % for the collection coefficient in a perfect uniform electric field of 200 V/cm. Due to the transverse diffusion, the maximal value of the collection coefficient is not equal to 1 but smaller.

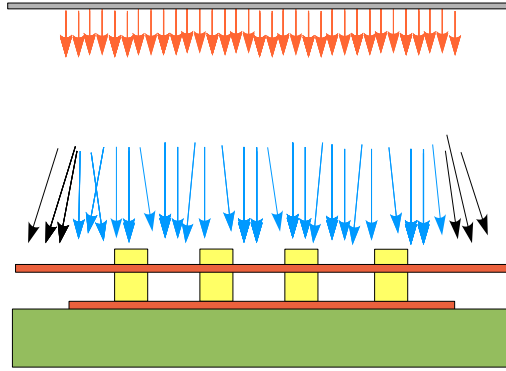


Figure 34: Schematic view of an electron illumination. The collection coefficient is defined as the ratio between the blue electrons reaching the pad and the orange electrons.

Since the drift distance is 4 cm, the mean value of the transverse diffusion is round about 0.62 mm and 0.44 mm for  $\text{ArCO}_2$  for a drift field of 200 V/cm<sup>11</sup>.

According to the initial position, the electron has a certain probability to be out of the pad. Theoretically, the collection coefficient is obtained by summing the area of the gaussian distribution limited by the pad width. It corresponds then to the case of a perfect uniform electric field, since a gaussian distribution is taken. The values found theoretically are 0.93 for  $\text{ArCF}_4\text{iC}_4\text{H}_{10}$ , and 0.96 for  $\text{ArCO}_2$ . As expected the maximal value of the collection coefficient for  $\text{ArCO}_2$  is greater because of its smaller transverse diffusion coefficient.

### 5.2.2 Mean shift of an electron

The difference between the position of the electron reaching the mesh and the initial position is called shift of an electron. The mean shift corresponds then to the mean value of the shift distribution of an electron.

The mean shift distribution along the pad plane is obtained with a statistic of thousand electrons implying an uncertainty of 20  $\mu\text{m}$ . In figure 35, the gaussian distribution is gotten in the case of a perfect uniform electric field and the mean value given with an uncertainty of 2 microns for a statistic of 50000 electrons. The gas used for this simulation is  $\text{ArCF}_4\text{iC}_4\text{H}_{10}$  (93:3:2), as expected the RMS of the distribution is 624  $\mu\text{m}$  corresponding wholly to the transverse diffusion of the electron after 4 cm drift<sup>12</sup>.

To have an accurate precision, the same process is used with 50000 electrons over the beginning, the middle and the end of few pads, specially to study the potential setting influence. From an ideal point of view, a zero value of the mean shift corresponds to a straight field line. For the first middle of the pad plane, a negative mean shift indicates a field line curved outside of the pad plane, while a positive mean shift corresponds to a field line curved toward the pad plane. By symmetry, one have the contrary states for the other side of the pad plane. Figure 35 shows this effect for a design with an aluminum base frame supporting the shield. The field cage of the test bench is made by using a single material (FR4), so that no such effect exists, as it can be seen in figure 35.

<sup>11</sup> Actually, the transverse coefficient for a drift field of 200 V/cm is  $310 \mu\text{m}/\sqrt{\text{cm}}$  for  $\text{ArCF}_4\text{iC}_4\text{H}_{10}$  (93:3:2).

<sup>12</sup> As explained in the previous section, the RMS of the gaussian distribution, in the case of  $\text{ArCO}_2$ , is smaller and would be around 440  $\mu\text{m}$  for a perfect uniform electric field.

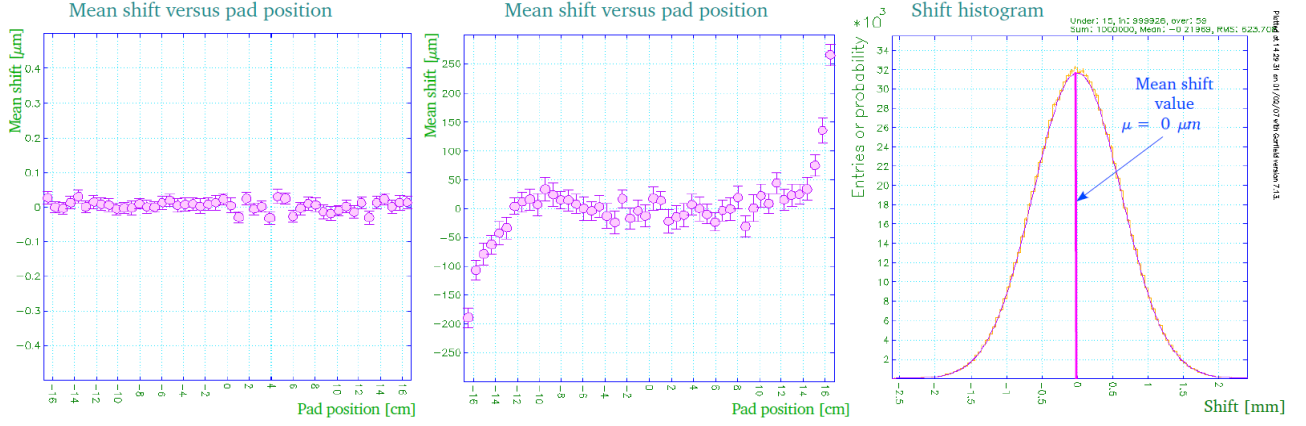


Figure 35: Mean shift value for 1000 electrons sent above the middle of each pad for different design: Micromegas test bench design (left), version with a grounded shield base in aluminum (middle). Histogram of the mean shift of an electron drifting along perfectly straight field lines (right).

### 5.3 Electrostatic simulations for the Micromegas test bench

#### 5.3.1 Influence of the external setup

As we can see in figure 19, the support of the gas box is an aluminum plate. Therefore a calibration box, as it is designed for the GEMs, induces too many distortions. Since aluminum is conductor,

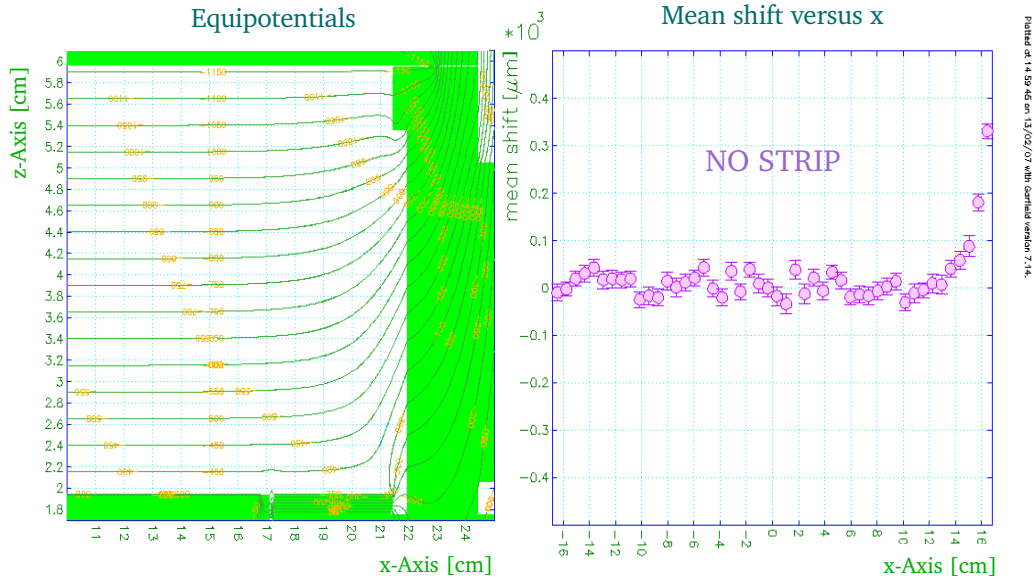


Figure 36: Electric field distortions without strip over the walls: equipotentials (left), mean shift value along the pad plane (right)

the support has to be grounded. The distortions due to the aluminum support are shown in figure 36, where no strip is implemented. The mean shift at the edge of the last pad, in this configuration, is:  $(470 \pm 10) \mu\text{m}$  (see figure 38). Such value is not acceptable. Therefore an additional strip is implemented to avoid the distortions and allow conductor support. Figures 36, 37 and 38 show clearly that a strip over the wall is necessary to get uniform field lines.

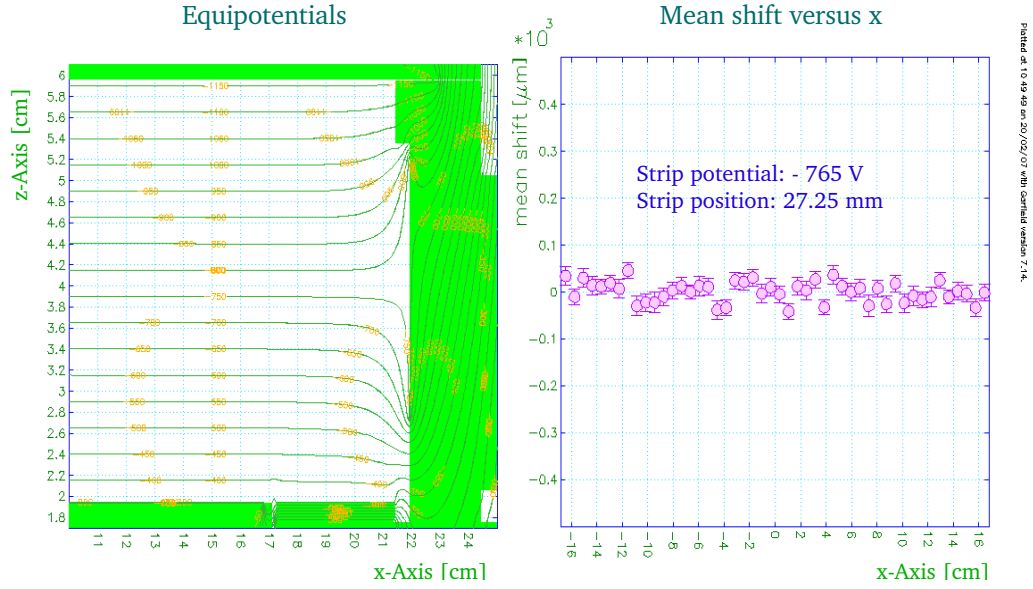


Figure 37: Equipotentials (left) and mean shift values along the pad plane (right) with a strip over the walls.

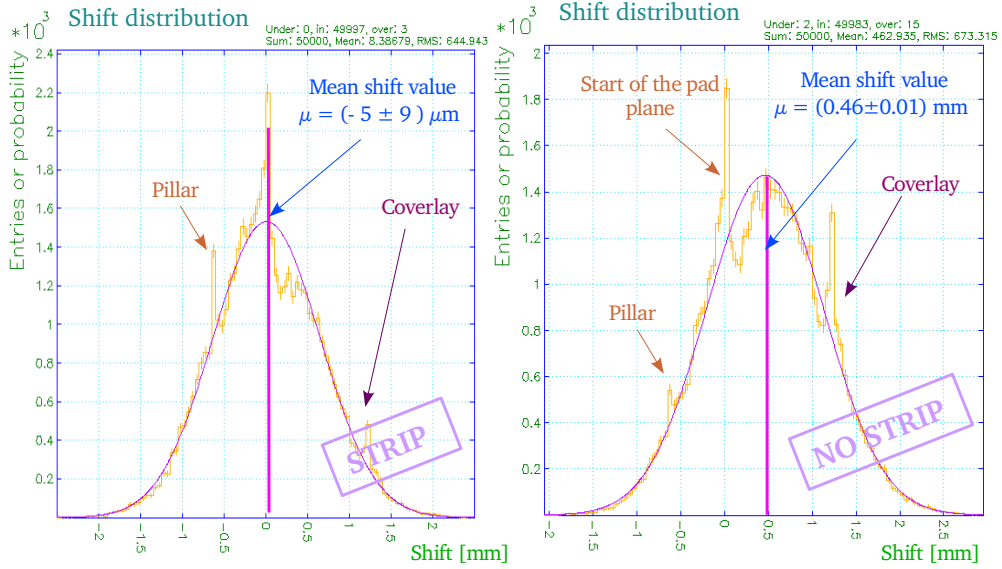


Figure 38: Shift of an electron with a strip (left) and without strip (right) near the aluminum base.



### 5.3.2 Border frame mesh (BFM) potential and pillars influence

Along the pad plane, and at the edges, the shift histograms cannot be exactly fitted by a gaussian. The distribution presents peaks along the pad plane, while at the edges the distribution is not a gaussian distribution (see figure 39).

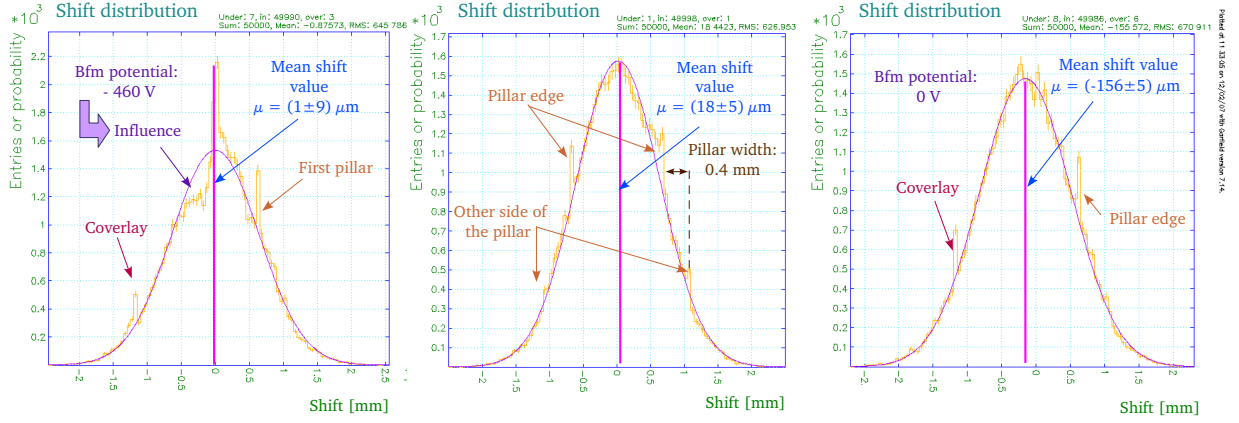


Figure 39: Histogram of 5000 electrons sent above the edge (left) and the middle (middle) of the 1<sup>st</sup> pad with a BFM potential set at -460 V. Histogram of the edge of the first pad for a BFM potential set at 0 V (right).

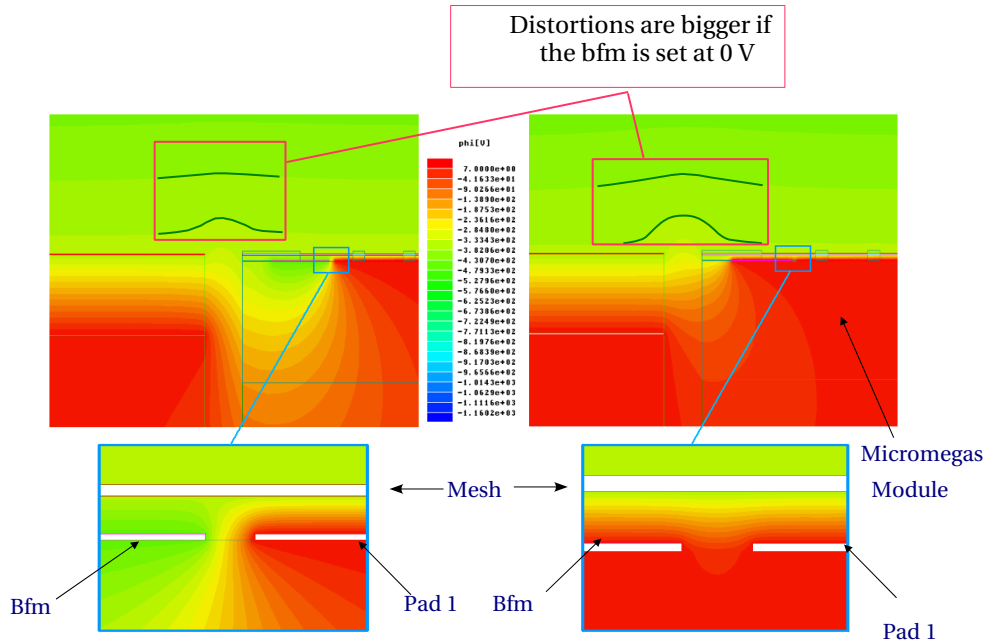


Figure 40: Equipotential for the G10 design: BFM at -460 V (left) and 0 V (right).



These peaks correspond to the beginning and the end of the pillars supporting the mesh. The center of the pad is between two pillars situated at the same distance of 0.675 mm. Each pillar is 0.4 mm wide so that the end of the pillars appears at 1.075 mm from the center corresponding thus to the small peaks of figure 39.

This observation is a consequence of the GARFIELD program used for this simulation. Actually, when an electron, after scattering in the gas, hits the side of the pillar, GARFIELD collects the hit position over the insulator. The same process can also be seen, for the edge of the pad plane, where another peak is situated at about 1.2 mm which corresponds to the coverlay.

The non-gaussian form for the edge of the pad plane is due to the BFM potential which creates a slight distortion between the readout pads and the micro-mesh, while the distribution remains gaussian when the BFM potential is set at 0 V (see figure 39).

However this slight distortion is preferable to those that appear between the cathode and the micro-mesh, when the BFM potential is set to 0 V. This can be observed by looking the mean shift values for both cases (see figure 39 and 40).

### 5.3.3 Determination of the nominal setting

In a ideal field cage, the shield potential should be set at the same value as the mesh (-360 V) and the strip potential set at the value which would be at the center of the strip (-765 V). From figure 41, the minimal mean shift is found for a shield potential set at -361 V, and a strip potential at -771 V. The difference to the setting that would be normally applied is due to the design of the field cage, including the frame of 6 mm width supporting the cathode, and the space of 5 mm between the wall and the shield.

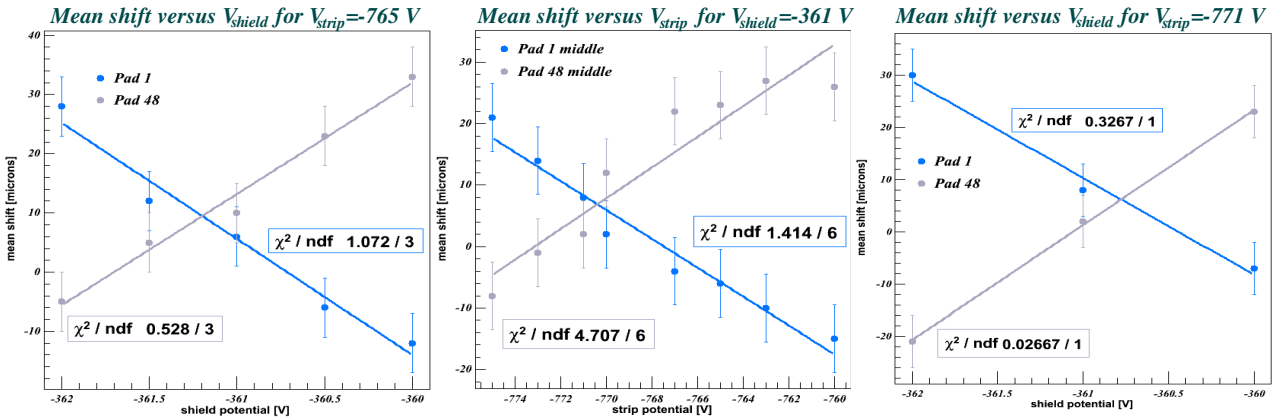


Figure 41: Mean shift value as a function of the shield potential for  $V_{\text{strip}} = -765$  V (left), as a function of the strip potential for  $V_{\text{shield}} = -361$  (middle) and as a function of the shield potential for  $V_{\text{strip}} = -771$  (right) for the first and last pad. The mean shift values are obtained with a statistic of 1000 electrons sent above the middle of each pad.

Figure 41 also shows that the variation of the potential setting has a larger effect at the shield level. In particular, for an uncertainty of 10  $\mu\text{m}$ , the accuracy needed for the shield potential should

be smaller than 1 V, while the strip potential need only 5 V. The good linearity with potential, which is observed for the first pad, is less evident for the last pad. Besides, in the case of a perfect uniform electric field, the intersection of the straight lines of both pads would be at 0 mean shift rather than 6  $\mu\text{m}$ . These asymmetries between the first and the last pad are due to the external mechanical support.

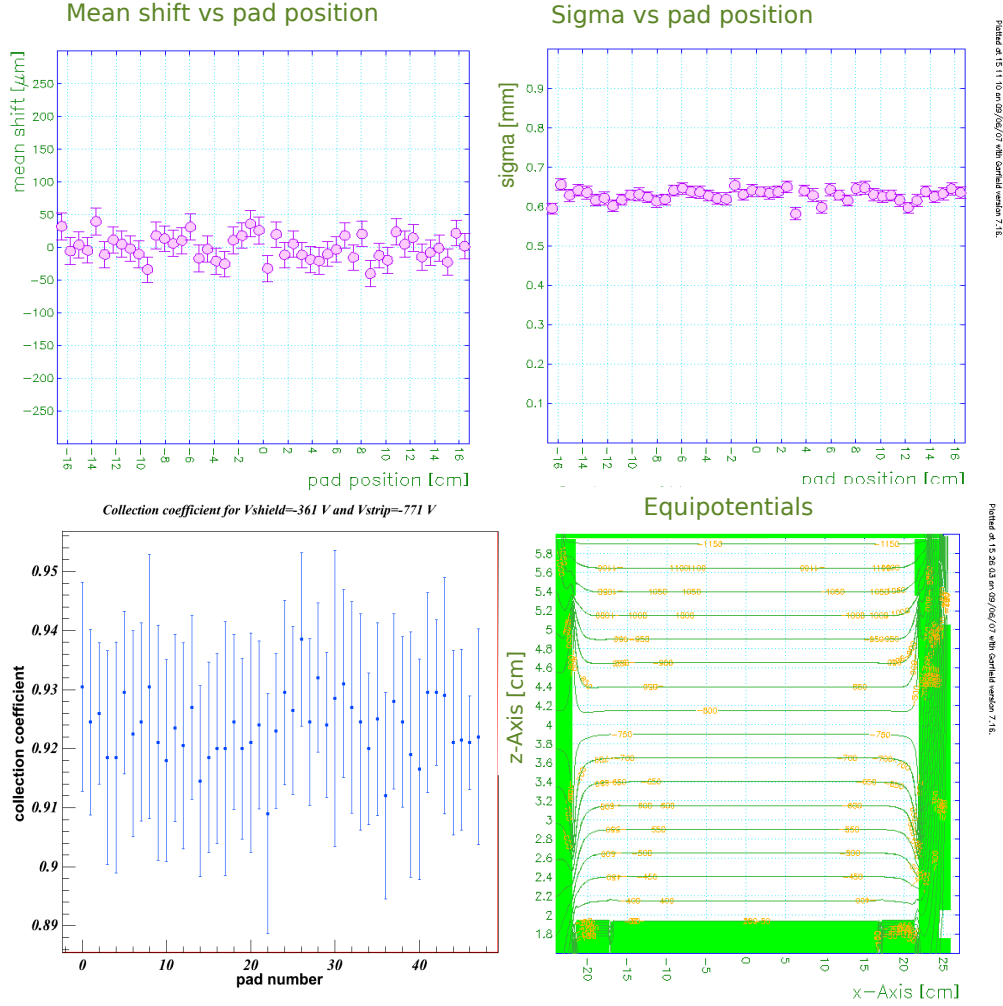


Figure 42: Mean shift (top left) and sigma value of the gaussian electron shift distribution (top right) and collection coefficient (bottom left) as a function of the pad position. Potential configuration of the field cage (bottom right). The mean shift and sigma are obtained with a statistic of 1000 electrons, while the collection coefficient values are determined from 10 illuminations of 100 electrons sent uniformly above the pad.

A change of the strip height has no influence over this asymmetry but only modifies the mean shift value. A strip displacement of 0.5 mm implies a 10  $\mu\text{m}$  shift of the mean value. On the contrary, the strip width can slightly correct the asymmetry but not completely because of the rest of the box setup constraints. The implementation of one strip decreases the initial asymmetry obtained without any strip but does not avoid it. Simulations with two and three strips show that the asymmetry decreases

with the number of strips. Three strips are already enough to totally avoid the asymmetry. However, an asymmetry between 5-10  $\mu\text{m}$ , as it is in the case of one strip, is practically too small to be taken into consideration. The uncertainties on the shield alignment or its potential precision have greater influences.

Figure 42 shows the different parameters for the nominal setting determined in this section (e.g  $V_{shield} = -361$  V and  $V_{strip} = -771$  V). The collection coefficient shows a mean value of 92.5 % which is very close to the 93 % determined theoretically for a ideal electric field.

### 5.3.4 Alignment precision

From the previous section, we already know that the electric field is very sensitive to the shield potential. But this is not the only factor that can increase distortions. The misalignment of the shield with respect to the mesh can also cause distortions. Simulations with various designs have been done to study this effect. They are indicated in figure 43.

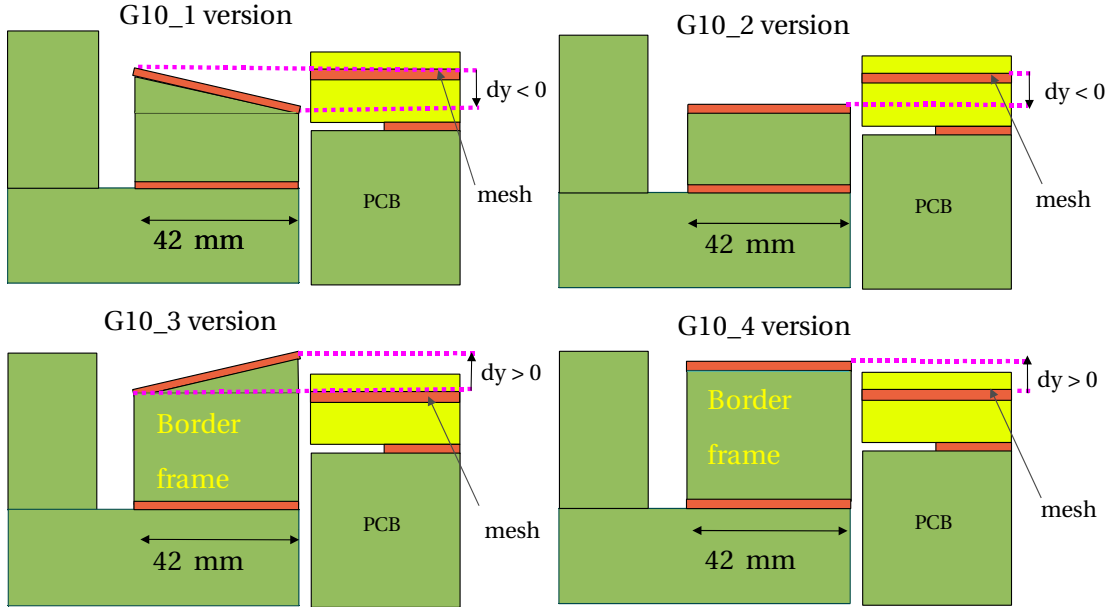


Figure 43: Different simulated G10 design showing various possible misalignment.

Figure 44 shows the collection coefficient and the mean shift of an electron as a function of the misalignment  $dy$ . 50000 electrons were used to compute the mean shift while 30 illumination of 1000 electrons were used to compute the collection coefficient. In figure 44, the linear fit seems to be, at first order, a good estimation of the evolution of both parameters with respect to the misalignment  $dy$ . The consequence of a misalignment like the G10-2 and G10-4 version appears to have more influence than the others.

In addition, it shows that an error of 0.2 mm in the alignment implies a shift of 80  $\mu\text{m}$  of the mean shift and 5% variation of the collection coefficient. Depending on the sign of the misalignment  $dy$ , the field lines can be curved towards the pad plane. As a consequence, more electrons are collected in the first pad in these configurations as demonstrated by a greater collection coefficient.

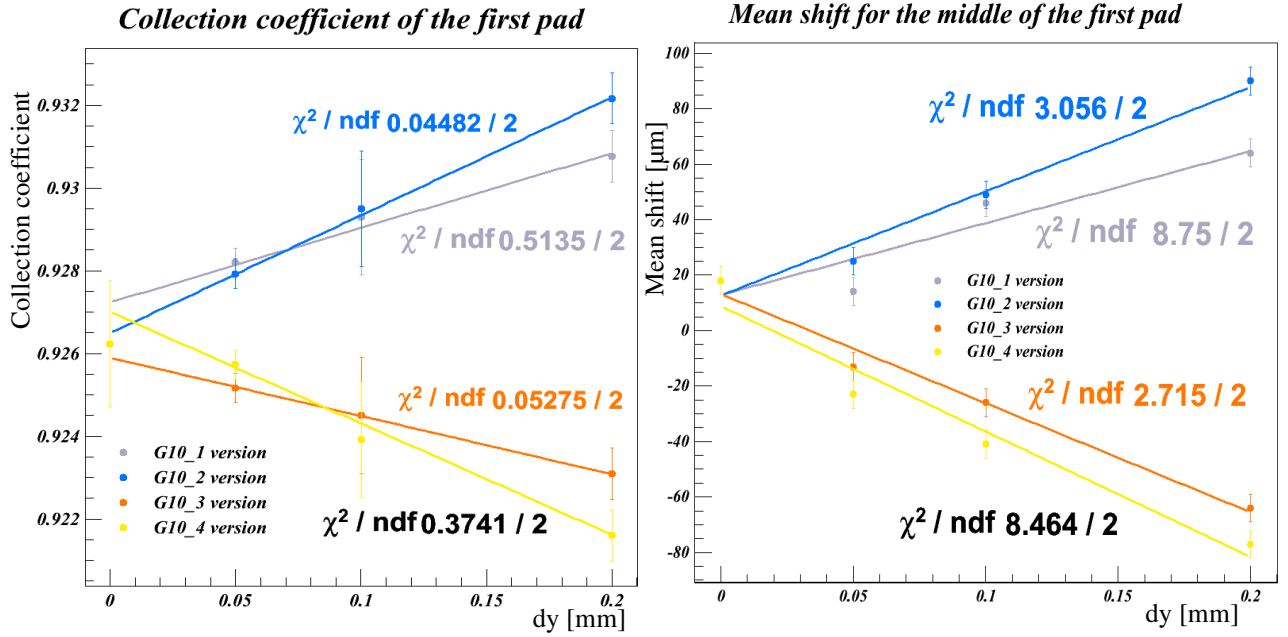


Figure 44: Collection coefficient for the first pad (left) and mean shift value of an electron sent above the middle of the first pad as a function of the  $dy$  parameter.

The field cage is designed with  $\pm 0.2$  mm tolerance, so that a mean shift of  $80 \mu\text{m}$  is expected with the nominal setting. Concerning the TPC, the precision required is  $\pm 0.1$  mm, which corresponds to a mean shift around  $40 \mu\text{m}$ . In the case of a constant misalignment observed in the whole shield, the distortions can be attenuated by raising or reducing the shield potential above or below the nominal setting of  $-361$  V but also by changing the strip potential.

#### 5.4 Electrostatic simulations for the GEM test bench

The simulations of the GEM test bench give some keys for the preliminary analysis of the results of the test bench measurement done in February 2007. The results are presented in the next section. In the following simulation, the GEM voltages are set such as to get transfer fields of  $2000 \text{ V/cm}$  and an induction field of  $2000 \text{ V/cm}$ . The cathode and the guard ring voltages are set to get a drift field of  $140 \text{ V/cm}$ . This setting corresponds to the nominal setting of the module during data acquisition on the GEM test with the  $\text{ArCO}_2$  (90:10) gas mixture. No amplification simulation has been done so far but it might be done in the future.

Figure 45 shows great distortions due to the presence of the guard ring. The equipotentials start to be straight at a distance larger than two centimeters from the guard ring. Such a distance corresponds to more than one pad and can already explain the non collection of charges at the edges of the pad plane in the HARP TPC measurement<sup>13</sup>. As expected, the side where the guard ring is  $5 \text{ cm}$  wide is more affected than the other.

<sup>13</sup>This measurements were done in March 2006, at CERN with the similar configuration

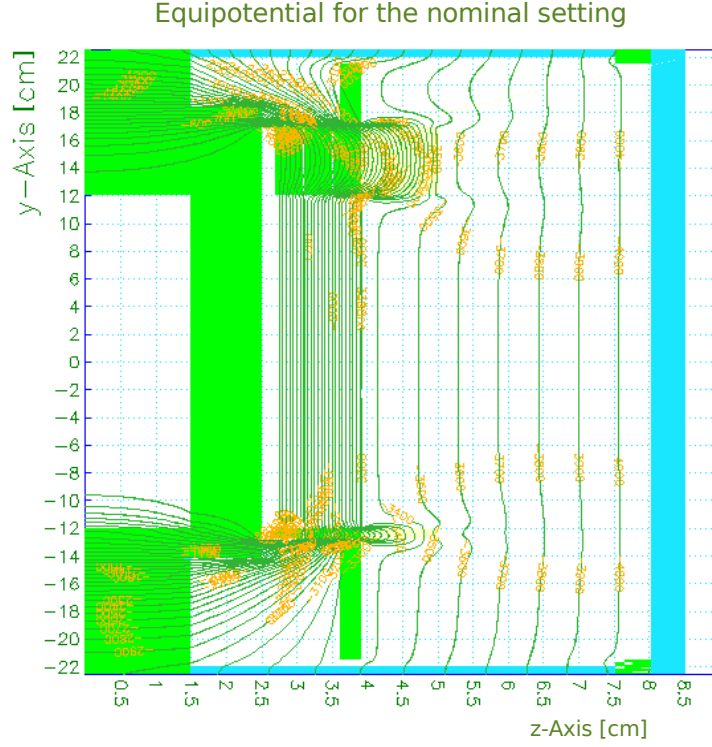


Figure 45: Equipotentials of the GEM box for the nominal setting.

#### 5.4.1 Guard ring influence

For the particular study of the guard ring potential influence, the setting is described in Table 4.

$IF$ [V/cm]	$TF1$ [V/cm]	$TF2$ [V/cm]	$V_q$ [V]	$DF$ [V/cm]	$V_{NS}$ [V]
2005	2010	2020	-315	180	-3557

Table 4: Nominal setting.  $V_q$  is the potential difference between the top and the bottom of the GEMs,  $DF$  the drift field and  $V_{NS}$  is the nominal setting value of the guard ring potential.

Table 5 indicates the four voltage settings used for the simulation.

$V_{GR}$ [V]	$DV$ [V]
-3497	-60
-3557	0
-3617	60
-3677	120

Table 5: Voltage setting of the guard ring for the four simulations. The other settings remain as in Table 4.

Figure 10 consists of four subplots arranged in a 2x2 grid, showing drift lines for different values of  $DV$ . The top row shows results for  $DV=0$  V, and the bottom row shows results for  $DV=120$  V. The left column plots  $y_{TAxis}$  [cm] (ranging from -9.5 to -15.5) against  $z-Axis$  [cm] (ranging from 3.8 to 5.8). The right column plots  $y-Axis$  [cm] (ranging from 8 to 18) against  $z-Axis$  [cm] (ranging from 3.8 to 5.8). The plots show drift lines (orange) and shaded regions (yellow and green) representing different physical regions or boundaries.

Figure 46 shows that no charge reaches the border pads. Hence, the collection coefficient is zero at the edge and increases up to a average value of 95%. This corresponds to the collection coefficient obtained in a perfect uniform electric field of 96% (see 47). It follows that despite the distortions that are observed near the guard ring, good measurement can be done in the center of the sector (without

Figure 46 shows that no charge reaches the border pads. Hence, the collection coefficient is zero at the edge and increases up to a average value of 95%. This corresponds to the collection coefficient obtained in a perfect uniform electric field of 96% (see 47). It follows that despite the distortions that are observed near the guard ring, good measurement can be done in the center of the sector (without

any distortion).

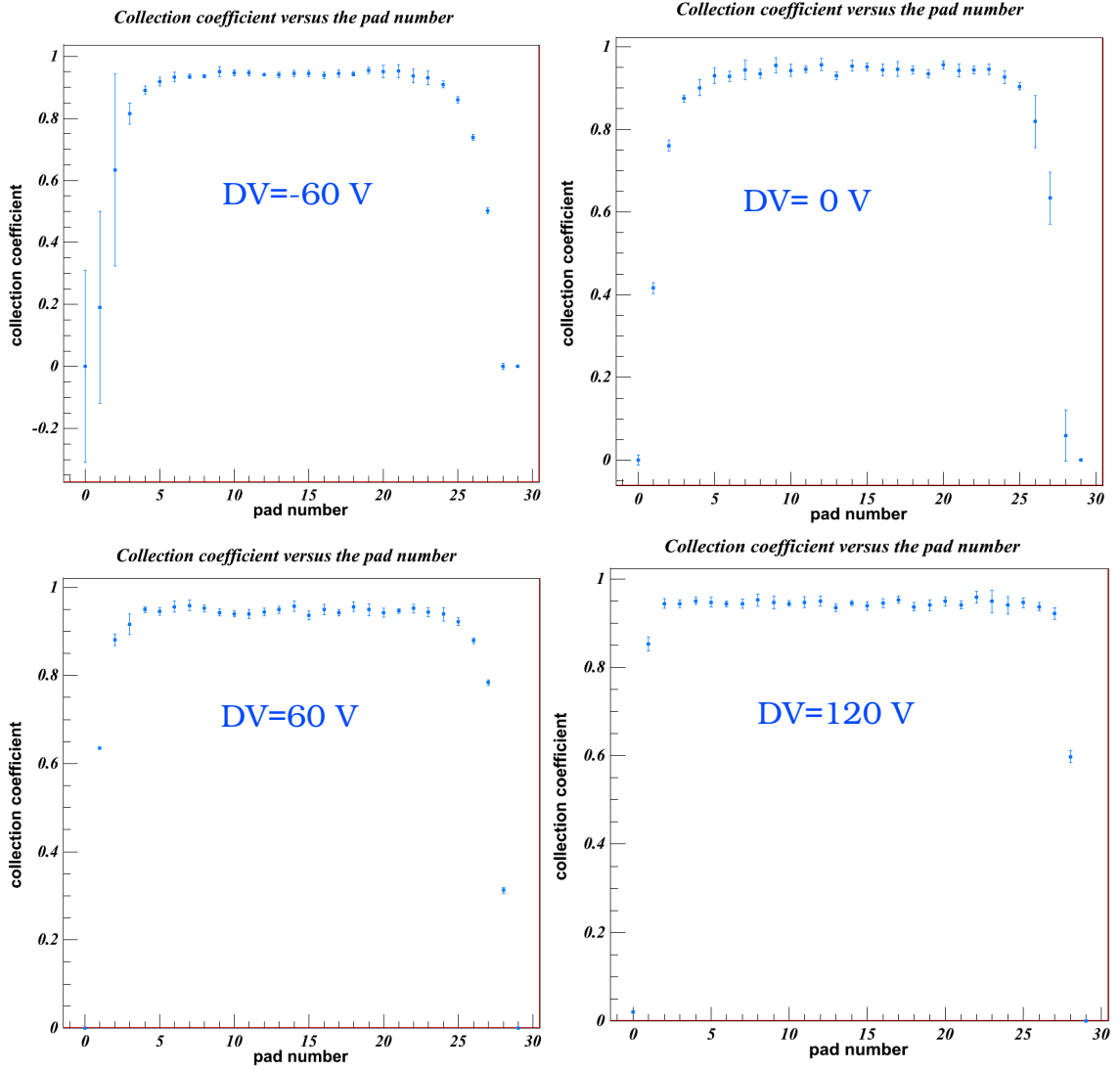


Figure 47: Collection coefficient as a function of the pad position for  $DV = -60$  V (top left),  $DV = 0$  V (top right),  $DV = 60$  V (bottom left) and  $DV = 120$  V (bottom right).

Figure 48 shows the mean shift obtained for various value  $V_{GR}$ .

The uniformity can be improved by changing the guard ring potential. The mean shift, as well as the collection coefficient, become zero after 5 pads for  $DV = -60$  V. They fall to 0 V, after 4 pads for  $DV = 60$  V and after 3 pads for  $DV = 120$  V. For  $DV = 120$  V, near the guard ring long side, an opposite distortion due to a very small guard ring voltage ( $-3677$  V) starts to bend the drift lines more toward the pad plane. as it can be seen for third pad with a mean shift greater than zero and a collection coefficient already at 0.95 while, at the other side, it is still below.

The mean shift distribution of the first and last point indicate the same value for the first three

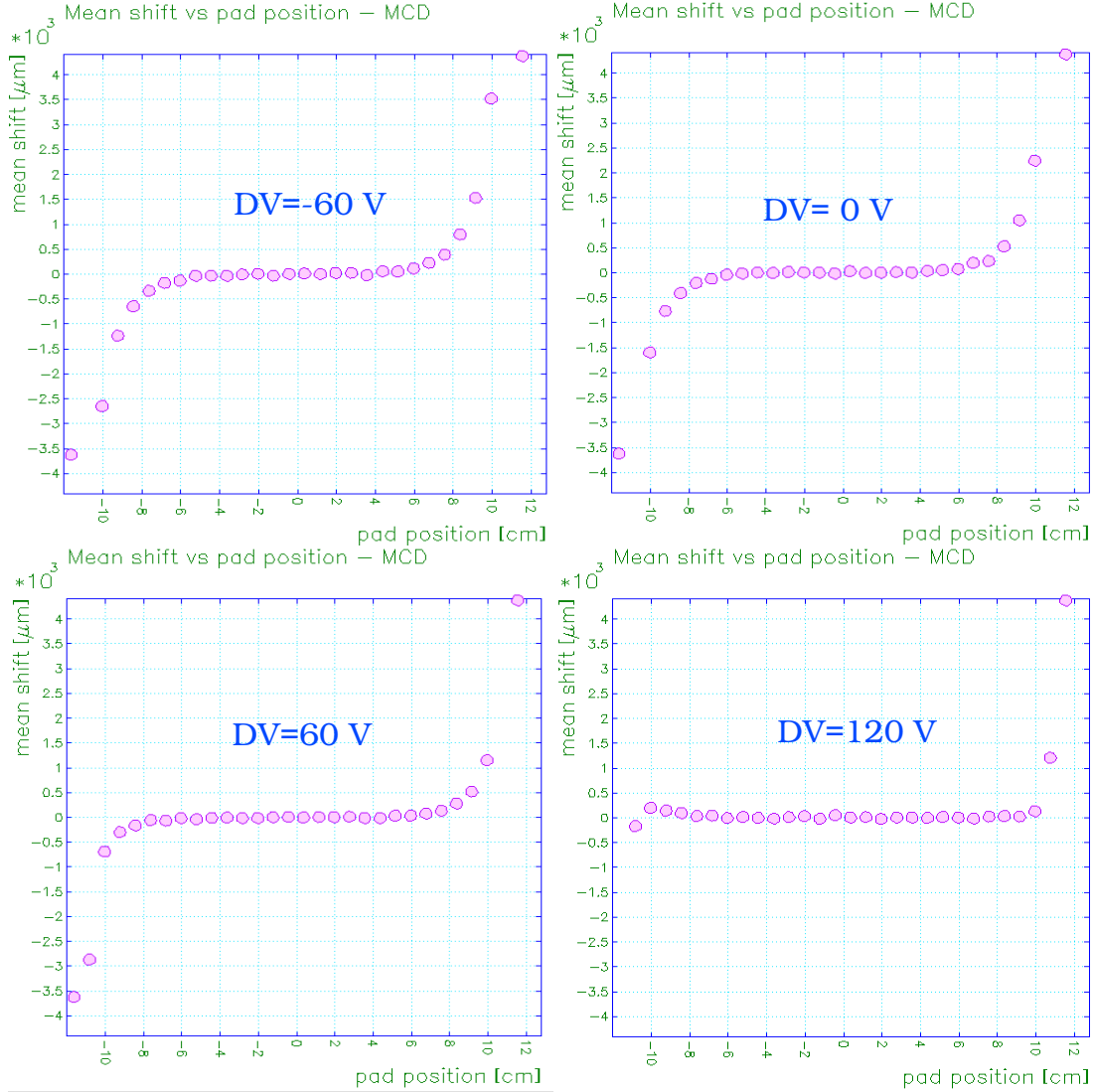


Figure 48: Mean shift value as a function of the pad position for  $DV=-60$  V (top left),  $DV=0$  V (top right),  $DV=60$  V (bottom left) and  $DV=120$  V (bottom right).

voltages. This behaviour comes from the GARFIELD program itself the same reason than the peaks observed over the shift distribution in the case of the Micromegas (see section 5.3.2). Actually, the arrival position of the electrons released over the middle of the first and last pad is taken by the garfield program as the guard ring edges since the program does not take into account the motion of the electrons through the guard ring. Hence, the mean shift of the edge pads is only given by the half of the pad width<sup>14</sup>. For the same reason, the uncertainties on the collection coefficient are not

<sup>14</sup>Note: the simulation of figure 48 is done with electrons released not over the middle of the pad but a little bit shifted with a value of  $375 \mu\text{m}$  toward the guard ring short size. Therefore the value near the guard ring short size is  $-3.625 \text{ mm}$  and  $4.375 \text{ mm}$  near the guard ring long size



properly calculated near the guard ring as well as the RMS value (see 49). For a perfect uniform electric field, as seen in the previous section that the RMS of the shift distribution is about  $440 \mu\text{m}$ . In figure 49, the RMS indicates a value between 450 and  $500 \mu\text{m}$  which is in good agreement with the theoretical value.

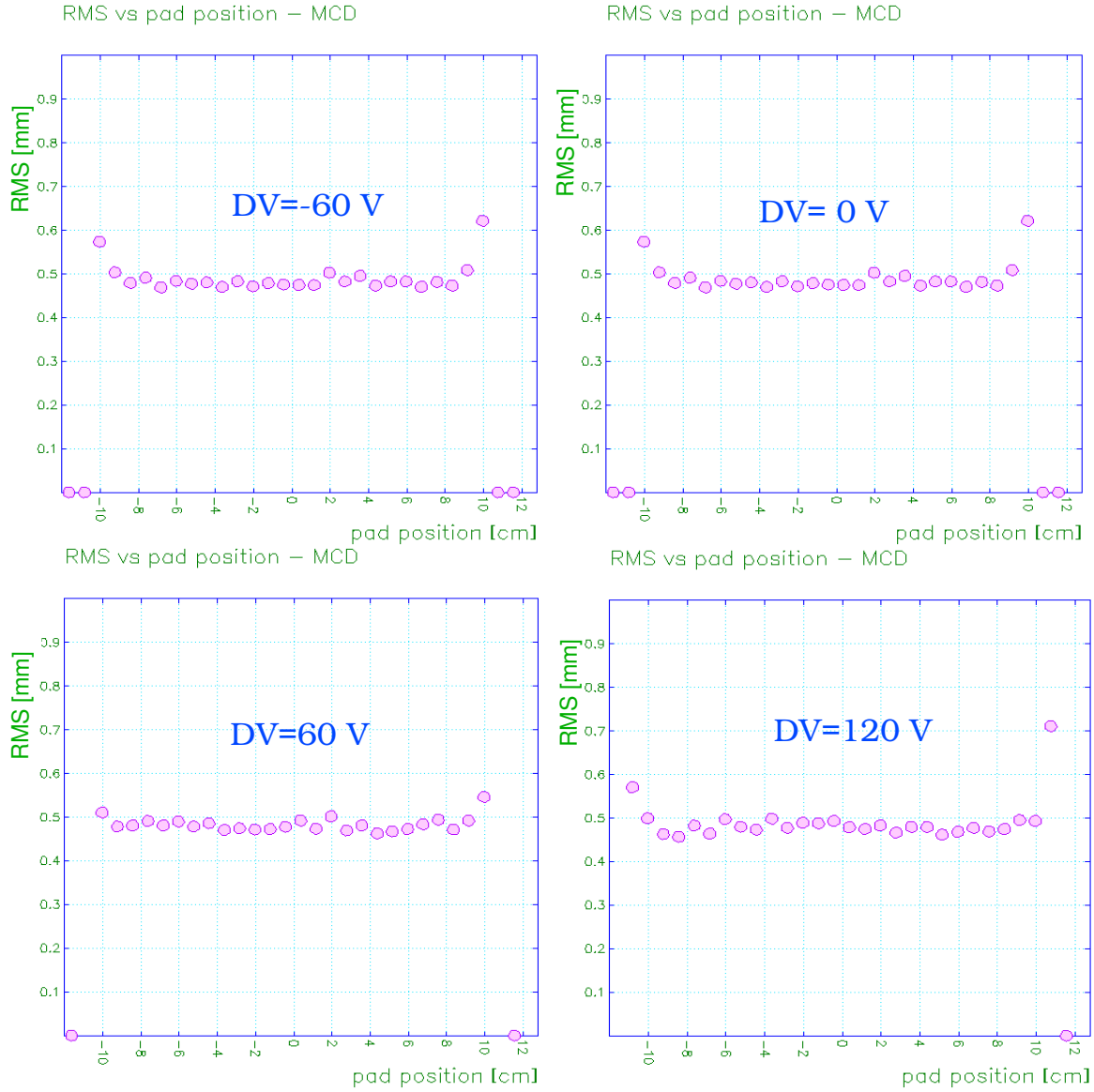


Figure 49: RMS of the electron shift distribution as a function of the pad position for  $DV=-60 \text{ V}$  (top left),  $DV=0 \text{ V}$  (top right),  $DV=60 \text{ V}$  (bottom left) and  $DV=120 \text{ V}$  (bottom right).

## 6 GEM measurement results

### 6.1 Scope

The characterization of the readout modules is done by the study of the following parameters:

- **SOURCE SPECTRUM RECONSTRUCTION:** To calibrate the modules, the source spectrum is reconstructed to observe any broadening or displacement of the photo-peaks.
- **GAIN and ENERGY RESOLUTION:** The gain can vary by up to 20 % on a pad-per-pad basis. Therefore, a calibration of the electronics is needed to be able to interpret future measurements. The gain is given by:

$$G = \frac{\text{charge [ADCcounts]} \times C}{N},$$

where  $C$  is the electrons/ADC conversion factor and  $N$  is the mean number of ionization, calculated using the energy of the photons and the energy necessary for a creation of an ion-electron pair in the gas. In the following, the ADC value of the iron source peak at 5.9 keV will be called gain, as first approximation, and the ratio between the mean and sigma value of the photo-peak will give the energy resolution of the pads.

- **LOCAL CHARGE COLLECTION:** Precisely measure the charge collection on the border of the active area of the GEMs, especially in the intermediate region between the two sectors of the pad plane. More generally, this point focuses on a border effects study.
- **PAD RESPONSE FUNCTION and CROSS-TALK:** Reconstruction of the centroid position as function of the source displacement, and observation of the induced signals on neighboring pads when moving the source from the center to the border of a given pad.

### 6.2 Spectrum Reconstruction

#### 6.2.1 Spectrum Reconstruction algorithm

The spectrum reconstruction is made via functions shared in three classes. The methods of the first class are able to read the files where are set all the relations between the pad plane, the channels and the boards and make the link to the row and pad number. The second class is the storage class where storage vectors are defined. The third class is the class where the clustering is defined.

- **Initialization:**

For each hit, the row, the pad, the ADC charge and the time arrival are determined and stored in a vector which will be used by the cluster algorithm.

- **Data purification:** Before running the cluster algorithm, it is useful to purge the data in order to have only the information needed. Hence, only the value above the pedestal is taken into account.
- **Cluster algorithm:**
  1. The ADC charge and the other properties of one pad are ordered in time.
  2. If a time sample is the same for contiguous pad, then the information of these pads are joined together in a vector. The faster way to check that the time sample of the contiguous pad overlaps is using the minimal and maximal time of the sample.

3. Taking into account the possibility to have more than one time group per pad, the sum of each time sample per hit and per pad gives the reconstructed adc value for a determinate cluster.
- The spectrum of the iron source is then simply obtained by filling an histogram with the adc charge of each cluster.

### 6.2.2 Spectrum fit

To quantify the gain and resolution of each pad, a fit is done over the peak of the reconstructed iron spectrum.

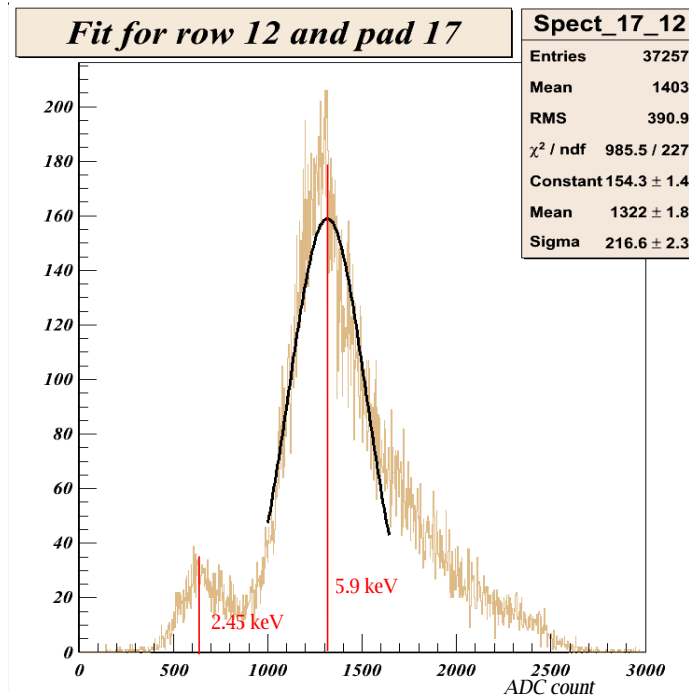


Figure 50: Spectrum of the iron source with a gaussian fit for the peak at 5.9 keV. The escape peak is also visible. The mean value of the gaussian fit is  $1322 \pm 2$  and the sigma  $217 \pm 2$  for a  $\chi^2/\text{ndf}$  of 985.5/227.

The final fit is made via three intermediate fits. The range of the first fit is define around the bin with the highest content. From this fit,  $\mu_0$  and  $\sigma_0$  are obtained. The range of the second fit is set as  $[\mu_0 - 1.5\sigma_0, \mu_0 + 2\sigma_0]$ . This procedure is repeated and finally gives the parameters  $\mu_2$  and  $\sigma_2$ .

Figure 50 shows the result obtain after 24h of measurement. As we can see in figure 50, the gaussian approximation is not a good fit. Normally the spectrum shape should stop faster and the peak should more correspond to the gaussian fit. This observed behaviour is, by now, explained with the presence of a huge attachment inside the chamber. In fact, a Monte Carlo simulation of charge attenuation has been done. The distribution obtained showed that an electron attachment can give a shape to the iron spectrum. This assumption is actually not totally proved and therefore further studies using  $\text{iC}_4\text{H}_{10}$  instead of  $\text{CO}_2$  are planed.

However, the fit of the photo-peak can give an estimation for the sigma, which is necessary to determine the resolution obtained by taking the ratio  $R = \frac{\sigma_2}{\mu_2}$ . In the following, the mean value,  $\mu_2$ , determined by the fit will be called gain.

It can be also interesting to compare the number of conversion observed during the measurement and the one calculated theoretically. For the measurement over 24 hours, 98363 events have been observed for 120000 triggers. The number of observed conversion is then :

$$\frac{98364 \text{ conversion}}{120000 \cdot \text{triggers}} \cdot 1.4 \frac{\text{triggers}}{s} = 1.2 \frac{\text{conversion}}{s},$$

for an expected number of conversions of 1.45 theoretically. The number of conversions is then well described theoretically.

## 6.3 Stability

### 6.3.1 Time Stability

The gain and energy resolution stability have been checked over one day for a pad at the center of the second sector. The variation of the gain is about 2% while it is 8% for the resolution. These values can be improved by a check over time of the temperature, the pressure and the voltage applied. The gaussian fit, shown in figures ?? and 52, is better for the mean value than for the resolution. Both case show however a good stability around a mean value of 1240 ADC count for the gain and around a mean value of 20 % for the resolution.

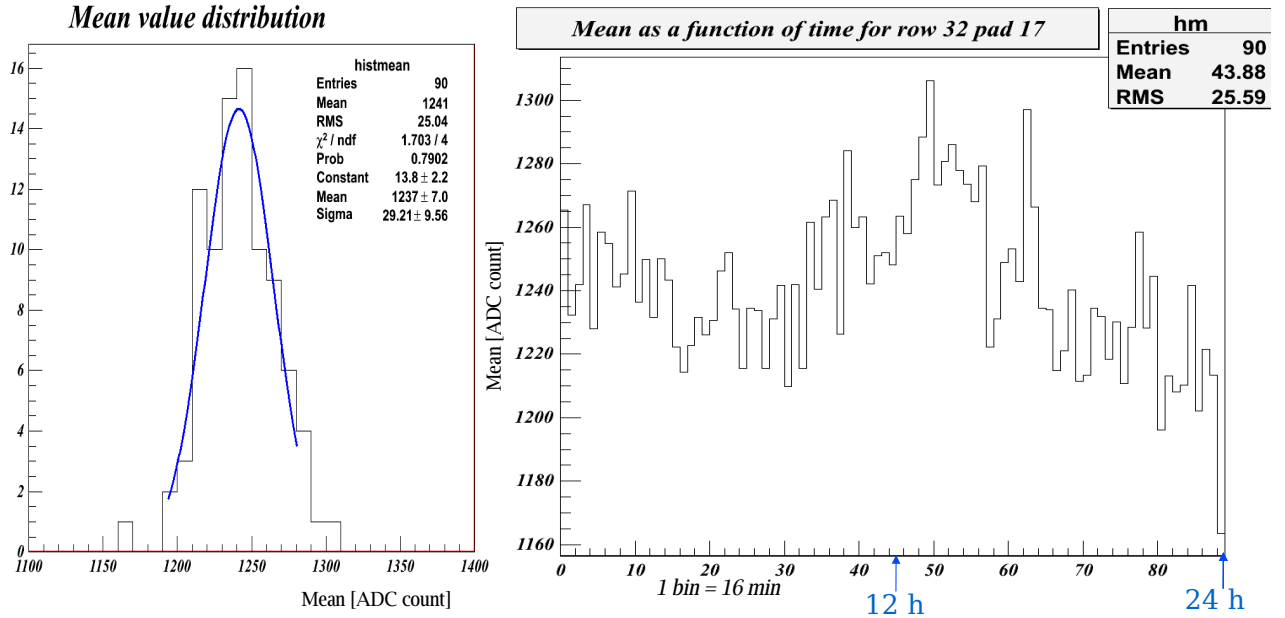


Figure 51: Distribution of the mean value over one day (left). Mean value of the iron source peak as a function of time (1 bin = 16 min).

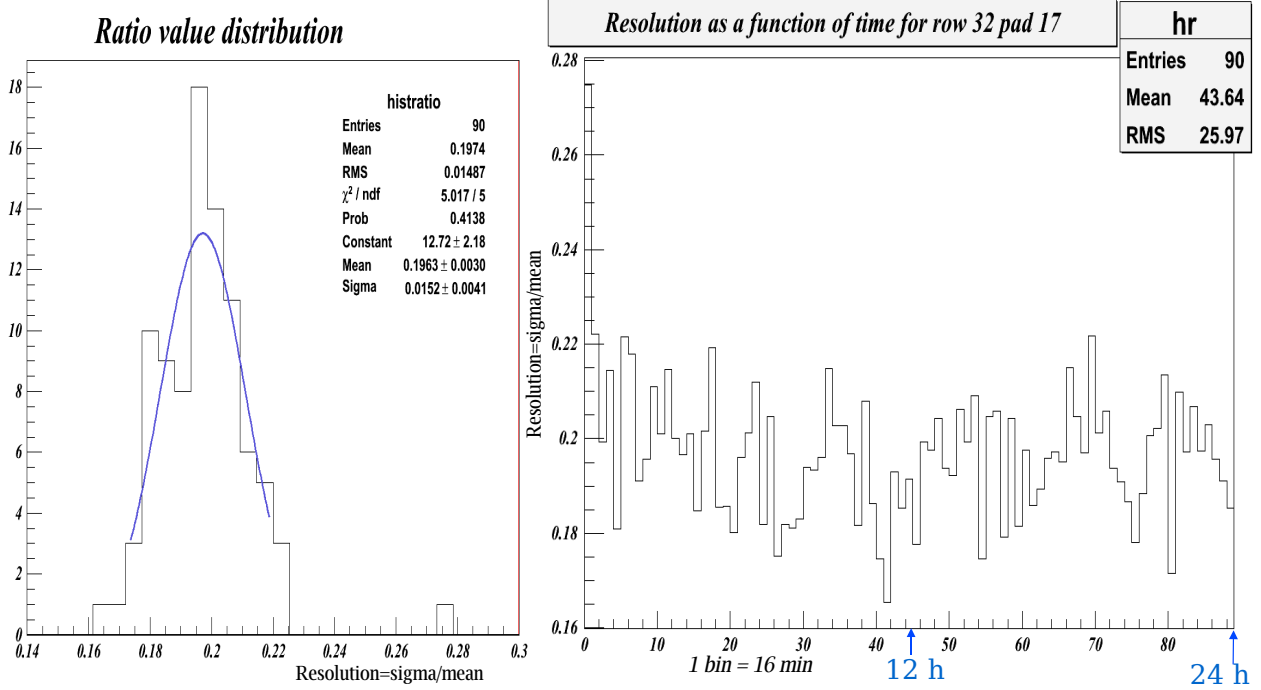


Figure 52: Distribution of the resolution over one day (left). Resolution of the iron source peak as a function of time (1 bin = 16 min).

### 6.3.2 Pad plane uniformity

This measurement manifests the capabilities of the test bench to establish precise gain map. A scan with 300 triggers taken over each pad of 10 successive rows has been taken.

The measurement starts from the second row (row=1) of the first sector since no charge is observed over the first row. In spite of the low statistics, gain and resolution are quite uniform in the 10 rows except at the edge of the pad plane, where edge effects are observed. A 10% gain variation is observed. This variation is greater than the measurement precision which is about 3% (see figure 55). The improvement of the acquisition rate to 7 Hz will provide a complete and precise scan of a Micromegas module in 1-2 days. In fact, for the same statistic, 14 hours are needed to characterize the 1728 pads of a Micromegas module.

The edge effects are due to the presence of the guard ring which creates distortions at the border pads as seen in the simulation of the potential configuration (see figure 45).

Because of the distortions at the edges and the few collected charges in this region, the photo-peak of the iron source is not well defined. Hence, the mean and sigma values obtained from the fits are not properly computed; the pads with a resolution greater than 1 are not represented.

The accumulated charge per column (see figure 55) describes reasonably well the distortions. The influence of the guard ring long side and short side is also shown by observing an asymmetry in the

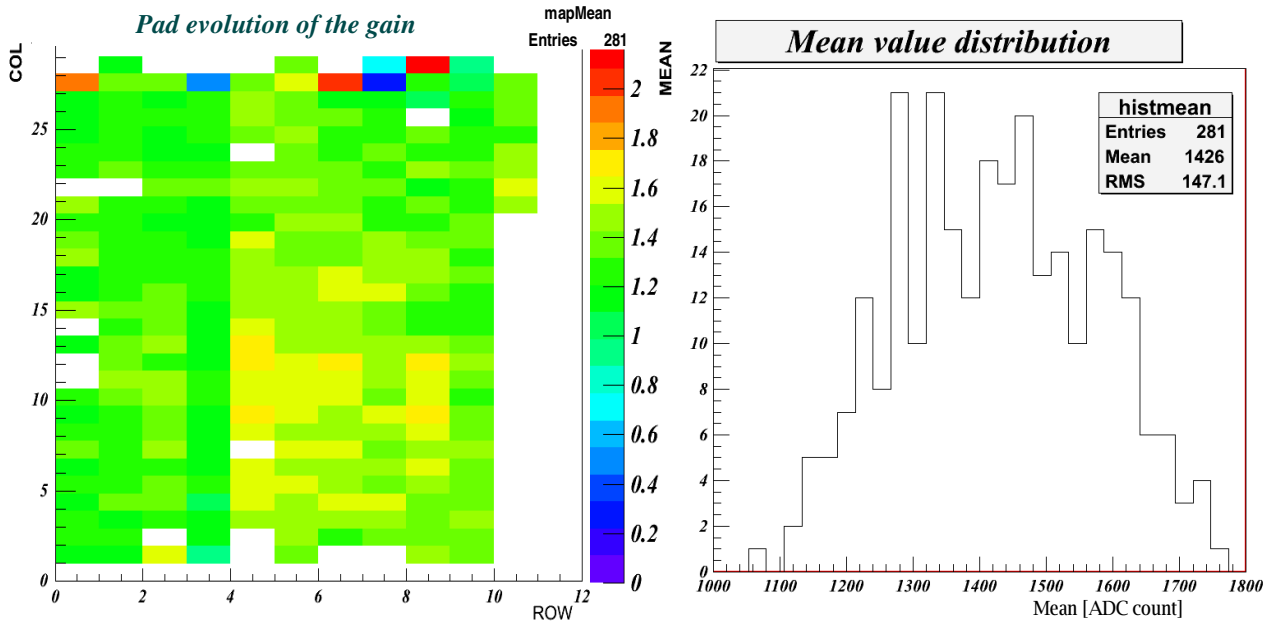


Figure 53: Mean value per pad for 10 successive rows (left). The pads without value in the center are faulty pads. Mean distribution for the good pads (right).

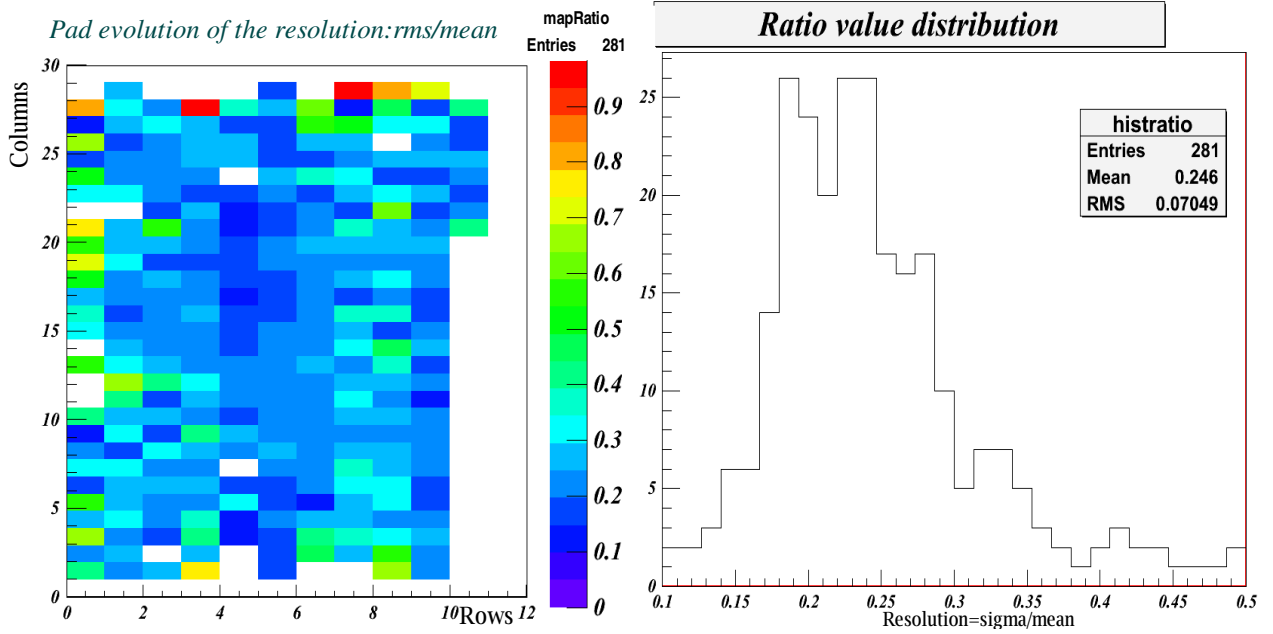


Figure 54: Resolution value per pad for 10 rows (left). The pads without value in the center are faulty pads. Resolution distribution for the good pads (right).

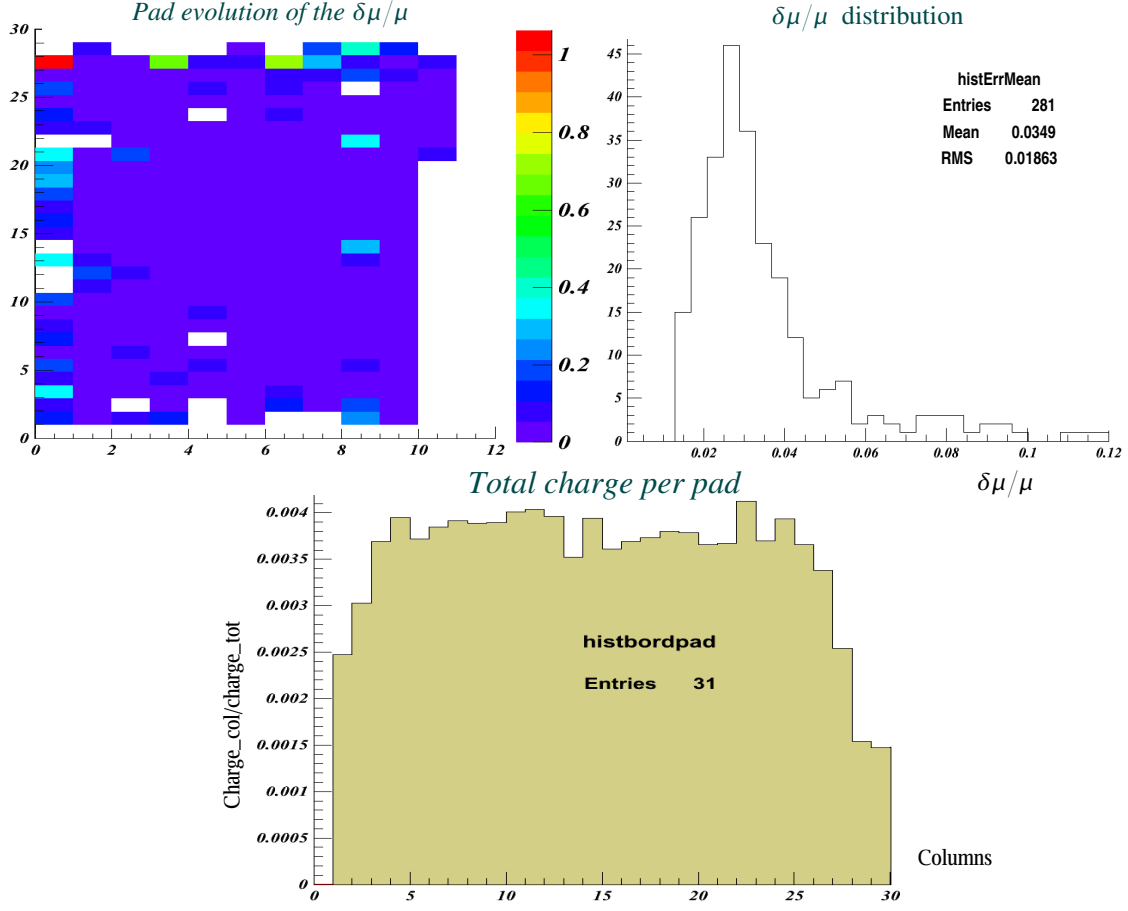


Figure 55: Charge distribution per column normalized with the total charge collected over 10 rows (bottom right).

collected charge of both sides of the pad plane. In particular, figure 55 shows that less charge is collected near the guard ring long side, where the column number is 30.

#### 6.4 Difference between the sectors

In order to compare the gain and the resolution between the two sectors the setting described in Table 6 has been set.

$V_{cathode}$ [V]	$V_{GR}$ [V]	$DF$ [V/cm]	$V_q$ [V]	$TF2$ [V/cm]	$TF1$ [V/cm]	$IF$ [V/cm]
-3905	-3499	140	315	2000	2000	2000

Table 6: Voltage setting, where  $V_q$  is the potential difference between the top and the bottom of a GEM (see figure 22).

The gain observed on the GEMs is slightly different according to the sector analysed. It seems also that the first sector has a greater gain than the second sector (see (56) and table 7). This result

was also observed when the GEMs were placed over the HARP TPC at CERN.

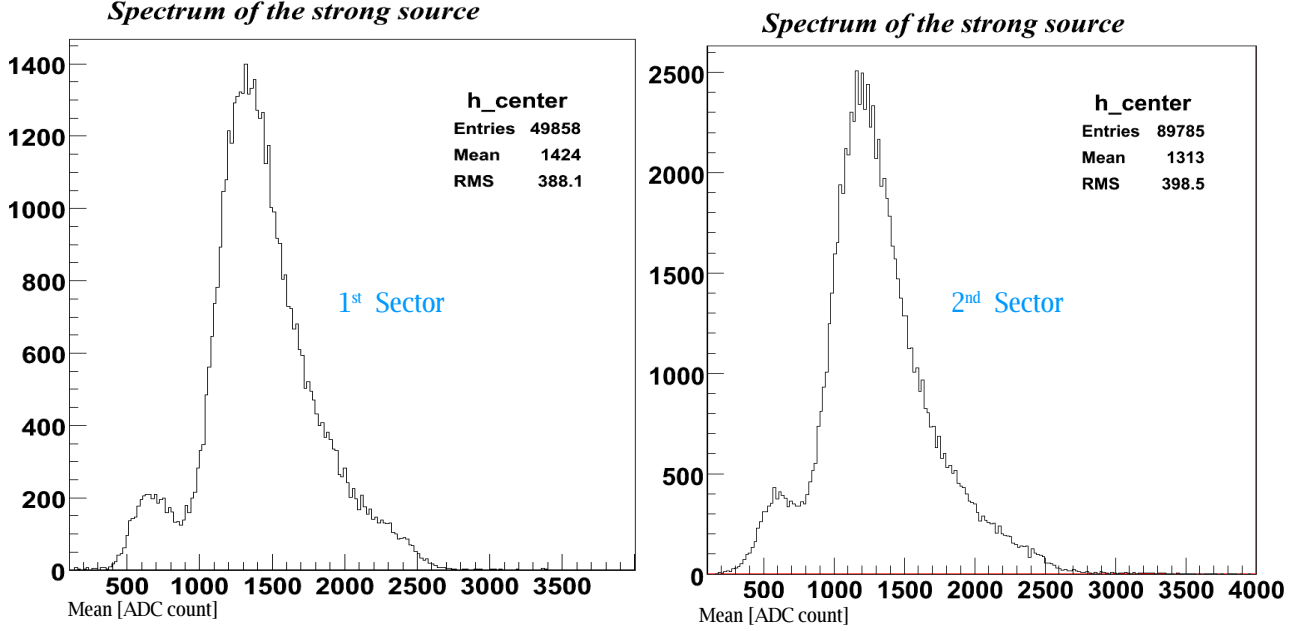


Figure 56: Spectrum obtained for a pad in the center of the first sector (left) and second sector(right).

Sector	Gain	Resolution
1 <sup>st</sup> sector	$1361 \pm 2$	$20.5 \pm 0.2\%$
2 <sup>nd</sup> sector	$1263 \pm 1$	$22.0 \pm 0.1 \%$

Table 7: Gain and resolution value obtained for both sectors

#### 6.4.1 Variation of the GEM potential

In figure 57, three reconstructed spectrum are presented depending on the potential difference of each GEM.

	$V_{cathode}$ [V]	$V_{GR}$ [V]	$DF$ [V/cm]	$V_q$ [V]	$TF2$ [V/cm]	$TF1$ [V/cm]	$IF$ [V/cm]
a)	-3890	-3484	140	310	2000	2000	2000
b)	-3905	-3499	140	315	2000	2000	2000
a)	-3920	-3514	140	320	2000	2000	2000

Table 8: Voltage setting, where  $V_q$  is the potential difference between the top and the bottom of a GEM (see figure 22).



Figure 57 shows the iron spectrum used to compute the results shown in figure 57.

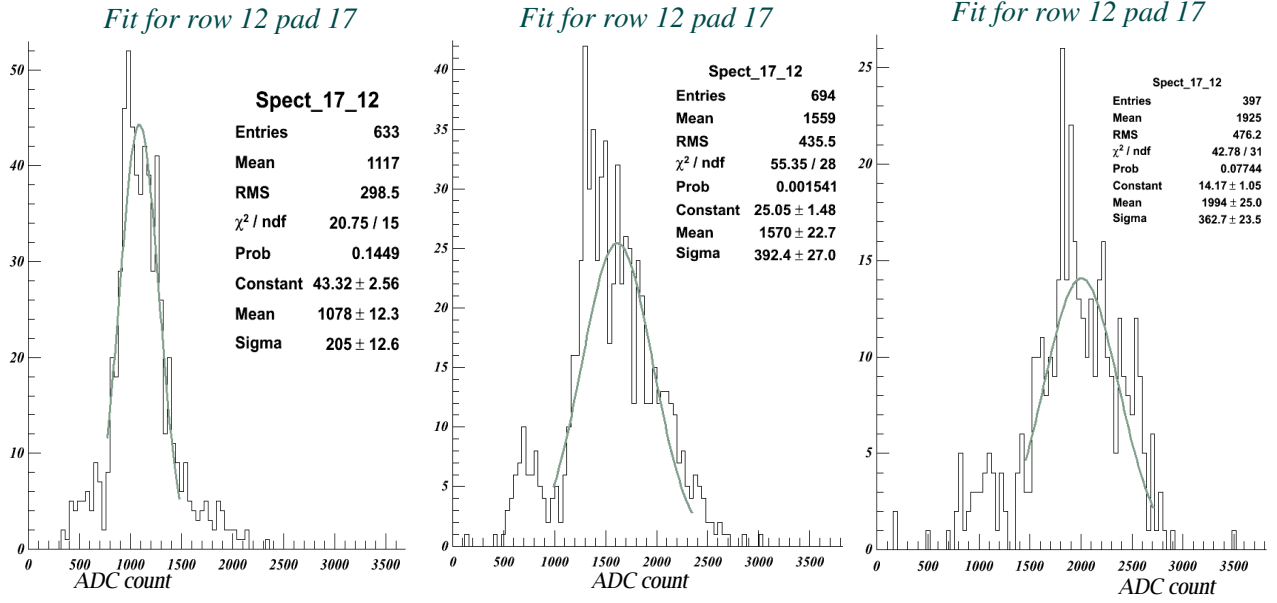


Figure 57: Spectrum obtained over the pad (12,17) for  $V_q = 310$  V (left), 315 V (middle) and 320 V (right)

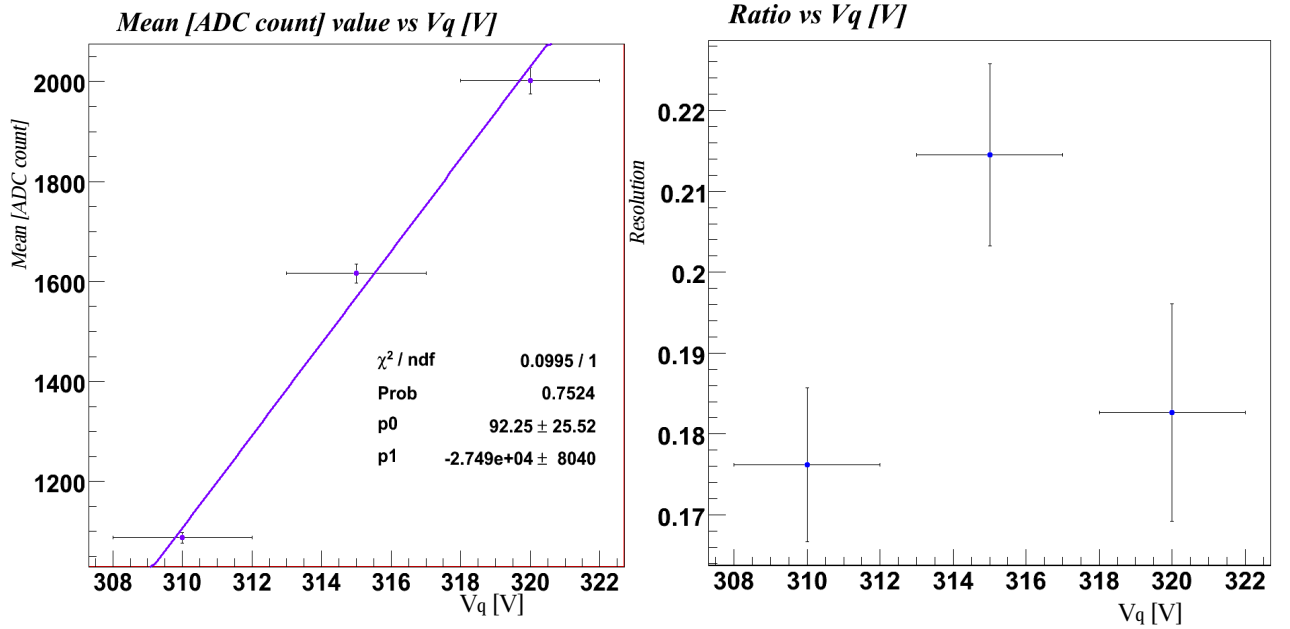


Figure 58: Mean value (left) and resolution (right) as a function of  $V_q$ .

From these figures, one see that an increase of the amplification field induces a linear increase of the gain, whereas the resolution remains approximately constant. Normally the proportional mode of the GEM would imply an exponential dependence of the gain with the voltage applied. However since the variation of potential is small (about 5 V), the result obtained corresponds totally to an exponential distribution at first order (i.e a linear distribution).

#### 6.4.2 Transfer and induction field variation

The variation of the amplification field is described in table 9. For each setting, one spectrum has been done for a pad situated in the middle of the first sector. An example of one of these spectrum is shown in figure 59, while the result obtained for the mean, sigma and their ratio are shown in figure 60.

$IF$ [V/cm]	$TF1$ [V/cm]	$TF2$ [V/cm]	$dV$ [V/cm]
-2000	-1600	-1200	-800
-2000	-1800	-1500	-500
-2000	-2000	-2000	0
-1500	-1800	-2000	500

Table 9: Potential setting:  $IF$  stands for the induction field,  $TF1$  for transfer field between the first and the second GEM and  $TF2$  for the transfer field between the second and the third GEM and finally  $dV$  is defined as the difference  $dV = IF - TF2$

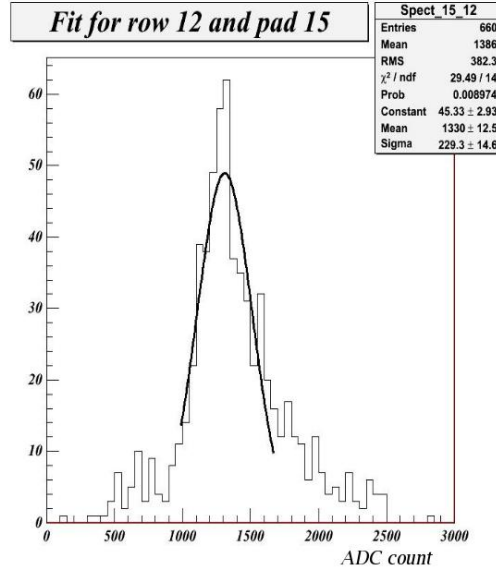


Figure 59: Reconstructed spectrum for the first setting ( $dV=-800$  V). The mean value is  $1330 \pm 13$  and the sigma  $229 \pm 15$  for a  $\chi^2/ndf = 29.49/14$ .

In figure 60, the mean and sigma values are given for 660 entries in the spectrum histogram. Systematic effects seem to be avoided by studying the ratio instead of the mean or the sigma value,

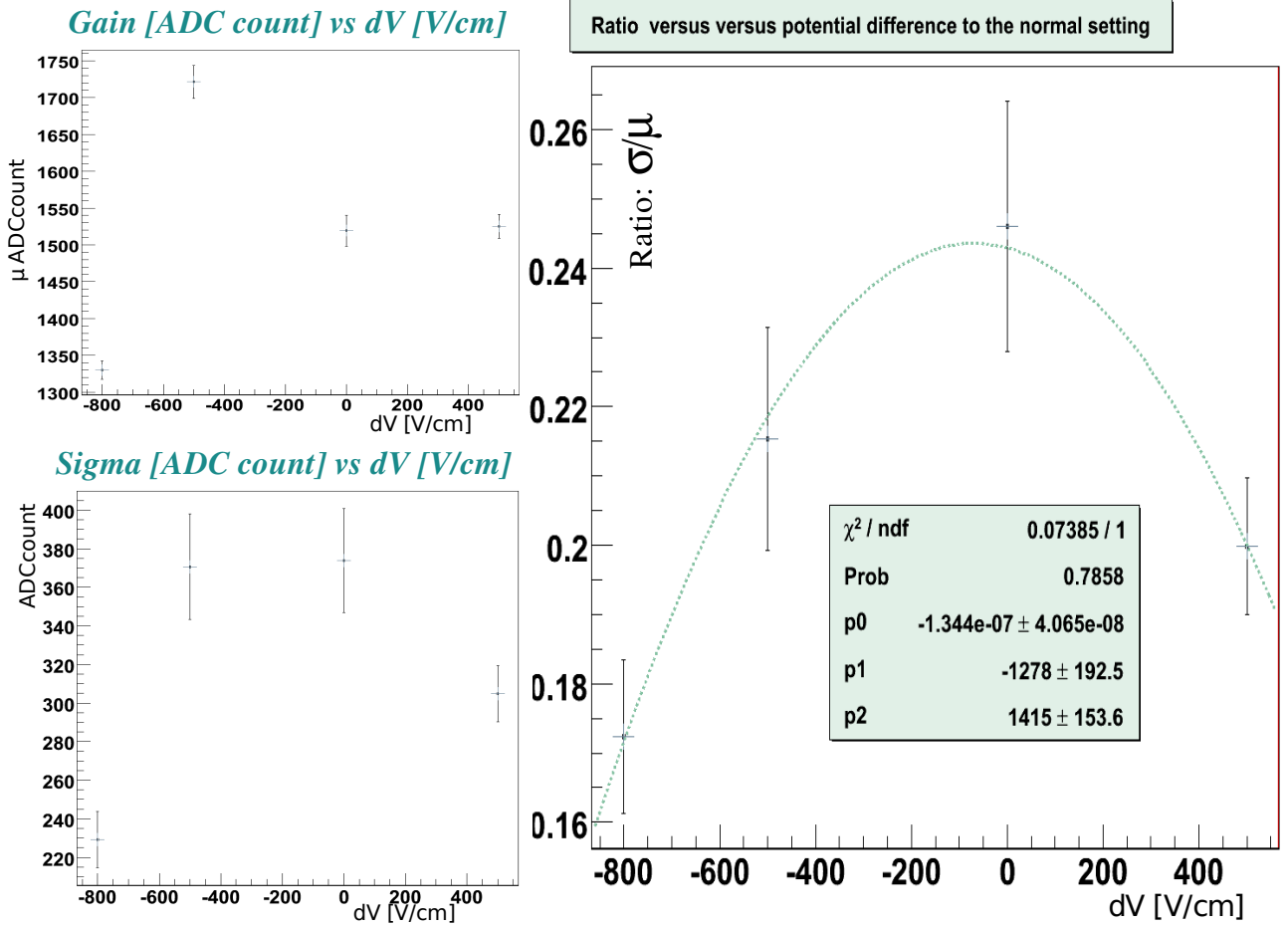


Figure 60: Mean and sigma value of the iron source peak (left) and resolution as a function of  $dV$  (right).

since a parabolic correlation is clearly observed for the resolution showing an expected symmetry with the similar value found for  $dV = -500$  and  $+500$  V. This result is not so evident for the sigma nor for the mean value. A same measurement over various pads, with more amplification variation, and more statistics might give better information about the best setting for a setup of three GEMs and maybe a confirmation of the parabolic behaviour.

### 6.4.3 Drift field variation

Measurements changing the drift field from 140 V/cm to 200 V/cm show (see figure 61) a linear correlation. The linearity is by now not explained and needs further measurements. The increase observed can imply a huge attachment in  $\text{ArCO}_2$ . Actually, when the drift field is stronger, the electrons go faster to the first GEM and have less time to be attached. This observed effect is then in accordance with the argument of section 6.2.2 concerning the shape of the iron spectrum. Therefore,

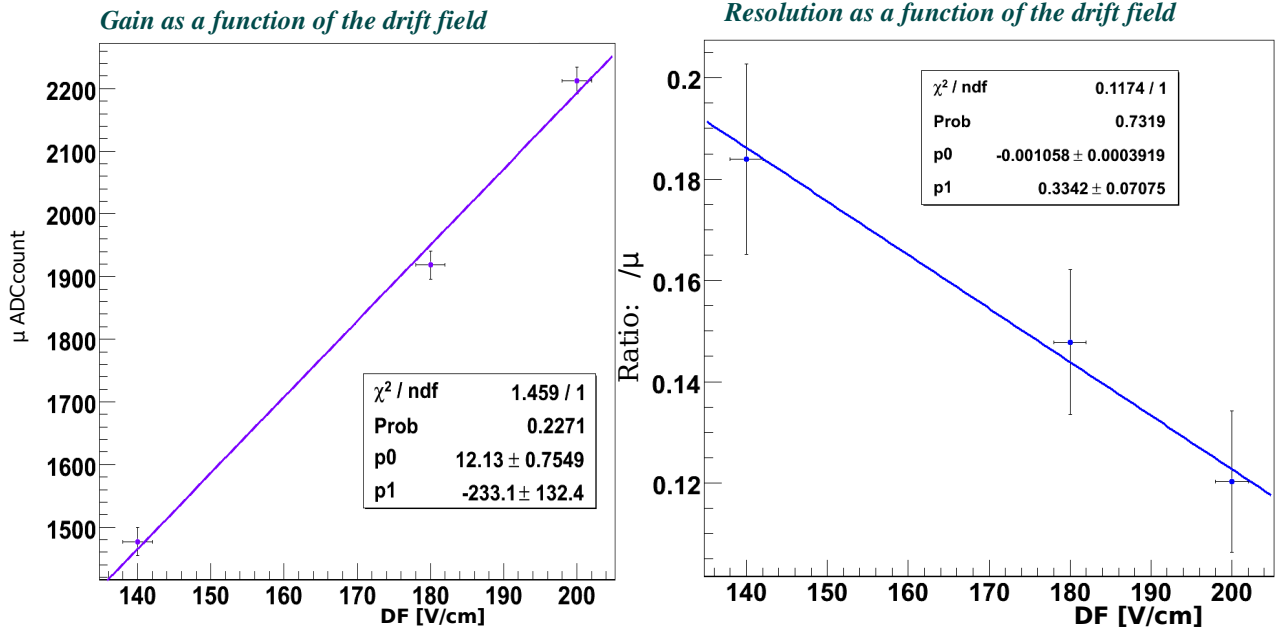


Figure 61: Mean value of the iron source peak (left) and ratio value as a function of the drift field  $DF$  (right). The resolution uncertainties are dominated by the sigma uncertainties.

measurement with other gas mixture

## 6.5 Modification of the guard ring potential

As we saw before in the simulations, a change in the guard ring potential can affect the distortions at the edge of the guard ring.

The nominal setting taken into account is described in Table 10.

$IF$ [V/cm]	$TF1$ [V/cm]	$TF2$ [V/cm]	$V_q$ [V]	$DF$ [V/cm]	$V_{GR}$
-2005	2010	-2020	-315	180	-3557

Table 10: Nominal setting.  $V_q$  is the potential difference between the top and the bottom of the GEMs,  $DF$  the drift field while  $V_{GR}$  is the guard ring potential.

In figure 62, three different example of charge map are given. For  $DV = -70$  V, no charge is detected in the row 24 which is the first row of the second sector. It follows that a part of the charges are collected by the insulator of the guard ring. For  $DV = 70$  V the cluster is shifted to the left size even if more charges are collected in the second sector.

Figure 63 shows that the collected charge depends highly on the guard ring potential. The highest charge detected is for a guard ring potential of -3500 V and not for the nominal setting. For a motor position located in the row 23 and pad 16, distortion appear to be greater when  $DV$  is increased since the pads (21,17) and (22,17) are affected in this case. This observation do not correspond to the simulations done in the previous chapter. Actually, GARFIELD do not take into account that the PVC

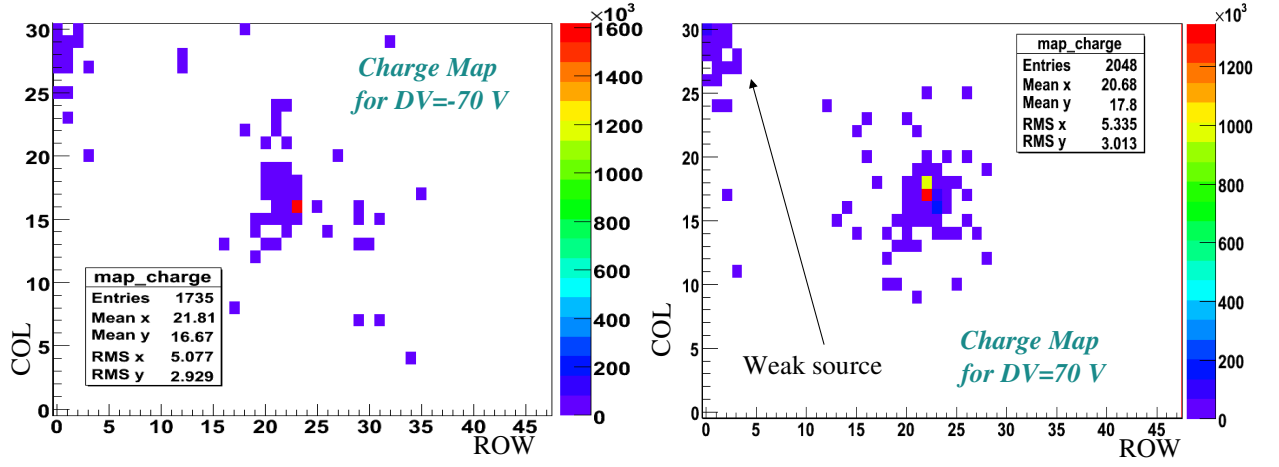


Figure 62: Charge map for three GR voltage settings. The cluster of charges situated on the left side are due to the weak source.

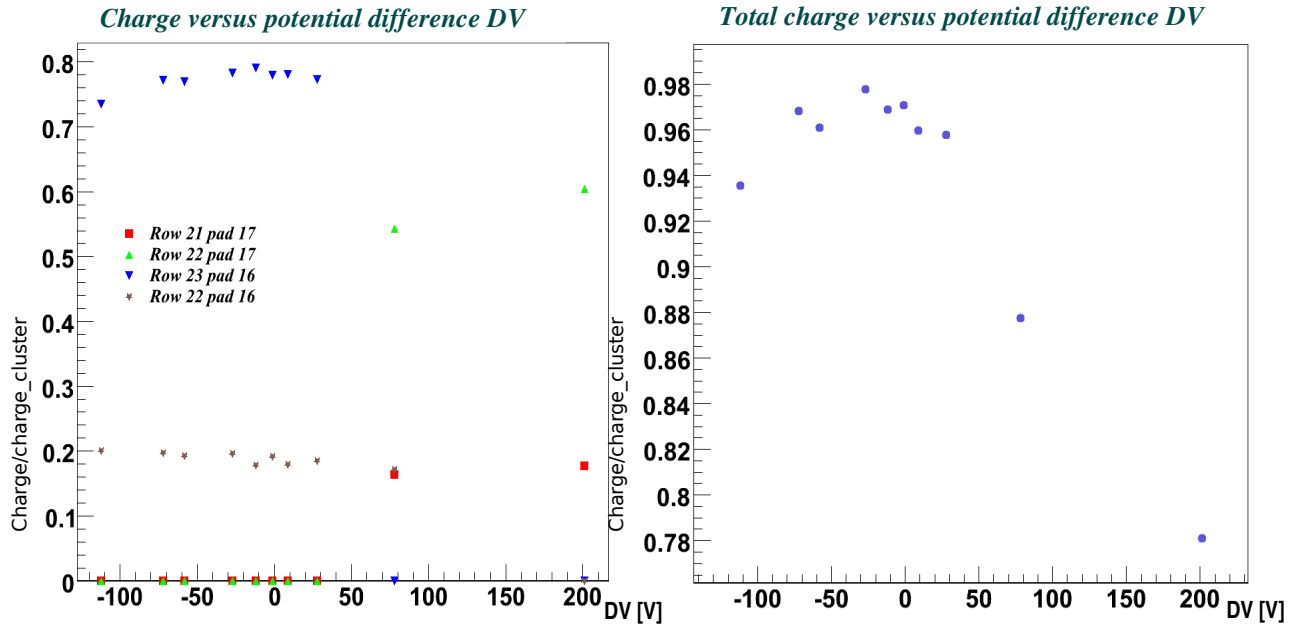


Figure 63: Charge collected of the main hit pads normalized with the total charge inside the cluster (e.g. ROW > 10), for a constant number of trigger (left) as a function of  $DV$ , the potential difference to the nominal setting which is described in Table 10 ( $DV = V_{NS} - V_i$ , with  $i$  the setting number). Total normalized charge collected on the main hit pads (right) as a function of  $DV$ .

insulator below the guard ring copper layer charges itself and becomes electronegative. In consequence, the electrons are not reaching the insulator anymore because of the electrostatic repulsion, as it is shown in figure 46.

### 6.6 Pad response function: source displacement over three pads

The change of the motor position with a step smaller than the width of a pad gives an information about the effective resolution. The step is chosen to be 1 mm so that 17 different positions are taken, from the center of pad 17 to the center of pad 19.

Monte Carlo simulations of the arrival electron distribution have been done depending on where the spot is placed with respect to the grid pattern. The distributions shown in figure 65 are very different. When the collimator moves by steps smaller than a pad width, like 1 mm, the spot distribution goes through these three distributions. Therefore, to be closer to the reality, a pad response function using a different distribution with respect to source position might be done.

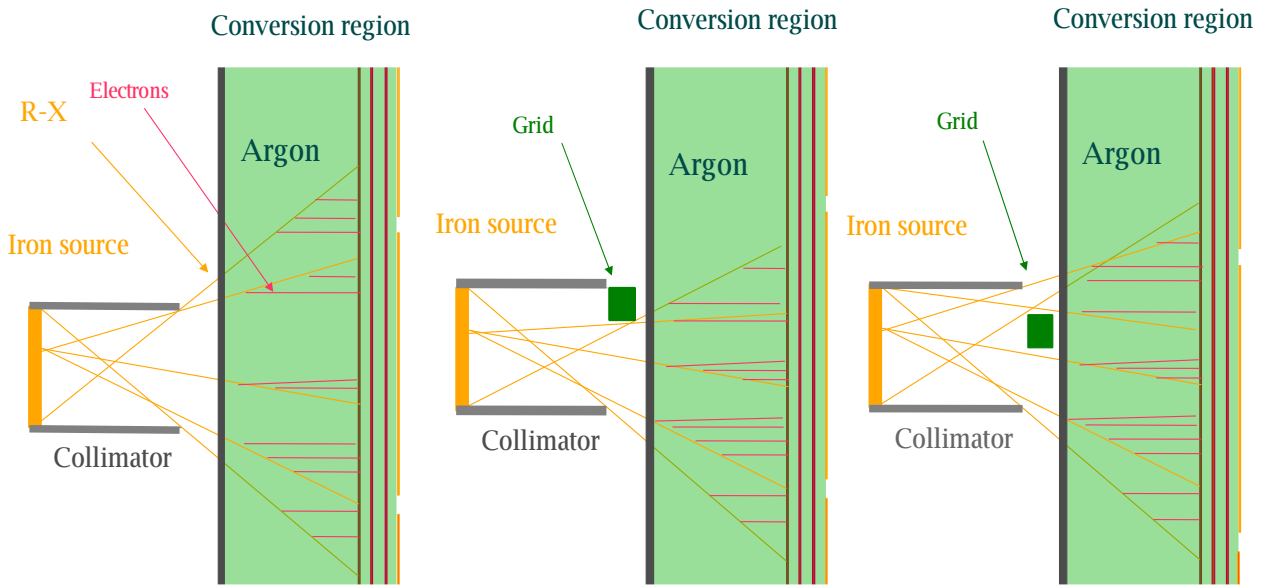


Figure 64: Schematic position of the collimator without grid (left), with the grid at the edge of the spot (middle), inside the spot (right).

However, as a first approximation, I assume that the charge distribution follows the first distribution to fit the data, which is clearly false in presence of the grid. Therefore the parameters of the fit of figure 66 are only at the same order of magnitude and do not correspond to the parameters of the distribution of the spot without grid. Figure 66 shows the fit of the data with this theoretical approach. The  $p_0$  parameter corresponds to the height of the constant plateau of the first distribution,  $p_1$  corresponds to the middle position of the distribution,  $p_2$  the radius plateau,  $p_3$  corresponds to the amplitude of the gaussian distribution outside of the plateau,  $p_4$  its sigma, and  $p_5$  the total normalisation. The mean of the gaussian distribution is fixed as  $p_1$ .

As a first influence of the grid effect, figure 66 shows that the mean value (e.g  $p_1$ ) of the distribution is always shifted with a value of -0.6 mm. Actually, the  $p_1$  value of each distribution might be at 0, 8 and 16 mm, and not -0.6, 7.4 and 15.4 mm as it is observed. The value of 0.6 mm does not correspond to the grid width which is 1.2 mm. The sign of the shift is due to the row analyzed which was chosen

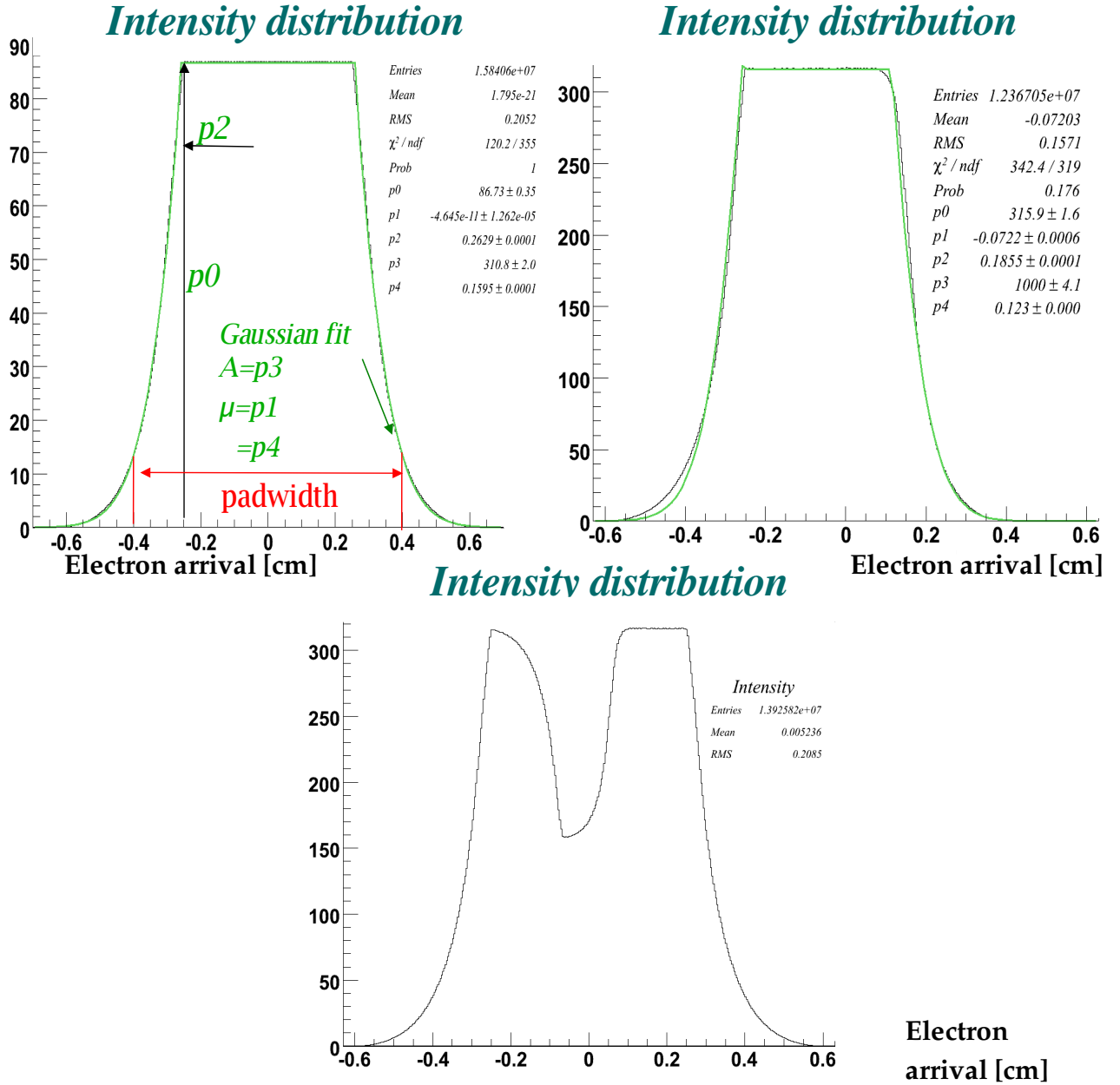


Figure 65: Arrival electron distribution without grid (top-left), with the grid at the edge of the spot (top-right), inside the spot (bottom). The top distribution are fitted with the same function which is used to determine the response function. For both grid distributions, the grid thickness of 6 mm was not taken into account and only the grid width was considered. In consequence the effect of the grid might be even more larger in the reality.



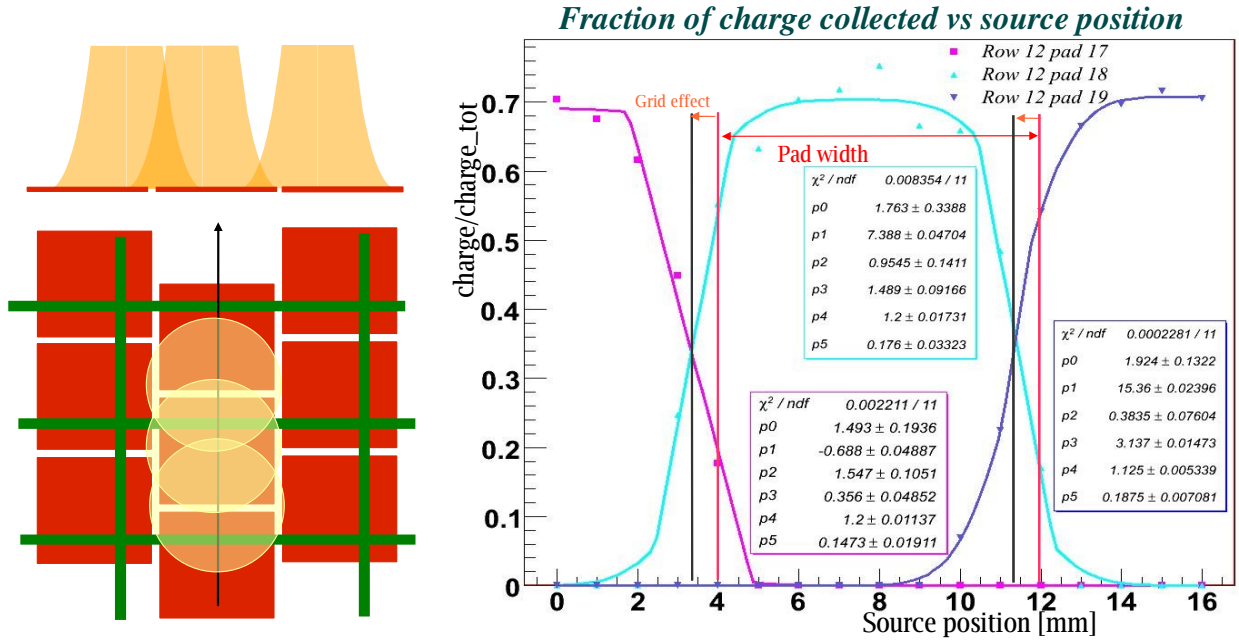


Figure 66: Schematic principle of the charge response function of a pad as a function of the collimator position (left). Collected charge as a function of the collimator position (right).

to be the row on the left side of the grid window (see figure 66).

The grid effect will be much smaller for Micromegas since there is no staggered pad, and the collimation smaller (see figure 27).

## 7 Conclusion

This master thesis reports the combined efforts of the groups of Geneva, Barcelona and Saclay in the study of GEM and Micromegas readout technologies. The Micromegas readout technology was chosen in 2006 to be implemented in the future ND280 TPC which is an important element of the near detector of the T2K experiment. The main goals of this common study were:

- Characterization of the GEM readout used in the HARP TPC.
- Design of a calibration box for the Micromegas readout.

For the first point, the GEM foils have been retrieved from the LHCb experiment, tested and integrated in a tower structure based on individual frames. A testing procedure of the GEM foils has been developed.

Data have been successfully taken and analysed. The results of this study are still preliminary but one was already able to quantify the electric distortions at the edges of the tower using inputs from GARFIELD simulations. Further measurements are required to clearly determine the behaviour of the gain and resolution as a function of the applied drift, transfer and induction fields.

GEM measurements are currently performed with Ar:iC<sub>4</sub>H<sub>10</sub> (98:2) in order to compare energy resolution and gain previously obtained with Ar:CO<sub>2</sub> gas mixture. The procedure analysis developed during the GEM test bench will be also applied to the Micromegas test bench.

The choice of Micromegas technology for the ND280 TPC readout imposed new constraints on the design of the calibration box to minimize electric field distortions. Precision requirements on the voltage settings and alignment were obtained from the simulations discussed in this thesis.

The first operational Micromegas module (MM1) will be tested inside the calibration box in the next few months.

## References

- [1] Fechner M. *Détermination des performances attendues sur la recherche de l'oscillation  $\nu_\mu \rightarrow \nu_e$  dans l'expérience T2K depuis l'étude des données recueillies dans l'expérience K2K*. PhD thesis, Université Pierre et Marie Curie - Paris VI, 2006.
- [2] Gonzalez-Garcia M.C. *Neutrino Masses and Mixing: Evidence and Implications*. Theory Division, CERN, January 8, 2003.
- [3] Maggiore M. *A Modern Introduction To Quantum Field Theory*. Oxford University Press, 2005.
- [4] Univeritat Autònoma de Barcelona. *A Time Projection Chamber For The Near Detector Of The T2K Experiment*, 2006. [http://lhcb.physik.unizh.ch/time05/Talks/Talk\\_Thursday\\_Federico\\_Sanchez.pdf](http://lhcb.physik.unizh.ch/time05/Talks/Talk_Thursday_Federico_Sanchez.pdf).
- [5] T2K collaboration. *Tokai-to-Kamiokande (T2K) Long Baseline Neutrino Oscillation Experiment Proposal*, April 28, 2006.
- [6] Physics Letters B. *Review of particle physics*. ELSEVIER, volume 592, 15 July 2004.
- [7] Ronan T. *Early TPC History and Recent Developments*. LBNL (Berkeley), December 20, 2004.
- [8] Hoch M. *Trends and new developments in gaseous detector*. ELSEVIER, August 27, 2004. [vci.oew.ac.at/2004/book\\_1.5.pdf](http://vci.oew.ac.at/2004/book_1.5.pdf).
- [9] *Charge dispersion MPGD Readout @ ILC-TPC Prototype Test Beam Studies*. Carleton University & TRIUMF, April 7, 2006. [http://www.physics.carleton.ca/research/ilc/talks/Dixit\\_Berkeley\\_TPC\\_Workshop\\_2006.pdf](http://www.physics.carleton.ca/research/ilc/talks/Dixit_Berkeley_TPC_Workshop_2006.pdf).
- [10] Abgrall N. *Work for the 280 m off-axis Detector*. University of Geneva, October 19, 2006.
- [11] *Electric Field Distortion Study in a GEM Module Draft v1r1*. University of Geneva, 2006.
- [12] Thomas Schwetz. *Global fits to neutrino oscillation data*. Institute of Physics Publishing, Phys. Scr. T127(2006)1-5, June 7, 2006.
- [13] Tavernet J.-P. Schune P. Cours sur les détecteurs en physique des particules et en astro-particules, 2005. <http://www-dapnia.cea.fr/Phocea/Membres/Cours/index.php>.
- [14] Thorsten Lux. *Bau und Test einer Mini-TPC mit GEM-Auslese zur Messung des Ionen-Rückflusses*. PhD thesis, University of Hamburg, Oktober 9, 2001.
- [15] T. Kobayashi. J-PARC Neutrino Beam Line. In Y. Suzuki, M. Nakahata, S. Moriyama, and Y. Koshio, editors, *Neutrino Oscillations and their Origin*, pages 152–+, January 2005. <http://adsabs.harvard.edu/abs/2005noo..conf..152K>.
- [16] *Status of J-PARC Neutrino Project T2K*. IPNS, April 8, 2005. <http://nnn05.in2p3.fr/trans/kobayashi.pdf>.
- [17] S. Roth. Recent developments in gaseous tracking detectors. *Nuclear Physics B Proceedings Supplements*, 117:899–902, April 2003. <http://adsabs.harvard.edu/abs/2003NuPhS.117..899R>.
- [18] Kopp J. *Phenomenology of Three-Flavour Neutrino Oscillation*. PhD thesis, Technische Universität München, May 2006. <http://www.mpi-hd.mpg.de/personalhomes/jkopp/pdf/diplomathesis.pdf>.

- [19] Honda Minako. *Matter effect on neutrino oscillation from neutral current universalitiz violation.* University of Ochanomizu, December 14, 2005. <http://ccweb1.kek.jp/group/riron/workshop/KEKPH2006/file/Honda.pdf>.
- [20] Barouch G. *Analyse des phénomènes physiques liés au fonctionnement du détecteur gazeux à micropistes micromegas.* PhD thesis, Université de Paris-Sud, April 27, 2001.
- [21] Abgrall N. *Construction and Performance of a Triple GEM as Amplification Device for the ND280m TPC Detector at the T2K experiment.* University of Geneva, February 2006.
- [22] Rob Veenhof. *Garfield - simulation of gaseous detector - Users Guide v.8.01.* CERN writeups Ref. W505, 2005.
- [23] CERN. Maxwell and hfss at cern. <http://wwwce.web.cern.ch/wwwce/ae/Maxwell/documentation.html>.
- [24] Thorsten Lux. *A GEM Module with two large 3-GEM Towers.* Universitat Autònoma de Barcelona, 2006.
- [25] Kudenko Y. *Status of the T2K experiment.* Institute for Nuclear Research, Moscow, July 28, 2006. [www.nd280.org/presentations/kudenko.pdf](http://www.nd280.org/presentations/kudenko.pdf).
- [26] *A Micromegas based TPC for the T2K ND280 detector: advantages and benefit for T2K.* Dapnia-Sacley, April 26, 2006.
- [27] *ND280.* University of Geneva, March 7, 2007. [http://dpnc.unige.ch/users/dimarcompresentationsmcgillt2k\\_nd280](http://dpnc.unige.ch/users/dimarcompresentationsmcgillt2k_nd280).
- [28] *Test Bench for GEMMM Module Calibration.* University of Geneva, March 7, 2007. <http://dpnc.unige.ch/users/dimarcomtbenchtest.bench.pdf>.
- [29] *T2K 280m detector.* University of Victoria, Canada, 2005. <http://fphy.hep.okayama-u.ac.jp/NuInt/main/session3/karlen-nuint05.pdf>.
- [30] *The JPARC Neutrino Target.* ICRR, University of Tokyo, 2003. [http://www.cap.bnl.gov/mumu/conf/target-030908/tuesday\\_am/Hayato.pdf](http://www.cap.bnl.gov/mumu/conf/target-030908/tuesday_am/Hayato.pdf).
- [31] *JPARC Neutrino beamline and target development.* ICRR, University of Tokyo, 2005. [www.cap.bnl.gov/mumu/conf/target-051010/talks/TNakadaira1.pdf](http://www.cap.bnl.gov/mumu/conf/target-051010/talks/TNakadaira1.pdf).
- [32] *T2K ND280 Time Projection Chambers.* University of Victoria, Canada, January 8, 2007. <http://phys01.comp.uvic.ca:8080/karlen/talks/t2k/tpcreview2007.pdf>.
- [33] Martin J. Colas P., Giomataris I. *Micromegas tpc r&d.* Technical report, LAL 03-10, DAPNIA-02-409, 2003. <http://hal.in2p3.fr/in2p3-00022317>.
- [34] *R&D pour la TPC à lecture Micromegas des futurs collision-neurs linéaires  $e^+ - e^-$ .* DAPNIA, November 5, 2001. [www-dapnia.cea.fr/Phoceaf/file.php?class=std&&file=Doc/Publications/Archives/dapnia-02-347.pdf](http://www-dapnia.cea.fr/Phoceaf/file.php?class=std&&file=Doc/Publications/Archives/dapnia-02-347.pdf).
- [35] Yoshikazu Y. *The T2K program.* HEARO, March 16, 2006. [linkinghub.elsevier.com/retrieve/pii/S0920563206000909](http://linkinghub.elsevier.com/retrieve/pii/S0920563206000909).